

Copyright
by
Liangfeng Sun
2006

The Dissertation Committee for Liangfeng Sun
certifies that this is the approved version of the following dissertation:

Two-beam SHG from centrosymmetric media

Committee:

Michael C. Downer, Supervisor

Todd Ditmire

Greg O. Sitz

Zhen Yao

John G. Ekerdt

Two-beam SHG from centrosymmetric media

by

Liangfeng Sun, B.E., M.S.

DISSERTATION

Presented to the Faculty of the Graduate School of
The University of Texas at Austin
in Partial Fulfillment
of the Requirements
for the Degree of

DOCTOR OF PHILOSOPHY

THE UNIVERSITY OF TEXAS AT AUSTIN

December 2006

Dedicated to my wife Wenqi.

Acknowledgments

I thank my supervisor, Prof. Michael C. Downer, for his enormous guidance and support throughout my Ph.D. graduate research. This work would have been impossible without his insightful directions and constant encouragement.

I appreciate my Ph.D. supervising committee members, Prof. John G. Ekerdt for his guidance and help, Prof. Todd Ditmire, Prof. Greg O. Sitz and Prof. Zhen Yao for their time and support.

I owe special thanks to my colleagues in labs, Dr. Yingying Jiang, Dr. Daeyoung Lim, Dr. W. Thomas Leach and Dr. Jianhong Zhu. Yingying helped me get familiar with the experiment apparatus when I started exploring the world of ultrafast optics. Daeyoung advised me a lot on maintaining the laser system in Prof. John G. Ekerdt's lab. I learned a lot of vacuum technology and surface chemistry from Jianhong and Thomas in Chemical Engineering Department. I enjoyed the time working with Dr. Scott Stanley on the project of monitoring nanocrystal growth with laser. I thank Dr. Ramon Carrilles-Jaimes, Dr. Bonggu Shim, Dr. Nicholas Hill Matlis, Dr. Yongqiang An, Dr. Jinhee Kwon, Dr. Kui Wu, Dr. Carsten Winterfeldt, for their helpful discussions.

I offer my humblest thanks to my colleagues in Mexico, Prof. W. Luis

Mochán and Prof. Bernardo S. Mendoza, for their guidance in theoretical modeling. I thank visiting students Jens Rafaelsen from Denmark, Joost Gielis from Netherlands for their help in the experiments and the good time.

I appreciate the time with my fellows in the labs: Peter Figliozzi for working together in surface spectroscopy and sharing ideas with me, Rafal Bogumil Zgadzaaj, Benjamin Bowes and Franklin Grigsby for inspiring discussions on laser and optics, P. J. Smith, Sebastian Jung and Adrian Wirth for their help in Femtosecond Spectroscopy Lab, Shawn Coffee and Wyatt Winkenwerder for their help in C4GAS Lab.

I thank James Halligan for assisting me with purchasing matters, Robert Hasdorff and John England for helping me on electronics, Jack Clifford for his help in the machine shop, Carol Noriega, Linda Hallidy, Cathy Rapinett and Mary A Whitmore for helping me out on the paperwork related to graduate study and conference travels.

I thank my parents – Junyi Sun and Jinzhi Bao, and parents-in-law – Daqian Zhao and Jinxiu Gong for their trust, guidance and wisdom.

Above all, I thank my wife Wenqi for her support and patient understanding.

Two-beam SHG from centrosymmetric media

Publication No. _____

Liangfeng Sun, Ph.D.

The University of Texas at Austin, 2006

Supervisor: Michael C. Downer

We report a comprehensive study of quadrupolar second-harmonic generation (SHG) from centrosymmetric materials. Because of symmetry, quadrupolar SHG from centrosymmetric materials is forbidden in the forward direction, and is extremely weak when it is obtained using a traditional single-beam SHG geometry. A two-beam geometry is found to enhance quadrupolar SHG greatly compared to single-beam SHG. Two orthogonally polarized laser beams create wavelength-scale, forward-radiating gradients in the second-harmonic polarization that enhance SHG. The radiation pattern of two-beam quadrupolar SHG is observed to have a TEM_{00} mode, different from single-beam quadrupolar SHG which has a TEM_{01} mode. The quantitative study of quadrupolar SHG is done with a two-beam geometry on an isotropic glass slide. The polarization of the two-beam quadrupolar SHG is found to be normal to the plane determined by the two crossed fundamental beams, and the SHG intensity depends on the orthogonally polarized fundamental electric fields. Quadrupolar SHG from a glass slide with two tightly focused laser beams appears surface-like

– SHG peaks sharply when the glass surfaces are centered on the two-beam overlap region, but vanishes when the overlap is totally immersed in glass bulk. Quasi-phase-matched quadrupolar SHG from two glass slides (and two pellicle films) is demonstrated. Enhanced and phase-matched two-beam SHG from a centrosymmetric and birefringent crystal – calcite – is also realized. Preliminary studies on the application of two-beam SHG in microscopy are done with a scratched glass slide. We find that dipolar SHG and quadrupolar SHG can be selectively imaged by choosing different polarization combinations of the fundamental laser beams. Macroscopically centrosymmetric silicon nanocrystal composites embedded in glass are studied by single-beam and enhanced two-beam SHG. Both techniques are sensitive to the nano-interface chemistry, but two-beam SHG gives rise to a signal that is several orders stronger. Multiple signal discrimination techniques are developed to separate the nanocrystal SHG from the glass SHG which is also enhanced by the two-beam geometry. The enhanced two-beam SHG enables spectroscopy and time resolved studies of silicon nano-interfaces.

Table of Contents

Acknowledgments	v
Abstract	vii
List of Tables	xi
List of Figures	xii
Chapter 1. Introduction	1
1.1 Historical notes	2
1.2 Phenomenological model of quadrupolar SHG	4
1.3 Scope of this work	6
Chapter 2. Quadrupolar SHG in glass	8
2.1 Introduction	8
2.2 Theory	9
2.3 Experimental setup	10
2.4 Enhanced 2-beam SHG from glass	12
2.5 SHG from glass using elliptically polarized beams	16
2.6 SHG from glass by z-scan	17
2.7 “Sandwich” experiment	21
2.8 Two-beam SHG microscopy	28
2.9 Conclusion	34
Chapter 3. Quadrupolar SHG in silicon nanocrystals	35
3.1 Introduction	35
3.2 Sample preparation	36
3.3 Single beam SHG from Si nanocrystals	39
3.3.1 Sensitivity to surface chemistry	39

3.3.2	Sensitivity to nanocrystal density gradients	41
3.3.3	SHG Radiation pattern	42
3.4	Two-beam SHG	43
3.4.1	Two-beam SHG Theory	45
3.4.2	Enhanced SHG from Si NC sample	47
3.4.3	SHG signal discrimination	52
3.5	Conclusion	58
Chapter 4.	Phase matched quadrupolar SHG from centrosymmetric materials	60
4.1	Introduction	60
4.2	Quasi-Phase-Matched SHG from glass slides	63
4.3	Quasi-Phase-Matched SHG from pellicle thin films	69
4.4	Phase-Matched SHG from calcite crystals	70
4.5	Discussion	73
Chapter 5.	SHG <i>in situ</i> monitoring of CVD growth of nanocrystals	75
5.1	Introduction	75
5.2	Experimental Setup	77
5.3	Surface contaminants effect on TDSHG	83
5.4	Monitoring growth of Si NCs	85
5.5	Summary	94
	Appendix	95
	Appendix 1. SH polarization direction	96
	Bibliography	98
	Index	106
	Vita	108

List of Tables

4.1	Comparison of type I and type II phase-matched SHG efficiencies in single-beam and two-beam geometries when short or long pulses are used.	74
-----	--	----

List of Figures

1.1	Principle of SHG	2
2.1	Two-beam SHG configuration. Beam 1 is normally incident onto the glass sample and polarized horizontally (in \hat{x} direction). The incident angle of Beam 2 is 20° . Its polarization can be tuned through a $\lambda/2$ plate.	11
2.2	Two-beam SHG experimental setup.	12
2.3	Two-beam SHG with unamplified laser as \mathbf{E}_2 rotates from vertical (\hat{y}) to horizontal (P -polarized), with \mathbf{E}_1 fixed along \hat{x} . The SH radiation was completely \hat{y} -polarized. Dashed line: dark count level.	13
2.4	Two-beam SHG signal for $\mathbf{E}_1 \parallel \hat{x}$, $\mathbf{E}_2 \parallel \hat{y}$ observed through polarization analyzer, showing signal polarized along \mathbf{E}_2	15
2.5	Experimental setup. The normally incident beam passes through a $\lambda/4$ waveplate before reaching the sample. The oblique incident beam is linearly polarized. Its polarization can be set in the horizontal (\hat{x}) or in the vertical (\hat{y}) by a $\lambda/2$ waveplate. . .	16
2.6	Two beam SHG signal vs. ellipticity of beam 1 polarization. Squares (circles) correspond to $\mathbf{E}_2 \parallel \hat{y}$ (\mathbf{E}_2 P -polarized). Curves are calculations based on Equation 2.2.	18
2.7	Measured (solid squares) and calculated (solid line) SHG intensity as the sample is scanned longitudinally (in \hat{z} direction) along the 2-beam overlap region of tightly focused unamplified beams. Dashed line: dark count level.	19
2.8	The integral of the 2-beam SH polarization vanishes when the 2-beam overlap is totally inside the glass bulk (left figure), but does not vanish when only part of the overlap is in the glass bulk (right figure).	21
2.9	Calculated SHG intensity as the sample is scanned longitudinally (in \hat{z} direction) along the 2-beam overlap region of tightly focused unamplified beams. Cross: Guoy phase included; Diamond: Guoy phase not included.	22

2.10	Measured (solid squares) and calculated (solid line) SHG intensity as the sample is scanned longitudinally (in \hat{z} direction) along the 2-beam overlap region of loosely focused amplified beams.	23
2.11	Left: z-scan of the overlap of two laser beams through two stacked glass slides with an air gap in between; right: 2-beam SHG shows three peaks along the z-direction.	24
2.12	Left: z-scan of the overlap of two laser beams through two stacked glass slides with a water gap in between; right: 2-beam SHG shows two peaks along the z-direction.	25
2.13	Simulated 2-beam SHG peaks when the sandwiched sample (glass/air/glass) is z-scanned through the 2-beam overlap. . .	26
2.14	Simulated 2-beam SHG peaks when the sandwiched sample (glass/water/glass) is z-scanned through the 2-beam overlap. The middle SHG peak depends on the SH susceptibility of water.	27
2.15	Linear (a, b) and SH (c) images of a ZnO cluster. From (a) to (b), the sample was shifted so that the image of the ZnO particle can be distinguished from the background.	30
2.16	Linear (a) and SH (b) images of a ZnO cluster show the size of the cluster is the same ($\sim 4.8\mu\text{m}$) in either case.	31
2.17	2-beam SHG image of a glass slide with a scratch on one surface. (a) Straight beam (beam 1) is horizontally polarized (in \hat{x}), angled beam (beam 2) is vertically polarized (in \hat{y}). (b) Both beams are polarized in $\hat{x} - \hat{z}$ plane. (c) Difference of image in (a) and in (b).	32
2.18	2-beam SHG image of a glass slide with a scratch on one surface. (a) Straight beam (beam 1) is horizontally polarized (in \hat{x}), angled beam (beam 2) is vertically polarized (in \hat{y}). (b) Both beams are polarized in $\hat{x} - \hat{z}$ plane. (c) Difference of the image in (a) and the image in (b).	33
3.1	composite density profile (solid curve) for excess Si $5 \times 10^{21} \text{cm}^{-3}$, $\langle d_{NC} \rangle = 3$ nm of depth $L_{\text{implant}} \sim 1 \mu\text{m}$ formed by Si ion implantation at six different energies (dotted curves).	37
3.2	(a) A typical silicon nanocrystal sample. The yellow region is where Si nanocrystals are embedded, while the transparent margin is pure glass. (b) Cross-section TEM micrograph of a typical single silicon nanocrystal embedded in a glass substrate [49, 51]. The NCs with average diameter $\langle d \rangle_{NC} = 3, 5$ and 8 nm, respectively (with 30% size fluctuation), with corresponding NC densities $n_{NC} = 7, 3$ and $1.5 \times 10^{18} \text{cm}^{-3}$ were formed under different conditions.	38

3.3	Scan of single-beam SHG across the boundary between Si NC implant and unimplanted glass rim at edge of sample. $x < 0 \mu\text{m}$ – NCs implanted region; $x > 0 \mu\text{m}$ – pure fused silica margin. Solid dots (circles) correspond the sample annealed in Ar (Ar + 4% H ₂). Inset: single beam transmitted SHG configuration.	40
3.4	Small step lateral scan on the boundary between pure glass and nanocrystal-embedded glass shows SHG sharply increasing at some points.	42
3.5	The SHG radiation pattern measured by a CCD camera has a TEM ₀₁ mode (double lobes, lower right) when the incident fundamental beam has TEM ₀₀ mode (upper right). The experimental setup for imaging the SHG mode is shown in the main panel of the figure.	43
3.6	The gradient of the fundamental electric field vanishes in the center of a Gaussian beam, so does the SH field.	44
3.7	Two laser beams are used to excite quadrupolar SHG from centrosymmetric materials.	46
3.8	The 2-beam SHG intensity depends on the angle between the polarization of E_1 and E_2 . The intensity maximized when $E_1 \perp E_2$	48
3.9	(a) Scan of two-beam SHG across the boundary between Si NC implant and unimplanted glass rim at edge of sample. $x > 0 \mu\text{m}$ – NCs implanted region; $0 > x > -1000 \mu\text{m}$ – pure fused silica margin; $x < -1000 \mu\text{m}$ – air. Solid dots (circles) correspond the sample annealed in Ar (Ar + 4% H ₂). (b) Transmission two-beam SHG geometry.	49
3.10	The spatial profile of the 2-beam SHG from Si NC embedded region appears in a TEM ₀₀ mode.	50
3.11	Transmitted 2-beam SHG (labeled as SFG in the figure) scan across the boundary (2.2mm) between 5 nm Si NCs and unimplanted glass on the samples annealed for 1 hour at 1100 ^o C in pure Ar. Both of the incident beams are P polarized according to the sample.	51
3.12	a) The incident beam electric field has no component along the gradient at the the Si NCs composite/glass interface. b) The incident beam electric field component along the gradient at the the Si NCs composite/glass interface increases when the sample is tilted.	52
3.13	Scan of two-beam SHG across the glass-NC boundary with a NC layer ($\langle d_{NC} \rangle = 5\text{nm}$) at entrance (filled squares) or exit (triangles) side of sample, with orthogonally polarized incident fields.	53

3.14	Frequency dispersed SHGs from pure glass (solid circles) and nanocrystal embedded glass (solid squares) show “Maker” fringes due to the frequency dependent phase mismatch. The solid lines are fitting curves.	55
3.15	Frequency dispersed SHGs from pure glass (solid circles) and nanocrystal embedded glass (solid squares) when the two beams are co-polarized don’t show “Maker” fringes.	57
3.16	Two-beam SHG z -scan: a NC sample stacked with a same size fused silica slide with water filled in the gap. Top: z -scan in the pure fused silica margin; Bottom: z -scan in the NC implanted region.	58
4.1	The diagram in the center shows the growth of SH electric field in a complex coordinate. (a) If there is phase mismatch between the SH polarization wave and the SH radiation wave, the SHG oscillates along the beam propagation direction inside the crystal. (b) The SH field grows linearly along the beam propagation direction when the phase match between the SH e-wave and the fundamental o-wave is realized. (c) Quasi-Phase-Match can be realized when the SH polarization can be periodically reversed in the beam propagation direction. (d) In a polycrystalline structure, superimposition of the SH generated from each domain which has different phase in the beam propagation direction can yield net increase of the total SH [4].	61
4.2	(a) A structure designed to realize Quasi-Phase-Matched 2-beam SHG using isotropic material (e.g. glass). Left: the grey region is the active material, the white region is nonactive material which delays the phase of SH polarization wave relative to SH radiation wave. Right: growth of SH electric field when the fundamental two beams propagate through the material. (b) Phase mismatch between the SH polarization wave and SH radiation wave.	62
4.3	Comparison of calculated SHG growth in different schemes. . .	63
4.4	Simulation of the z -scan of the two-beam overlap across the two stacked glass slides separated by an air gap of different sizes. The horizontal axes represent the longitudinal position (\hat{z}) in μm , and the vertical axes represent the SHG intensity.	65
4.5	z -scan of the two-beam overlap across two stacked glass slides with a gap in between. (a) Gap size is about one coherence length ($13 \mu\text{m}$). (b) Gap size is larger than the two-beam overlap length.	66

4.6	As the two-beam overlap scans laterally across the wedge sample, the SHG signal oscillates as the spacing between the two inner surfaces of the glass slides increases.	68
4.7	Two pellicle films (about 5 μm thick) are set parallel to each other and inside the two beams overlap region. The variation of the distance between the two films can change the phase difference between the two SH field generated from each film. .	69
4.8	Experimental data (solid square) show the coherent superimposition of the two SH field generated from two pellicle films. The horizontal line shows the SHG intensity from a single pellicle film.	71
4.9	Scheme for phase-matched two-beam SHG from calcite crystal.	72
5.1	This cartoon shows all SHG sources from a Si sample: Si/SiO ₂ interface SHG, Si bulk SHG and EFISH due to the DC electric field formed by charges trapped on the SiO ₂ surface.	78
5.2	The intensity of the SHG from Si sample depends on the azimuthal angle. The bulk SHG has 8 fold symmetry. The bulk SHG intensity is 2 order lower than the surface SHG.	79
5.3	The total reflected SHG from a Si sample (lightly p-doped silicon substrate with 9 nm thick SiO ₂ on top) increases by time which is due to the DC electric field building up by the trapped charges on the sample surface.	80
5.4	Experimental setup. M: Mirror, F: Filter, $\lambda/2$: halfwave plate, P: Polarizer, L: Lens.	82
5.5	Top: TDSHG from a lightly p-doped silicon sample with 10 nm thermal oxide on top increases slightly by time. Bottom: After annealing at temperature 600 ⁰ C and then cool down to room temperature, SHG from the same sample is flat over time. The data were taken in high vacuum ($\sim 10^{-9}$ Torr) at room temperature.	84
5.6	TDSHG from n ⁺ doped silicon sample with 2 nm native oxide on top. The sample was annealed at different temperature and then cooled down to room temperature for SHG data taking. The pressure in the vacuum is $\sim 5 \times 10^{-10}$ Torr. Each set data were taken at different point on the sample to avoid SHG hysteresis.	86

5.7	<p>Top: TDSHG from $\text{HfO}_2(3.5 \text{ nm})/\text{SiO}_2(1.1 \text{ nm})/\text{Si}(001)$ sample depends on the annealing temperature (no annealing - solid square, 150°C - solid diamond, 300°C - solid triangle, 600°C - solid circle). Bottom: TDSHG from the same sample is large before annealing the sample (solid squares), but vanishes after annealing at 600°C for 10 minutes (solid circles). After 1 night stay in high vacuum ($\sim 10^{-9}$ Torr.), TDSHG is still negligible weak (solid diamond), but recovers after 1 hour exposure to air (solid triangle). Data were taken at room temperature in high vacuum ($\sim 10^{-9}$ Torr.)</p>	87
5.8	<p>TDSHG from a Si NC sample was observed in a vacuum chamber before annealing the sample (solid squares), but disappeared when the sample was annealed at 600°C for 10 minutes and then cooled down to room temperature (solid circles). After exposure to ambient air for about 12 hours the TDSHG recovered (solid triangles).</p>	89
5.9	<p>TDSHG observed from a Si sample before annealing (solid squares), after annealing (solid circles), after CVD growth for 15 minutes (solid up-triangles), 17.5 minutes (solid down-triangles), 20 minutes (solid diamonds), 25 minutes (solid left-triangles), 30 minutes (solid right-triangles). Data were taken in vacuum ($\sim 10^{-9}$ Torr.) at sample temperature 116°C.</p>	91
5.10	<p>(a) Time-independent SHG from a $\text{SiO}_2(2 \text{ nm})/\text{Si}(\text{n}^+ \text{ doped})$ sample as a function of CVD time. SHG data were taken from five locations on the sample. The maximum (minimum) SHG among the five is shown by solid squares (solid triangles). (b) The ratio of SHG after and before CVD from a $\text{SiO}_2(10 \text{ nm})/\text{Si}(\text{light p-doped})$ as a function of CVD time. Each data point was taken from different samples cut from the same wafer. The error bars indicate SHG variation from point to point on one sample. (c) The sample was cut from the same wafer as in (b). SHG data were taken from four locations (indicated by four different symbols) on the sample after each step of CVD growth. (d) Repeat the experiment as in (c) with another sample cut from the same wafer. SHG from one location of the sample was taken. All SHG were taken in vacuum ($\sim 10^{-9}$ Torr.) at sample temperature $\sim 100^\circ\text{C}$.</p>	93

Chapter 1

Introduction

Second harmonic generation (SHG) is a nonlinear optical process, in which photons interacting with a material are effectively “combined” to form new photons with twice the energy, and therefore twice the frequency and half the wavelength of the initial photons. The interaction between the photons (electromagnetic wave) and the material is illustrated with classical fields in Figure 1.1. The polarization of the material due to the electrons’ response to the driving electromagnetic (EM) field does not totally follow the driving EM field. The distortion of the polarization in time domain generates frequencies (nonlinear) other than the fundamental frequency (linear), which can be easily seen by Fourier decomposition of the polarization (see Figure 1.1). The lowest order of the nonlinear polarization is the second harmonic (frequency doubled) polarization – the source of SH radiation . The SH polarization in centrosymmetric materials (a material possessing a point with respect to which the medium remains unchanged under the operation of spatial inversion: $\mathbf{x} \rightarrow -\mathbf{x}$, e.g. Si bulk, Ge bulk) is dipole forbidden but allowed in noncentrosymmetric materials (e.g., GaAs bulk, surface of any materials). In centrosymmetric materials, the second-order response consists of the electric-quadrupole and magnetic-dipole terms comprised of products of the incident

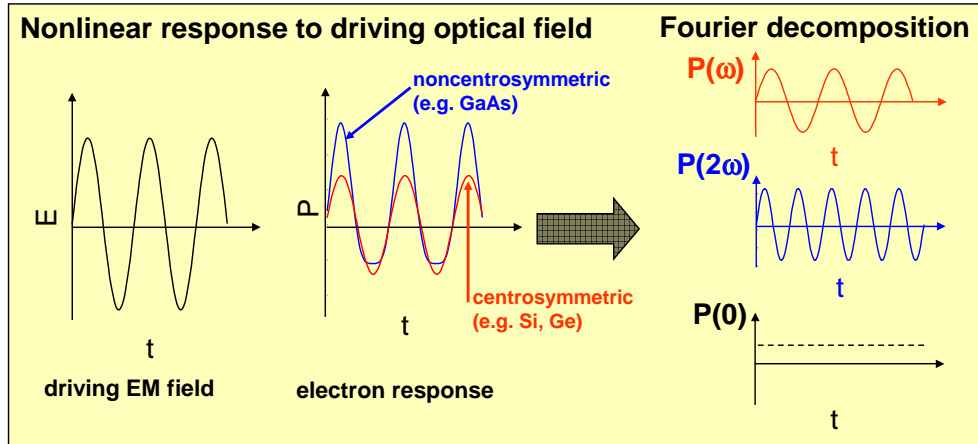


Figure 1.1: Principle of SHG

electric field and its spatial derivatives [9].

1.1 Historical notes

Optical SHG was first observed by Franken *et al.* (1961) in a noncentrosymmetric quartz crystal [24]. One year later, SHG in the centrosymmetric calcite crystal was reported by Terhune *et al.* [45]. Calcite is birefringent so that phase-matching of bulk SHG may be achieved, thus permitting weak quadrupolar SH polarization to produce relatively strong SH signal. In the following years, SHG was observed in a wide range of centrosymmetric materials, including metals [10, 13], semiconductors [8], insulating solids [48] and liquids [47]. In those experiments, the contribution to SHG was dominated by the surface of the materials while the bulk contribution was negligible. The theoretical framework developed by Bloembergen *et al.* was summarized in

his paper in 1968 [9]. It involved a weak polarization in the bulk arising from the magnetic-dipole and quadrupole terms and a thin strongly polarized layer in the surface region. The discontinuities of the pump fields on the surface were thought to be the reason of the strong surface nonlinear response.

The sensitivity of the SHG to surface conditions was first noted by Brown and Matsuoka [12] in 1969. In their experiments, they observed a much stronger SHG from a freshly evaporated Ag film in vacuum than from a film exposed to air. The dependence of SHG on the atomic nature of the surface was seen by Chen and co-workers for Na deposition on clean Ge surfaces [19] in 1973. This demonstrated the potential of SHG for surface studies of centrosymmetric materials. Since then, more theoretical work were done to model the SHG from metal surface. Rudnick and Stern suggested that the broken inversion symmetry of the surface was the source of surface SHG [35]. Sipe and Stegeman then developed a hydrodynamic model to describe the surface response [41]. In experiments, SHG was then widely used to probe surface reactions and adsorption/desorption, even on the atomic and molecular scale.

As a *planar* surface or interface probing technique, SHG has already been well developed. Using this technique to probe the interfaces of nanostructures only took place in the past few years. Since the size of the nanostructures is much less than the wavelength of the incident EM wave, a nanostructure composite is macroscopically centrosymmetric, so SHG vanishes in the dipolar approximation. Nevertheless, this weak quadrupolar type SHG

was detected and studied in a few groups. Aktsipetrov and co-workers (1999) used SHG interferometry to study the mutual coherence between the scattered SH (also called hyper-Rayleigh scattering) and the reference SH [21]. From the interference patterns, they deduced the spatial fluctuations of optical parameters (down to a few hundred nanometers) in bacteriorhodopsin and polycrystalline PZT ferroelectric films. Bonn and co-workers demonstrated the use of vibrational sum frequency generation to investigate the surface molecular properties of submicron particles dispersed in solution [33]. Dadap *et al.* developed the electromagnetic theory of SHG from the surface of a sphere that is small compare to the wavelength of light. Their theory shows that the SH radiation is emitted in nonlocally excited electric dipoles and locally excited electric quadrupole modes. More detailed calculation of SHG from a single sphere was performed by Brudny *et al.* [14], and SHG from arrays of spherical particles by Mochán *et al.* [31]. These models are based no longer on local dipolar SH polarization, but on quadrupolar SH polarization. In the following Section, we briefly review the phenomenological model of quadrupolar SHG.

1.2 Phenomenological model of quadrupolar SHG

The bulk nonlinear polarization source can be expressed in a multipole series of successive degrees of nonlocality:

$$\begin{aligned} \mathbf{P}^{(2)}(2\omega) &= \chi_D^{(2)}(2\omega) : \mathbf{E}(\omega)\mathbf{E}(\omega) \\ &+ \chi_Q^{(2)}(2\omega) : \mathbf{E}(\omega)\nabla\mathbf{E}(\omega) + \dots, \end{aligned} \quad (1.1)$$

where $\chi_D^{(2)}$ is the electric dipolar SH susceptibility, and $\chi_Q^{(2)}$ is the quadrupolar SH susceptibility. In a centrosymmetric material, the electric dipolar SH susceptibility $\chi_D^{(2)}$ vanishes. The leading-order nonlinear polarization can be written as

$$\mathbf{P}_Q^{(2)}(2\omega) = \chi_Q^{(2)}(2\omega) : \mathbf{E}(\omega)\nabla\mathbf{E}(\omega). \quad (1.2)$$

The fourth-rank tensor $\chi_Q^{(2)}$ has 81 independent elements for an arbitrary material. For a centrosymmetric cubic material of $m\bar{3}m$ -symmetry, there are only four nonvanishing elements: $\chi_{Q,iiii}^{(2)}$, $\chi_{Q,iiij}^{(2)}$, $\chi_{Q,ijij}^{(2)}$ and $\chi_{Q,ijji}^{(2)}$, where the tensor is expressed in terms of the crystallographic axes, and indices i, j are distinct. By introducing the phenomenological parameters β , γ , δ and ζ defined by

$$\beta = \chi_{Q,iiij}^{(2)}, \quad (1.3)$$

$$\gamma = \frac{1}{2}\chi_{Q,ijij}^{(2)}, \quad (1.4)$$

$$\delta = \chi_{Q,ijji}^{(2)} - \chi_{Q,iiij}^{(2)} - \chi_{Q,ijij}^{(2)}, \quad (1.5)$$

$$\zeta = \chi_{Q,iiii}^{(2)} - (\chi_{Q,ijji}^{(2)} + \chi_{Q,iiij}^{(2)} + \chi_{Q,ijij}^{(2)}), \quad (1.6)$$

the i -th component of the effective SH polarization can then be written as [9, 40]

$$P_{Q,i}^{(2)} = \gamma\nabla_i(\mathbf{E} \cdot \mathbf{E}) + (\delta - \beta - 2\gamma)(\mathbf{E} \cdot \nabla)E_i + \beta(\nabla \cdot \mathbf{E})E_i + \zeta E_i \nabla_i E_i. \quad (1.7)$$

In a cubic material, ζ can be finite and the last term in Equation 1.7 will give rise to a SH polarization sensitive to the orientation of the crystal. For an isotropic material, we have the relation $\zeta = \chi_{Q,iiii}^{(2)} - (\chi_{Q,ijji}^{(2)} + \chi_{Q,iiij}^{(2)} + \chi_{Q,ijij}^{(2)}) =$

0. So the isotropic materials are described by β , γ , and δ . The third term in Equation 1.7 can always be neglected in a homogeneous medium, since the factor $\nabla \cdot \mathbf{E}$ vanishes according to Maxwell's equations. The first term $\gamma \nabla(\mathbf{E} \cdot \mathbf{E})$ is equivalent to a polarized sheet at the interface with a longitudinal polarization. It always radiates in a manner indistinguishable from that of the interface term [39]. In a homogeneous isotropic medium, the bulk nonlinear polarization can be written as

$$\mathbf{P}_Q^{(2)} = \gamma \nabla(\mathbf{E} \cdot \mathbf{E}) + (\delta - \beta - 2\gamma)(\mathbf{E} \cdot \nabla)\mathbf{E}. \quad (1.8)$$

1.3 Scope of this work

This thesis focuses on characterization, enhancement and application of quadrupolar SHG from centrosymmetric materials using a two-beam SHG geometry – i.e. a degenerate sum-frequency generation. The centrosymmetric materials used in our experiments include fused silica, composites of silicon nanocrystals embedded in fused silica and calcite crystals. In Chapter 2, we present experimental two-beam quadrupolar SHG results from a simple glass slide, which serve to characterize the dependence of quadrupolar SHG on the polarization and focal geometry of the incident beams for the first time [43]. Then, in Chapter 3 we use the two-beam geometry to characterize and enhance SHG from silicon nanocrystal composites, which are macroscopically centrosymmetric [23]. Application of enhanced two-beam SHG in microscopy will be discussed in Chapter 2.8. Phase-matched quadrupolar SHG will be discussed in Chapter 4. Lastly, we discuss SHG *in situ* monitoring of silicon

nanocrystal growth by CVD in ultra-high vacuum chamber in Chapter 5.

Chapter 2

Quadrupolar SHG in glass

2.1 Introduction

Usually, quadrupolar SHG $\mathbf{P}_Q^{(2)}$ from centrosymmetric material simply contributes a weak, undesired background that interferes with the study of interface dipolar SHG [25,39]. However, the study of quadrupolar SHG is important in its own right. For example, study of quadrupolar SHG from an isotropic glass bulk can help to separate the bulk and surface contribution in a detailed polarization measurement [17]. The spatially-averaged dipolar SHG response of the interfaces of embedded centrosymmetric nano-spheres gives rise to a macroscopic quadrupolar SH polarization [14, 20, 31], which enables noninvasive SHG probing of the nano-interfaces [23]. In addition, bulk nonlinear susceptibilities of any type are more amenable to *ab initio* calculation than interface responses, making their measurement of interest for fundamental studies [5]. Finally, quadrupolar SHG could complement third-harmonic microscopy [3, 42] as a probe of biological samples by enabling use of shorter wavelength sources for which samples are transparent to second-, but not third-harmonic light. However, in the conventional single-beam geometry, quadrupolar SHG is usually exceedingly weak. Bethune *et al.* [6] showed that the quadrupolar SH polarization of an atomic vapor could be accessed by

using two intersecting, orthogonally polarized beams tuned to sharp atomic resonances. In this chapter, we study the completely nonresonant two-beam SH response of an isotropic fused silica slide. This simple material enables us to demonstrate quantitative features of two-beam SHG. In Section 2.2, we describe the quadrupolar SHG model and derive the SHG enhancement factor when two-beam geometry is used. Experimental observation of enhanced quadrupolar SHG is shown in Section 2.4. Then the model is tested more stringently using elliptically polarized beams, shown in Section 2.5. Phase mis-matched quadrupolar SHG from glass is well studied in the z-scan experiment, which is shown in Section 2.6. A new technique to prepare the sample – “sandwich” – is developed to measure the quadrupolar SH susceptibility and to discriminate the SH signal in Section 2.7.

2.2 Theory

In a homogeneous isotropic material, the nonlinear polarization is given by Equation 1.8. The magnetic dipole term $\gamma\nabla(\mathbf{E} \cdot \mathbf{E})$ is inseparable from surface contributions [39], but can be neglected when, as discussed below, the latter are negligible. The SH polarization then can be written as

$$\mathbf{P}_Q^{(2)} = (\delta - \beta - 2\gamma)(\mathbf{E} \cdot \nabla)\mathbf{E}. \quad (2.1)$$

In single-beam SHG, the component of $\nabla\mathbf{E}$ that radiates at 2ω originates from the transverse non-uniformity of the beam. Thus for a plane wave, $\nabla_{\perp}\mathbf{E} = 0$; for a Gaussian beam, $\nabla_{\perp}\mathbf{E} \sim |\mathbf{E}|/w_0$ (where w_0 =beam waist). In two-beam

SHG (see Figure 2.1), the SH-radiating component of $\nabla\mathbf{E}$ can become much larger if the polarization of each beam is properly set. For two plane wave fields $\mathbf{E}_i = \mathbf{E}_i^0 e^{i\mathbf{k}_i \cdot \mathbf{r}}$ (where $i = 1, 2$), Equation 2.1 becomes

$$\begin{aligned} \mathbf{P}_Q^{(2)} = & i(\delta - \beta - 2\gamma)\{\mathbf{E}_1^0 \cdot \mathbf{k}_1 \mathbf{E}_1^0 \exp(2i\mathbf{k}_1 \cdot \mathbf{r}) \\ & + \mathbf{E}_1^0 \cdot \mathbf{k}_2 \mathbf{E}_2^0 \exp[i(\mathbf{k}_1 + \mathbf{k}_2) \cdot \mathbf{r}] \\ & + \mathbf{E}_2^0 \cdot \mathbf{k}_1 \mathbf{E}_1^0 \exp[i(\mathbf{k}_1 + \mathbf{k}_2) \cdot \mathbf{r}] \\ & + \mathbf{E}_2^0 \cdot \mathbf{k}_2 \mathbf{E}_2^0 \exp(2i\mathbf{k}_2 \cdot \mathbf{r})\}. \end{aligned} \quad (2.2)$$

The first and last terms in braces vanish since the electromagnetic wave vector is always perpendicular to the electric field for each laser beam in the plane wave approximation. If $\mathbf{E}_1 \parallel \mathbf{E}_2 \parallel \hat{y}$ (see axes in Figure 2.1), then $\mathbf{E}_1 \cdot \mathbf{k}_2$ and $\mathbf{E}_2 \cdot \mathbf{k}_1$ vanish, and $\mathbf{P}_Q^{(2)} = 0$. If each beam is polarized in the $\hat{x} - \hat{z}$ plane, then $\mathbf{P}_Q^{(2)}$ points along the propagation direction $(\mathbf{k}_1 + \mathbf{k}_2)$ (see Appendix 1 for derivation), and therefore, does not radiate. However, if $\mathbf{E}_1 \perp \mathbf{E}_2$ (e.g., $\mathbf{E}_1 \parallel \hat{x}$, $\mathbf{E}_2 \parallel \hat{y}$), then $\mathbf{E}_2 \cdot \mathbf{k}_1$ vanishes, but $\mathbf{E}_1 \cdot \mathbf{k}_2$ does not, and $\mathbf{P}_Q^{(2)} \parallel \mathbf{E}_2$ (i.e. *S*-polarized). $\mathbf{P}_Q^{(2)}$ scales as $\mathbf{E}_1 \cdot \mathbf{k}_2$, i.e. $(|\mathbf{E}_1|/\lambda_2) \sin \alpha'$, where α' is the angle between two beams inside the sample, and λ_2 is the wavelength of beam 2. Compared to single beam SHG, $|\mathbf{P}_Q^{(2)}|$ is enhanced by a factor $(w_0/\lambda_2) \sin \alpha'$, and SHG intensity by a factor $(w_0/\lambda_2)^2 \sin^2 \alpha'$.

2.3 Experimental setup

We use an unamplified (810nm, 100fs, 76MHz, 0.9nJ/pulse) and also an amplified Ti:Sapphire (810nm, 100fs, 1KHz, 0.5mJ/pulse) laser in our ex-

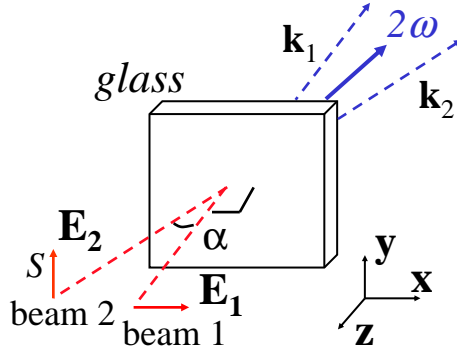


Figure 2.1: Two-beam SHG configuration. Beam 1 is normally incident onto the glass sample and polarized horizontally (in \hat{x} direction). The incident angle of Beam 2 is 20° . Its polarization can be tuned through a $\lambda/2$ plate.

periments. The diagram of the experimental setup is shown in figure 2.2. The laser beam passes through a lens then is split 50/50 into two beams. One beam (beam 2) is reflected by a mirror and then impinges obliquely on the sample (incident angle = 20°). The other beam (beam 1) goes through a delay stage and is then normally incident onto the sample. Those two beams are spatially and temporally overlapped on the sample. On beam 1, we also setup a $\lambda/2$ wave-plate so that we can change the polarization direction of beam 1. The sample is mounted on a 3-D micro-stage, so that it can be precisely positioned. After the sample, along the bisector of two fundamental beams, we set up a photomultiplier tube (PMT) to detect the 2-beam SHG. To suppress the fundamental light background, a monochromator and several blue glass filters (BG39, Schott color glass filter) are set up before the PMT. We confirmed that two-beam SHG detected by the PMT contained only frequencies within the doubled fundamental spectrum and depended on temporal overlap of the

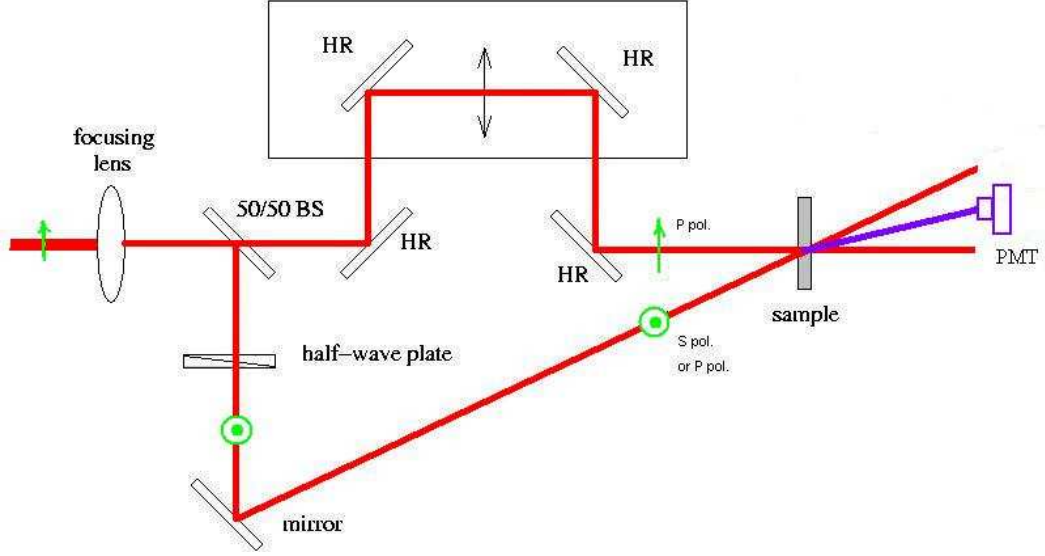


Figure 2.2: Two-beam SHG experimental setup.

incident pulses. We also confirmed that the intensity of the SHG obeyed the square intensity law ($I_{2\omega} \propto I_{\omega}^2$).

2.4 Enhanced 2-beam SHG from glass

We set the polarization of \mathbf{E}_1 in the horizontal direction (\hat{x}), then we rotate the polarization of \mathbf{E}_2 from the vertical direction (\hat{y}) to the horizontal direction (\hat{x}). At the same time, we count the 2-beam SH photons with the PMT. As shown in Figure 2.3, the SHG signal decrease monotonically to the noise level when the beam polarizations change from orthogonally polarized to co-polarized. This agrees very well with the prediction from the model described in Section 2.2.

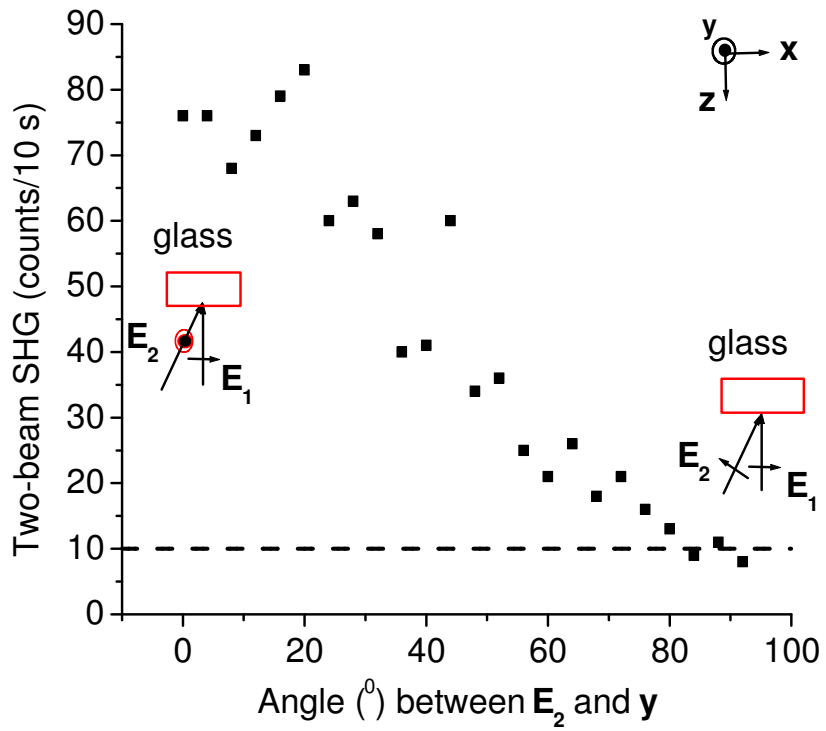


Figure 2.3: Two-beam SHG with unamplified laser as \mathbf{E}_2 rotates from vertical (\hat{y}) to horizontal (P -polarized), with \mathbf{E}_1 fixed along \hat{x} . The SH radiation was completely \hat{y} -polarized. Dashed line: dark count level.

The possibility that SHG from the glass surfaces contributes to the 2-beam SHG signal can be ruled out either on symmetry or experimental grounds, depending on the polarization configuration. When $\mathbf{E}_1 \parallel \hat{x}$ and $\mathbf{E}_2 \parallel \hat{y}$, surface SHG requires a susceptibility tensor component $\chi_{ixy}^{(2)}$ ($i = x, y$ or z), which vanishes for the surface of an isotropic material like glass. Thus there is no surface SH polarization in this configuration. If we rotate \mathbf{E}_2 to the $\hat{x} - \hat{z}$ plane (P -polarized), then a surface-like polarization $\mathbf{P}^{(2)} = \hat{z}\tilde{\chi}_{zxx}^{(2)}E_1^xE_2^x + \hat{x}\chi_{xxz}^{(2)}E_1^xE_2^z$ becomes allowed, where $\tilde{\chi}_{zxx}^{(2)} = \chi_{zxx}^{(2)} + \varepsilon^{-1}(2\omega)\gamma$ is an effective surface susceptibility component [18] that includes the inseparable bulk contribution $\gamma\nabla(\mathbf{E} \cdot \mathbf{E})$ and $\varepsilon(2\omega)$ is the dielectric constant at 2ω . However, as shown in Figure 2.3, no 2-beam SHG signal is observed in this configuration. Likewise a single P -polarized beam, which produces a similar polarization $\mathbf{P}_j^{(2)} = \hat{z}\tilde{\chi}_{zxx}^{(2)}E_j^xE_j^x + \hat{x}\chi_{xxz}^{(2)}E_j^xE_j^z$ ($j = 1, 2$), produces negligible SHG signal. Therefore, we can rule out observable surface-like SHG contributions originating from surface dipole and magnetic dipole terms.

The quadrupolar SHG model also predicts that the SH field is polarized normal to the plane described by the two fundamental beams. For example, when $\mathbf{E}_1 \parallel \hat{x}$ and $\mathbf{E}_2 \parallel \hat{y}$, the Equation 2.2 becomes,

$$\mathbf{P}_Q^{(2)} = i(\delta - \beta - 2\gamma)\{\mathbf{E}_1^0 \cdot \mathbf{k}_2\mathbf{E}_2^0 \exp[i(\mathbf{k}_1 + \mathbf{k}_2) \cdot \mathbf{r}]\}. \quad (2.3)$$

So the SH polarization is in the same direction as \mathbf{E}_2^0 (\hat{y} direction), which is perpendicular to the plane decided by the two crossed beams (plane $\hat{x} - \hat{z}$). Our experimental result shown in Figure 2.4 agrees very well with the prediction by the model.

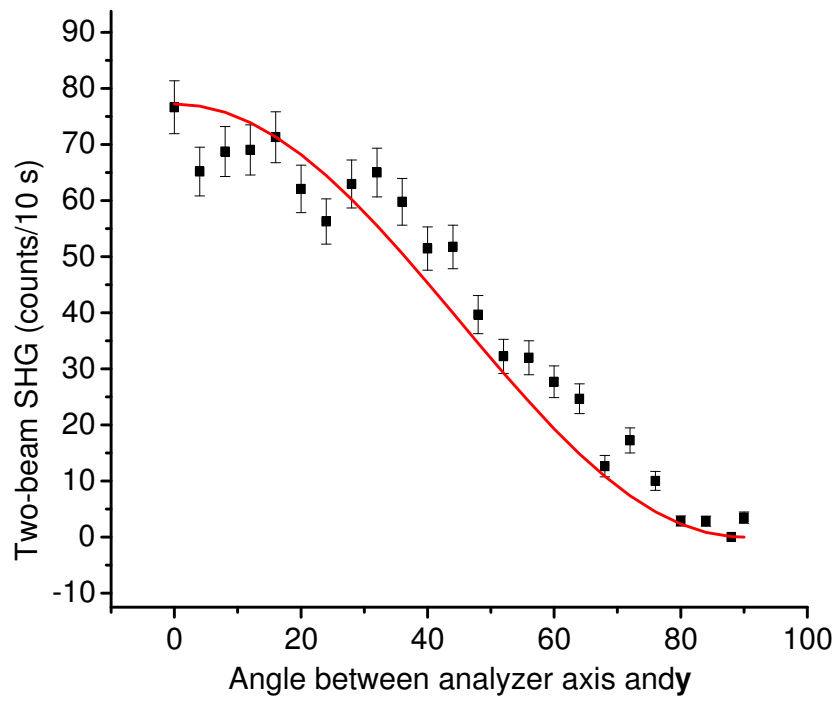


Figure 2.4: Two-beam SHG signal for $\mathbf{E}_1 \parallel \hat{x}$, $\mathbf{E}_2 \parallel \hat{y}$ observed through polarization analyzer, showing signal polarized along \mathbf{E}_2 .

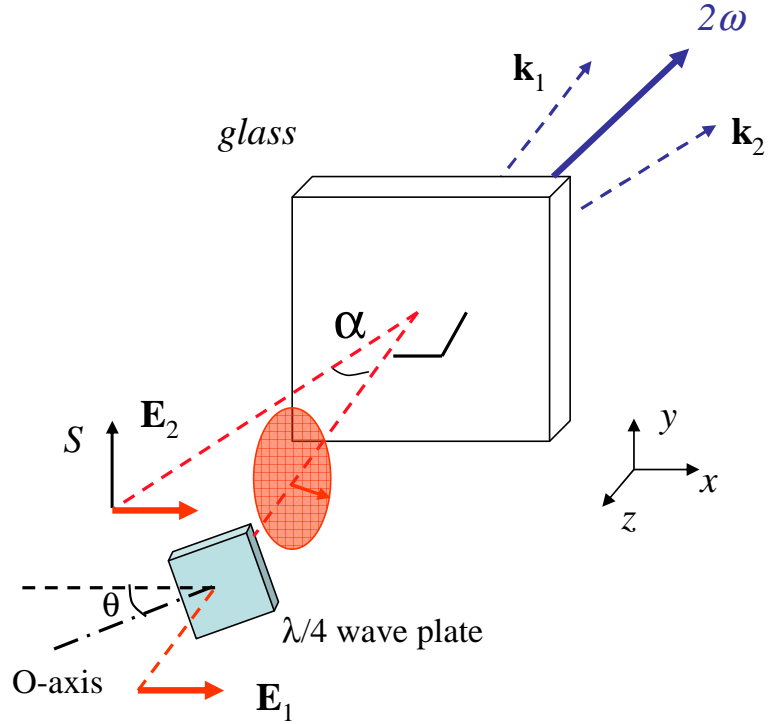


Figure 2.5: Experimental setup. The normally incident beam passes through a $\lambda/4$ waveplate before reaching the sample. The oblique incident beam is linearly polarized. Its polarization can be set in the horizontal (\hat{x}) or in the vertical (\hat{y}) by a $\lambda/2$ waveplate.

2.5 SHG from glass using elliptically polarized beams

To test the completeness of Equation (2.2) in describing quadrupolar 2-beam SHG more stringently, we compared its predictions for elliptically-polarized incident beams to experimental observations.

With \mathbf{E}_2 linearly polarized we controlled the ellipticity of \mathbf{E}_1 by varying the angle θ between \mathbf{E}_1 and the O-axis of a $\lambda/4$ plate lying in the $\hat{x}-\hat{y}$ plane (see Figure 2.5). \mathbf{E}_1 entered the $\lambda/4$ plate polarized along \hat{x} , and emerged in the

form $\mathbf{E}_1[\hat{x}(\sin^2 \theta + i \cos^2 \theta) + \hat{y}(1 + i) \sin \theta \cos \theta]$. When $\mathbf{E}_2 \parallel \hat{y}$, Equation (2.2) predicts that only the \hat{x} component of \mathbf{E}_1 couples with \mathbf{E}_2 to create $\mathbf{P}_Q^{(2)}$, resulting in SHG intensity proportional to $(|\mathbf{E}_1|^2 |\mathbf{E}_2|^2)(\cos^4 \theta + \sin^4 \theta)$. Similarly when \mathbf{E}_2 is P-polarized, Equation (2.2) predicts SHG intensity proportional to $2|\mathbf{E}_1|^2 |\mathbf{E}_2|^2 \cos^2 \theta \sin^2 \theta$. The experimental results, shown in Figure 2.6, agree very well with these predictions. On the other hand, if surface-like contributions present, the SHG would have shown very different θ -dependence. For example, Cattaneo *et al.* [18] found that the reflected surface SHG θ -dependence was totally opposite to the transmission bulk SHG from a BK7 glass slide.

2.6 SHG from glass by z-scan

Phase mismatch was characterized by z-scan (translating the sample in \hat{z} direction, the coordinate is shown in Figure 2.1) of the sample position through the 2-beam overlap. We used both unamplified and amplified Ti:Sapphire laser pulses to provide tightly focused beams ($w_1 = 20\mu m$, $w_2 = 10\mu m$) and loosely focused beams ($w_1 = w_2 = 500\mu m$).

With the tightly focused beams, for which the sample thickness $h = 900\mu m \gg 250\mu m$ (length of the overlap region), the signal peaked sharply when the front or rear surface was centered on the overlap, as shown in Figure 2.7.

An analogous enhancement occurs in third-harmonic microscopy when sample boundaries fall within the Rayleigh range of a tightly focused beam. For our case, the length of the overlap region is much less than the confocal

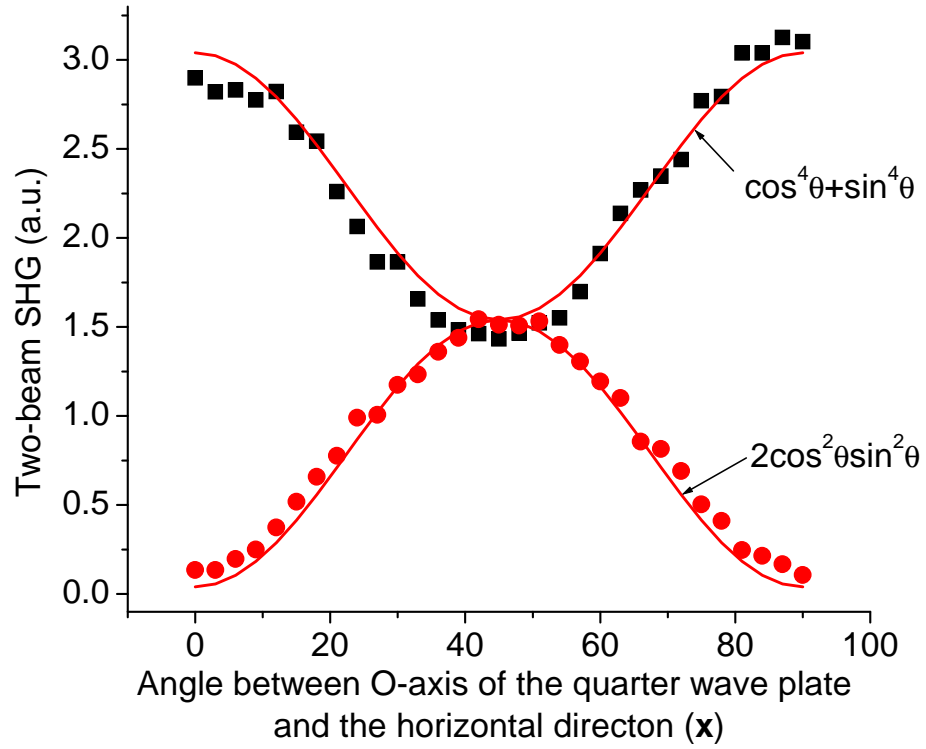


Figure 2.6: Two beam SHG signal vs. ellipticity of beam 1 polarization. Squares (circles) correspond to $\mathbf{E}_2 \parallel \hat{y}$ (\mathbf{E}_2 P-polarized). Curves are calculations based on Equation 2.2.

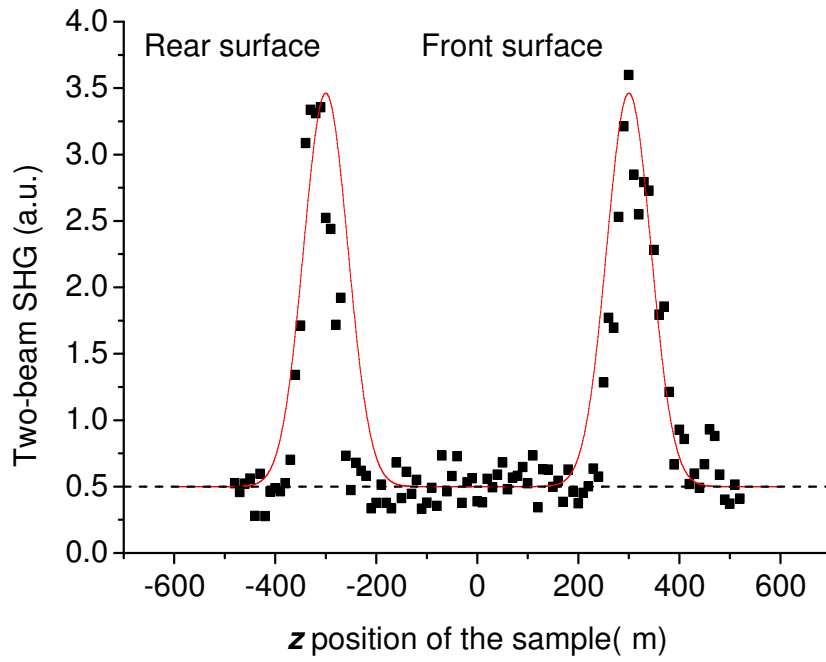


Figure 2.7: Measured (solid squares) and calculated (solid line) SHG intensity as the sample is scanned longitudinally (in \hat{z} direction) along the 2-beam overlap region of tightly focused unamplified beams. Dashed line: dark count level.

region $2z_R \sim 4.4, 1.1\text{mm}$ of either beam, the well-known effects of the Guoy phase shift on harmonic generation by focused beams [11] are negligible in our geometry. These peaks result not from interface SHG, but from relaxation of phase mismatch when boundaries of the sample fall within the 2-beam overlap region. The SHG field is proportional to:

$$\int_{-h/2-Z'}^{h/2-Z'} \exp\left[-\frac{(z \tan \alpha')^2}{w_1^2 + w_2^2 / \cos^2 \alpha'}\right] \exp(i\Delta k z) dz, \quad (2.4)$$

where $Z' = -Z \tan \alpha / \tan \alpha'$ is the position of the beam intersection ($z = 0$) measured from the center Z of the slide, $\Delta k = \hat{z} \cdot (\mathbf{k}_1 + \mathbf{k}_2 - \mathbf{k}_3)$ is the wave-vector difference between the SH polarization and generated SH light, and $\exp[-(z \tan \alpha')^2 / (w_1^2 + w_2^2 / \cos^2 \alpha')]$ is the amplitude of the SH polarization resulting from the intersection of two Gaussian profiles, $\Delta k z$ is the phase of the SH polarization at different z position. The integral of the SH polarization over the sample is illustrated in Figure 2.8.

When the 2-beam overlap (SHG active region) is totally in the glass, the positive and negative parts of the SH polarization are almost equal, so there is no net SH polarization after integration. However, if only part of the overlap is in the glass, then the integral gives a non-vanishing SH polarization. That's how the double peaks appear in the z -scan experiments. If Guoy phase through the overlap region is included, the results are nearly unaffected, as shown in Figure 2.9.

For contrast, Figure 2.10 shows a z -scan for amplified loosely focused beams for which $h \sim w_{1,2} = 500\mu\text{m}$. In this case only one peak is observed

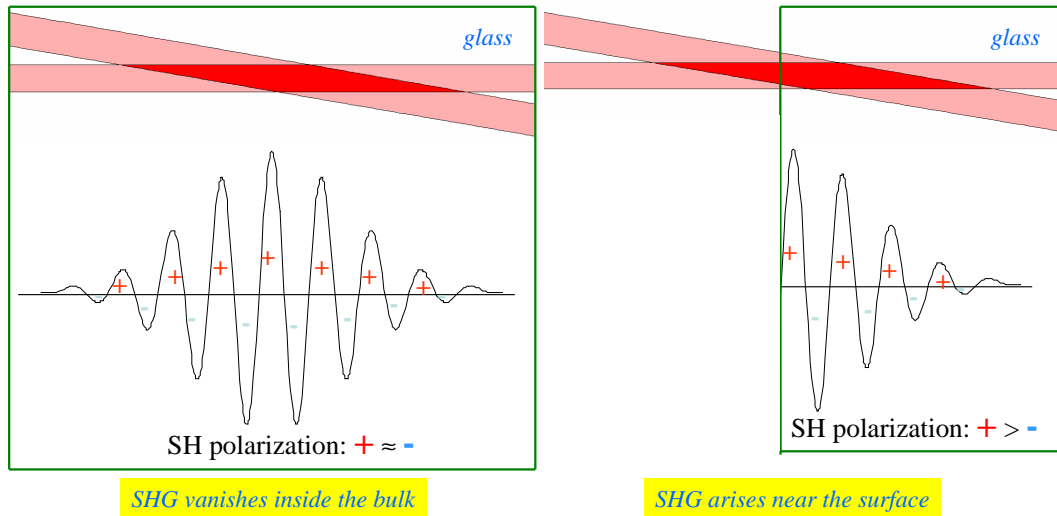


Figure 2.8: The integral of the 2-beam SH polarization vanishes when the 2-beam overlap is totally inside the glass bulk (left figure), but does not vanish when only part of the overlap is in the glass bulk (right figure).

(data points) and predicted (solid curve). Thus, in general, axial resolution in probing gradients in the optical properties is optimized with tightly focused intersecting beams, while signal enhancement $(w_0/\lambda_2)^2 \sin^2 \alpha'$ over single beam SHG is maximized with loosely focused beams.

2.7 “Sandwich” experiment

The integral of 2-beam SH polarization over a uniform medium vanishes as long as the 2-beam overlap region is totally inside the medium. However, the integral doesn’t vanish if the overlap region falls on a surface of the medium, as shown in Section 2.6. How about the internal surfaces within a bulk materials? Do they also generate 2-beam SHG?

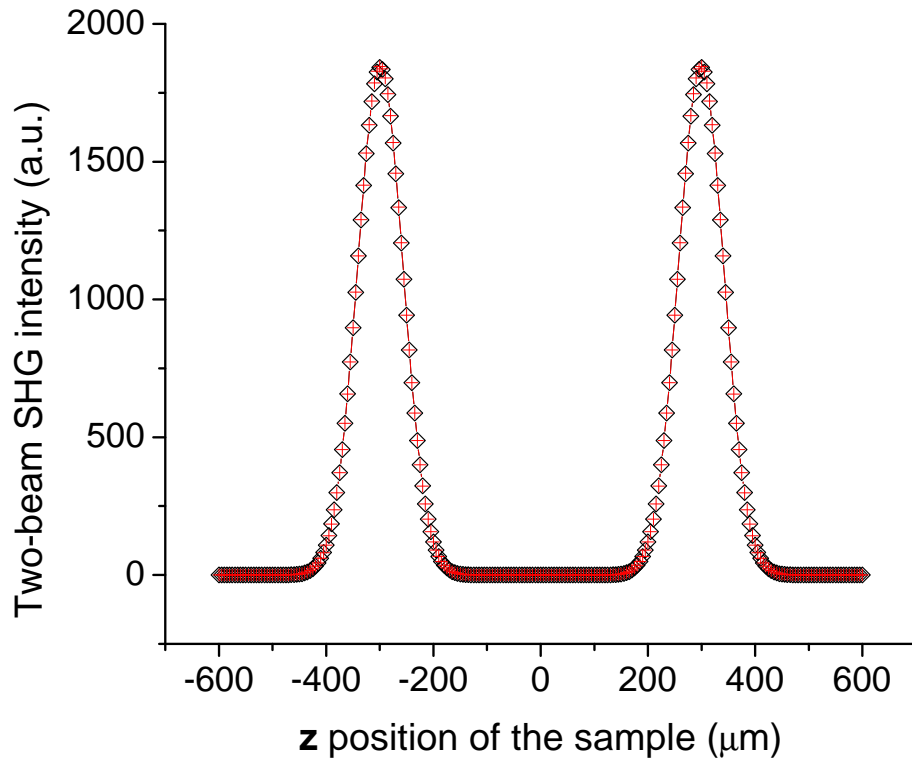


Figure 2.9: Calculated SHG intensity as the sample is scanned longitudinally (in \hat{z} direction) along the 2-beam overlap region of tightly focused unamplified beams. Cross: Guoy phase included; Diamond: Guoy phase not included.

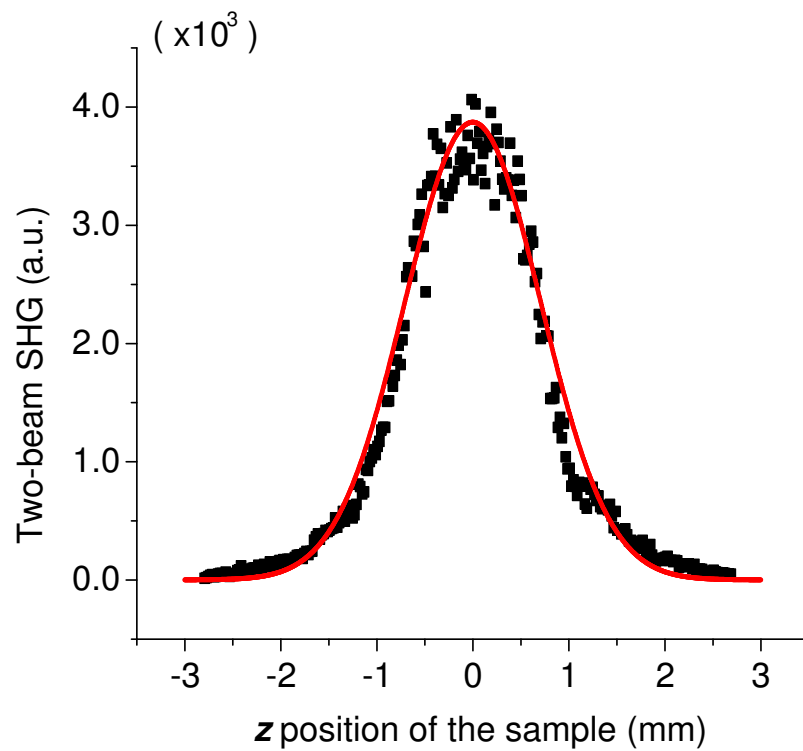


Figure 2.10: Measured (solid squares) and calculated (solid line) SHG intensity as the sample is scanned longitudinally (in \hat{z} direction) along the 2-beam overlap region of loosely focused amplified beams.

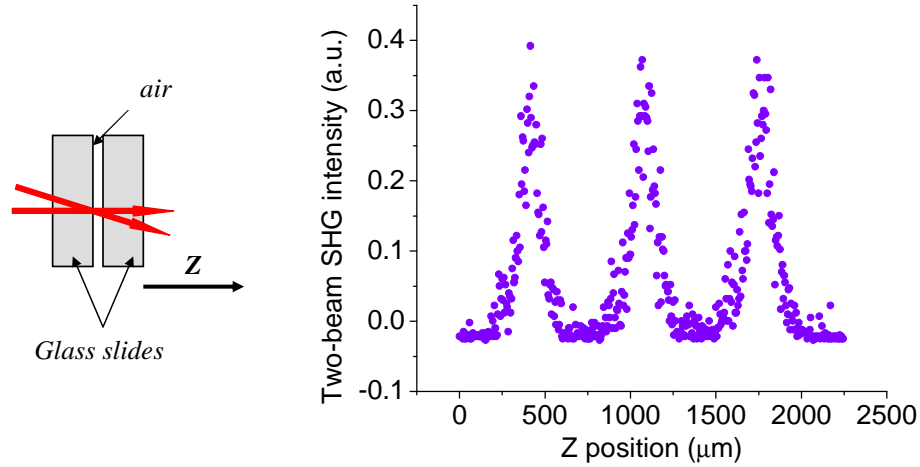


Figure 2.11: Left: z-scan of the overlap of two laser beams through two stacked glass slides with an air gap in between; right: 2-beam SHG shows three peaks along the z-direction.

In this experiment, we stacked two 1 mm thick glass slides together. The air gap which is about several microns wide forms two internal surfaces. We call it “sandwich” experiment since it is like that a layer of air is sandwiched in between two glass slides. The Spitfire laser beam (250fs, 1kHz, 800nm) was split into two beams, focused to about $20\mu\text{m}$ in diameter and overlapped with each other onto the sample. When the sample was z-scanned through two-beam overlap, we observed a non-vanishing 2-beam SHG from the air gap (see the middle peak in Figure 2.11). This result shows that the internal surfaces inside a isotropic bulk can also generate strong 2-beam SHG. In other words, 2-beam SHG can be used to probe internal surfaces inside transparent bulk materials.

Further experiment shows, the SHG from the gap can be depressed by

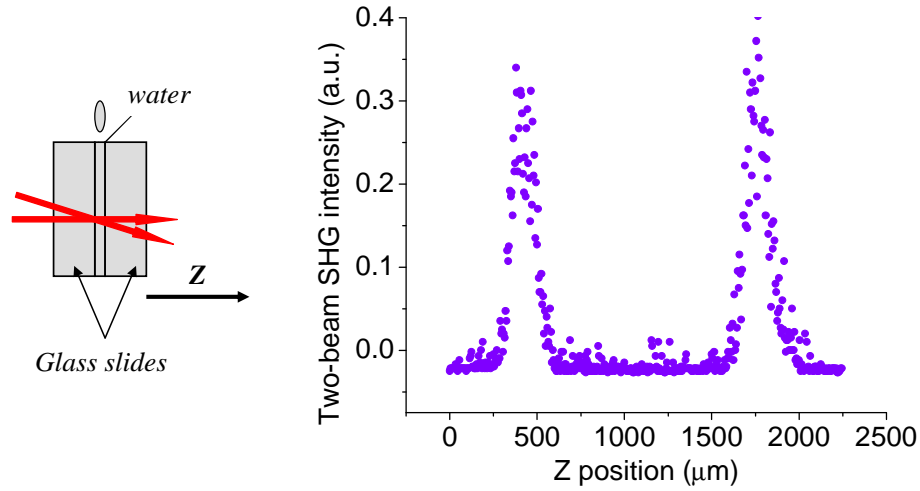


Figure 2.12: Left: z-scan of the overlap of two laser beams through two stacked glass slides with a water gap in between; right: 2-beam SHG shows two peaks along the z-direction.

filling the gap with water (see Figure 2.12). This is because the glass and the water have similar refractive indices and nonlinear susceptibilities, which make the sandwiched sample (glass/water/glass) like a single uniform bulk sample. In that case, the 2-beam SHG vanishes as long as the two-beam overlap is totally inside the sample.

Our simulation also shows that the magnitude of the SHG from the gap is sensitive to the magnitude of the SH susceptibility and the linear refractive index of the material being sandwiched. In Figure 2.13, we simulated the 2-beam SHG peaks in z-scan experiment. We used the model described by Formula 2.4, and set the gap size to be $5 \mu\text{m}$ and the glass SH susceptibility to be an unknown constant $\chi_Q^{(2)}(\text{glass})$, together with the known parameters: the

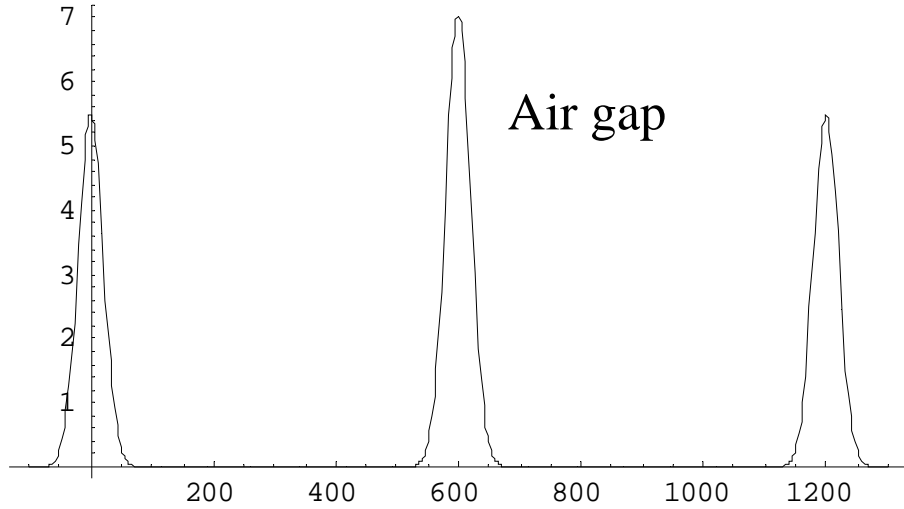
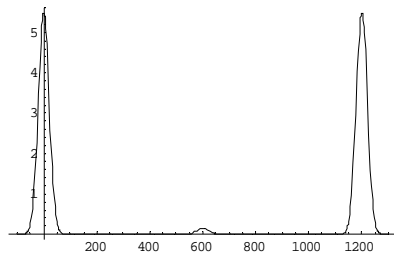


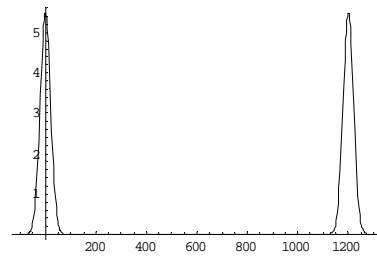
Figure 2.13: Simulated 2-beam SHG peaks when the sandwiched sample (glass/air/glass) is z-scanned through the 2-beam overlap.

air refractive indices $n_{air}^{\omega} = n_{air}^{2\omega} = 1$, the air SH susceptibility $\chi_Q^{(2)}(air) = 0$, and the glass refractive indices $n_{glass}^{\omega} = 1.45332, n_{glass}^{2\omega} = 1.47013$. Then we simulated 2-beam SHG peaks for glass/water/glass sandwiched sample, by setting the water SH susceptibility $\chi_Q^{(2)}(water)$ to be 0.7, 0.8, 0.9, 1.2 times of $\chi_Q^{(2)}(glass)$ with the known parameters: the water refractive indices $n_{water}^{\omega} = 1.329, n_{water}^{2\omega} = 1.339$. If $\chi_Q^{(2)}(water) = 0.8\chi_Q^{(2)}(glass)$, the SHG from water gap vanishes, as shown in Figure 2.14. It is interesting that the SHG always vanishes as long as $\chi_Q^{(2)}(water) = 0.8\chi_Q^{(2)}(glass)$, and it is independent of the gap size, which is shown by another simulation.

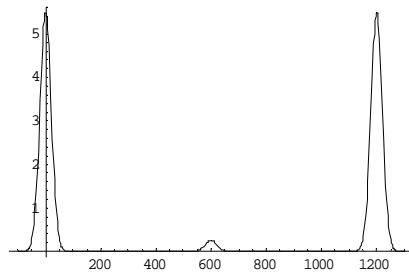
The above result shows the “sandwich” experiment can be used to measure the quadrupolar SH susceptibility of any fluid which can be sandwiched in between two glass slides. Moreover, some nano-structured materials and



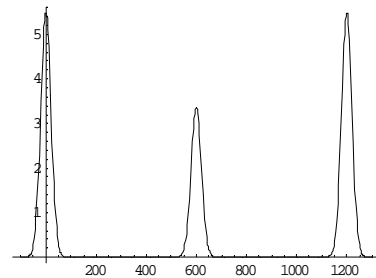
$$\chi^{(2)}_{\text{water}} = 0.7\chi^{(2)}_{\text{glass}}$$



$$\chi^{(2)}_{\text{water}} = 0.8\chi^{(2)}_{\text{glass}}$$



$$\chi^{(2)}_{\text{water}} = 0.9\chi^{(2)}_{\text{glass}}$$



$$\chi^{(2)}_{\text{water}} = 1.2\chi^{(2)}_{\text{glass}}$$

Figure 2.14: Simulated 2-beam SHG peaks when the sandwiched sample (glass/water/glass) is z-scanned through the 2-beam overlap. The middle SHG peak depends on the SH susceptibility of water.

bio-materials (e.g. cells) can also be sandwiched in between the two glass slides to be measured by 2-beam SHG. With an objective lens set behind the sample, we can also do microscopical SHG study on those materials.

2.8 Two-beam SHG microscopy

Optical SHG was first used for microscopy by Hellwarth and Christensen [26] (1974) and Sheppard *et al.* [38] (1977). SHG microscopy was applied to biological sample by Freund and colleagues in 1986. Since then, SHG microscopy gained broad applications [15]. The advantage of SHG microscopy over linear optical microscopy lies on its sensitivity to interfaces, which make it possible to see some transparent samples. To image centrosymmetric material, usually third-harmonic generation (THG) is used, since any material has nonvanishing third-harmonic (TH) susceptibility [3, 42]. In our study on quadrupolar SHG in glass, we successfully enhanced the SHG from centrosymmetric materials using two orthogonally polarized laser beams [43]. This in principle enables SHG microscopy to centrosymmetric materials, so that it can compliment THG microscopy for imaging samples that are transparent to SH photons, but not TH photons. In this section, we describe a few preliminary attempts to demonstrate this concept. These preliminary results are intended only as a prelude to a more extensive study of two-beam SHG microscopy.

We first chose ZnO micro-clusters for SHG microscopy. ZnO crystals are noncentrosymmetric and it has large dipolar SH susceptibility. They were used to exam our imaging system at that time, and maybe later will be used

in bio-labeling. The ZnO sample was prepared by chemical growth of ZnO nanorods ($\sim 100\text{nm}$ in diameter) and then depositing them on a glass cover slide. The ZnO nanorods tended to form big clusters. We picked up a cluster of a few microns to do linear and SH imaging. In Figure 2.15 (a) and (b), the linear imaging of the cluster is shown. The SH image of the same cluster is shown in Figure 2.15 (c). The size of the cluster is estimated to be $4.8\mu\text{m}$ by counting the pixels occupied the image (see Figure 2.16).

To demonstrate microscopy with quadrupolar SHG, we chose a glass cover slide ($150\mu\text{m}$ thick) in our experiment. We made a scratch (width is about $15\mu\text{m}$) on the glass surface so that we could use it as a reference feature. The sample was translated so that the scratch was close to the two-beam overlap. The SHG image of the glass away from the scratch is much brighter when the two beams were orthogonally polarized (Fig. 2.17 (a) and Fig. 2.18 (a)) than co-polarized (Fig. 2.17 (b) and Fig. 2.18 (b)). However, the image of the scratch was much brighter when the two beams were co-polarized. This is what we expect, the two orthogonally polarized beams enhanced the centrosymmetric bulk quadrupolar SHG, while the co-polarized two beams probe the interface dipolar SHG.

The above results shows our apparatus for two-beam SHG microscopy are ready. By tuning the polarization of the two laser beams, we can selectively image the centrosymmetric or noncentrosymmetric materials. This technique can be applied on microscopy of nanostructured material and biological materials.

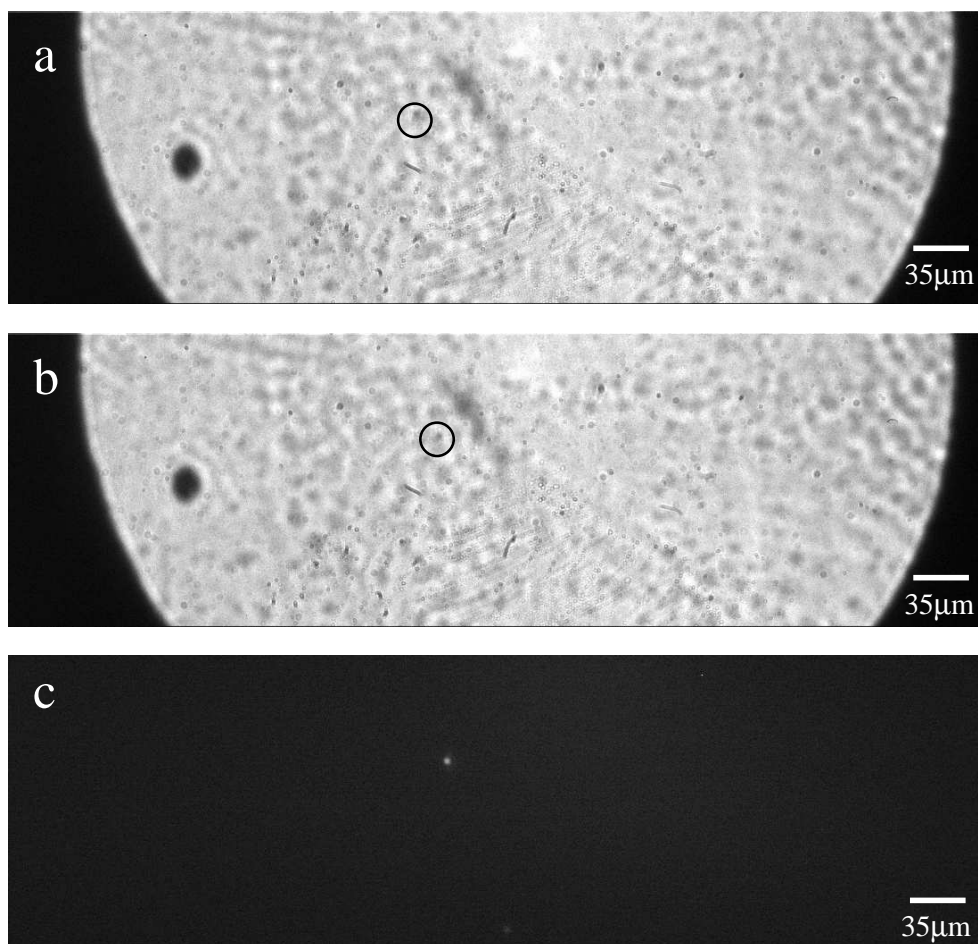


Figure 2.15: Linear (a, b) and SH (c) images of a ZnO cluster. From (a) to (b), the sample was shifted so that the image of the ZnO particle can be distinguished from the background.

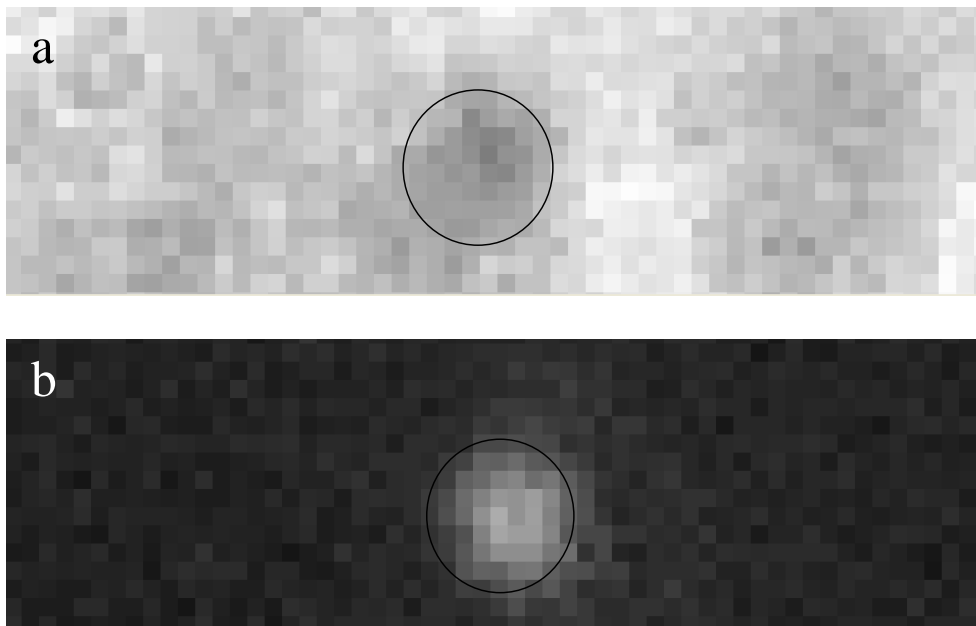


Figure 2.16: Linear (a) and SH (b) images of a ZnO cluster show the size of the cluster is the same ($\sim 4.8\mu\text{m}$) in either case.

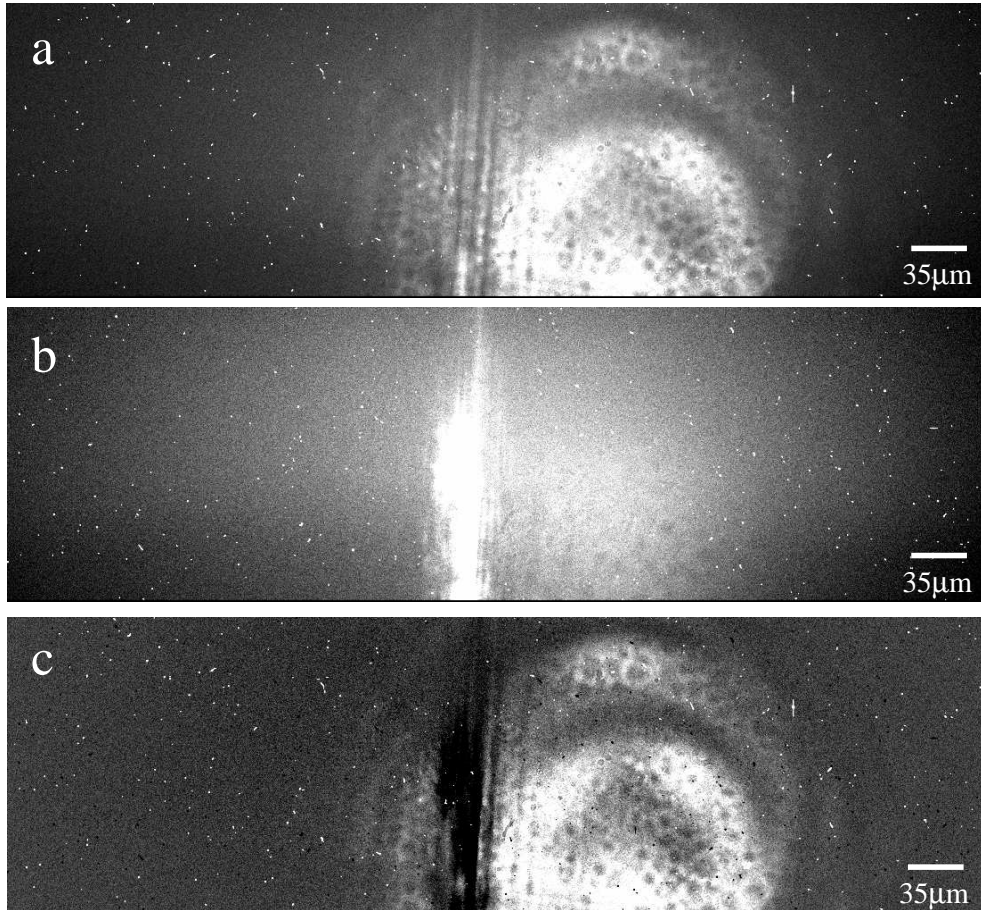


Figure 2.17: 2-beam SHG image of a glass slide with a scratch on one surface. (a) Straight beam (beam 1) is horizontally polarized (in \hat{x}), angled beam (beam 2) is vertically polarized (in \hat{y}). (b) Both beams are polarized in $\hat{x} - \hat{z}$ plane. (c) Difference of image in (a) and in (b).

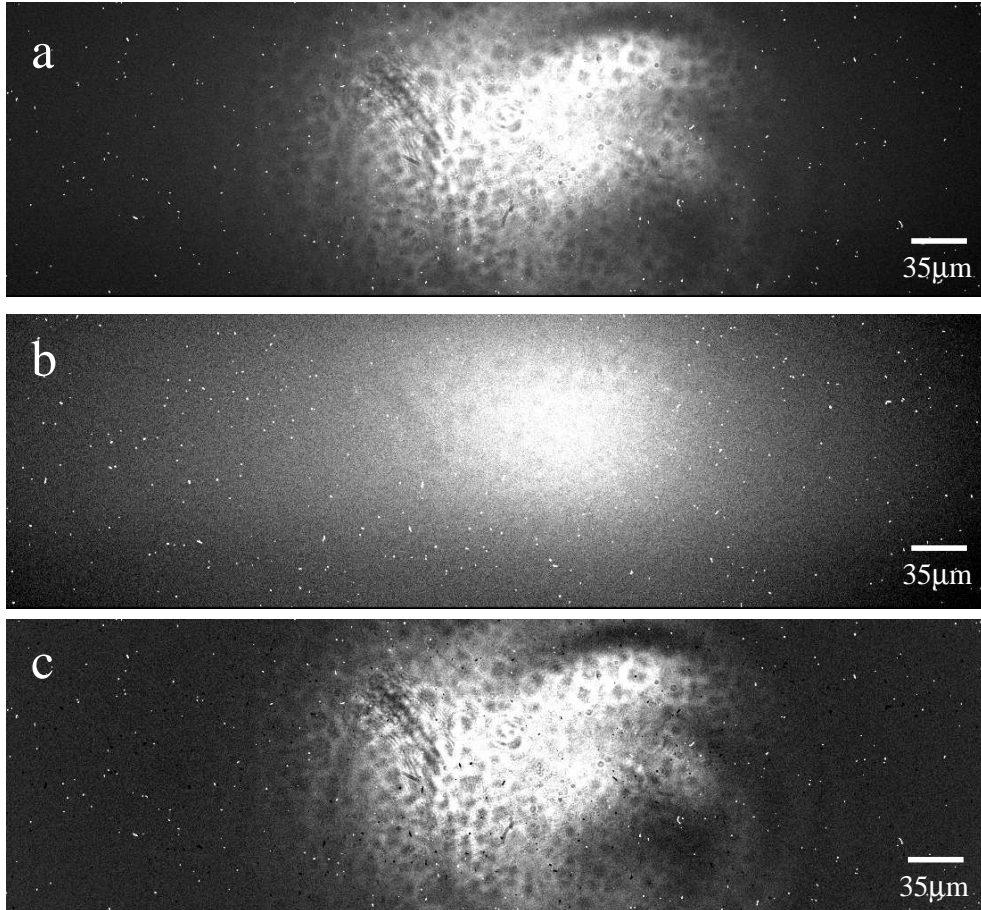


Figure 2.18: 2-beam SHG image of a glass slide with a scratch on one surface. (a) Straight beam (beam 1) is horizontally polarized (in \hat{x}), angled beam (beam 2) is vertically polarized (in \hat{y}). (b) Both beams are polarized in $\hat{x} - \hat{z}$ plane. (c) Difference of the image in (a) and the image in (b).

2.9 Conclusion

In conclusion, we have demonstrated the quantitative features of a general two-beam technique for enhancing the quadrupolar SHG response of isotropic materials. The quadrupolar SH polarization model is completely test by several experiments. The phase mismatch issues which related the fundamental and the SH wave propagating inside the sample are studied in detail through both experimental and theoretical approaches. Applications include the study of nano-composites of centrosymmetric materials [23] and second-harmonic microscopy of transparent samples.

Chapter 3

Quadrupolar SHG in silicon nanocrystals

3.1 Introduction

Silicon nanocrystals have unique optical and electrical properties that are lacking in bulk silicon. For example, silicon nanocrystals can emit light very efficiently. Optical gain in silicon nanocrystals embedded in glass was recently observed [32], which may make it possible to build a silicon laser. Another interesting property of the silicon nanocrystal is that it can trap electrons efficiently [46]. This feature has been utilized to make silicon-nanocrystal-based flash memory . Though the microscopic mechanisms behind those properties are still under debate, it is widely accepted that quantum confinement due to nanocrystal size and the nano-interfaces between the nanocrystals and the host material are responsible for those optical and electrical properties.

Second harmonic generation (SHG) as a non-contact, non-invasive optical probe method has already been used for about four decades. It has been widely used as a planar in bulk and interface/surface probe. It started to be used to probe nano-interfaces only in recent years [14, 20, 28, 31, 34, 44]. Since composites of randomly oriented nanocrystals are macroscopically centrosymmetric, dipolar SHG is forbidden. The SHG from such materials is

quadrupolar, which is extremely weak when the traditional single beam SHG setup is used. In this chapter, we investigate both single-beam and two-beam SHG from composites of Si nanocrystals. A new 2-beam SHG configuration is discovered. It is found to enhance quadrupolar SHG from nanocrystals by a factor of 10^3 .

3.2 Sample preparation

The silicon nanocrystal samples were prepared in Oak Ridge National Lab. Silicon ions were implanted into a glass (Corning 7940) substrate and then annealed to form silicon nanocrystals. Multi-energy (35keV \sim 500keV) silicon ions were implanted, yielding a flat ion distribution in depth (1 μ m) (see Figure 3.1). Two groups of sample were annealed at about 1100 $^{\circ}$ C in two different gas environments, pure Ar gas and Ar + 4% H₂ gas, to allow a comparison of samples with as-precipitated and H-terminated nano-interface, respectively. The size of the nanocrystals was controlled by the dose of the silicon ions, annealing temperature and the annealing time.

A macroscopic picture of a typical silicon nanocrystal sample is show in Figure 3.2 (a). It has a central yellow area where nanocrystals are embedded. The transparent margin which is about 1 mm wide has no Si nanocrystals embedded, and thus serves as a control sample in the SHG experiments. Figure 3.2 (b) shows the cross-section TEM micrograph of a single silicon nanocrystal about 5 nm big in diameter embedded in glass.

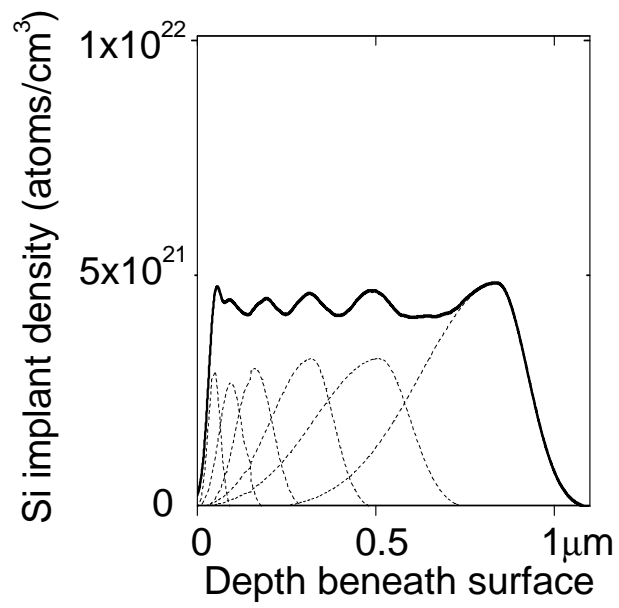


Figure 3.1: composite density profile (solid curve) for excess Si $5 \times 10^{21} \text{cm}^{-3}$, $\langle d_{NC} \rangle = 3 \text{ nm}$ of depth $L_{\text{implant}} \sim 1 \mu\text{m}$ formed by Si ion implantation at six different energies (dotted curves).

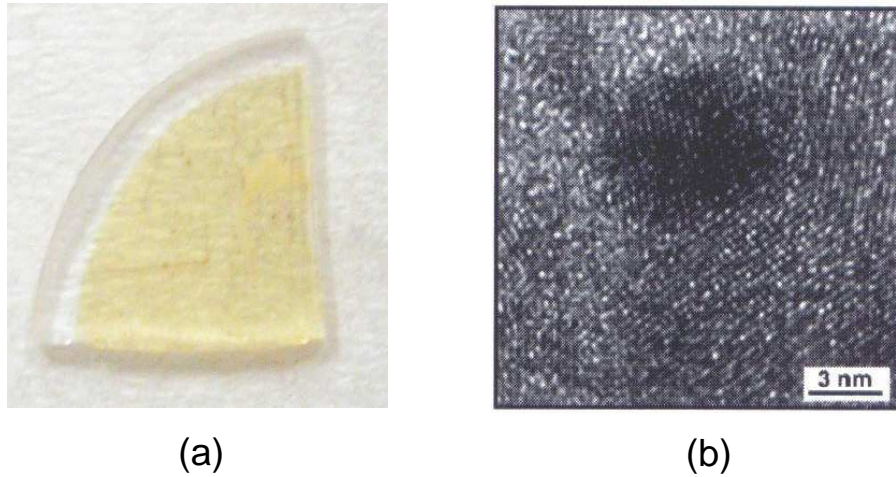


Figure 3.2: (a) A typical silicon nanocrystal sample. The yellow region is where Si nanocrystals are embedded, while the transparent margin is pure glass. (b) Cross-section TEM micrograph of a typical single silicon nanocrystal embedded in a glass substrate [49, 51]. The NCs with average diameter $\langle d \rangle_{NC}=3, 5$ and 8 nm, respectively (with 30% size fluctuation), with corresponding NC densities $n_{NC} = 7, 3$ and $1.5 \times 10^{18} cm^{-3}$ were formed under different conditions.

3.3 Single beam SHG from Si nanocrystals

Our first SHG measurement on NC-embedded fused silica was done by using a regeneratively amplified Ti:sapphire laser (200 fs, 300 nJ pulses at 250 kHz repetition rate and 800 nm central wavelength). Pulses were focused at normal incidence to spot radius 10 μm onto the samples. SHG from the isotropic glass surface vanishes in this configuration. SHG was collected in the forward direction and at small off-forward scattering angles. We used the lower repetition rate amplifier to avoid multi-pulse thermal heating damage in the fused silica samples.

Signals were normalized to reference SHG from a crystalline z-cut quartz plate [24] by a split-off portion of the fundamental beam. SHG signals were detected by photomultiplier tubes after Schott glass filters and gated to a photon counter, or by a cooled charge coupled device (CCD) camera. We confirmed that the detected signals obeyed quadratic intensity dependence, and contained only frequency components within the frequency-doubled fundamental spectrum.

3.3.1 Sensitivity to surface chemistry

A lateral scan of transmitted SHG as the linearly polarized focused excitation beam was translated across the boundary between Si implanted glass and unimplanted glass is shown in Figure 3.3. Two samples were used in this experiment. Both sample had $\langle d \rangle_{NC} \sim 3\text{nm}$ Si nanocrystals embedded. The only difference was, one sample was annealed in Ar, the other

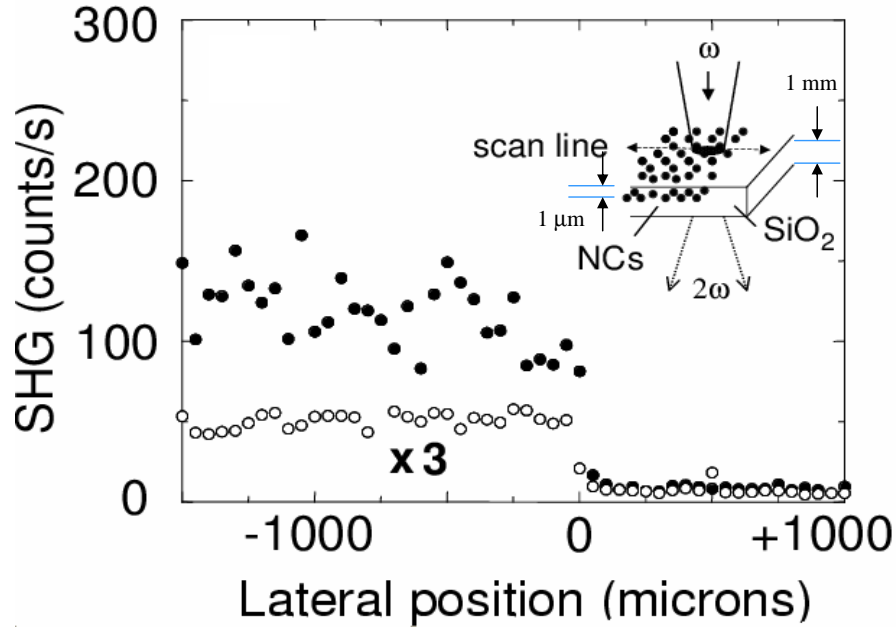


Figure 3.3: Scan of single-beam SHG across the boundary between Si NC implant and unimplanted glass rim at edge of sample. $x < 0 \mu\text{m}$ – NCs implanted region; $x > 0 \mu\text{m}$ – pure fused silica margin. Solid dots (circles) correspond the sample annealed in Ar (Ar + 4% H₂). Inset: single beam transmitted SHG configuration.

was annealed in an Ar/H₂ mixture. The unimplanted glass yielded a barely detectable background SHG signal. For both samples, the SHG signal rose immediately as the scanning excitation beam crossed into the implanted region, clearly demonstrating that the signal was caused by the Si NCs. Remarkably, the signal from Ar-annealed NCs was ten times stronger, i.e. annealing in H₂ quenched SHG relative to Ar-annealed samples. This result shows the SHG from Si nanocrystals is sensitive to the nano-interface chemistry.

Since the interior of individual Si NCs is centrosymmetric, the second-

order nonlinear susceptibility $\chi^{(2)}$ vanishes in the electric-dipole approximation. Thus the interior of a NC can contribute only quadrupolar SHG [14, 20, 31]. Nevertheless, centrosymmetry is broken locally at the Si/SiO₂ interface. The resulting local interface dipole creates a nonzero SHG polarization even upon spherical averaging. Such an interface polarization is evidently the dominant microscopic source of SHG from the Ar-annealed samples, in view of the sensitivity of SHG to H passivation of the Si/SiO₂ interface.

3.3.2 Sensitivity to nanocrystal density gradients

The presence of fluctuations in particle shape, size, or density can also contribute a nonzero SHG polarization in general remains on macroscopic bulk average. We observed strong enhancements of the basic SHG signal described above when explicit macroscopic centrosymmetry-breaking features were present in the sample. As one example of this, Figure 3.4 shows fine detail of one SHG scan across the boundary between implanted and unimplanted substrate for the Ar-annealed sample, with fundamental p-polarized with respect to the boundary and all SH polarizations detected. A further tenfold enhancement of SHG is evident in many locations in the immediate boundary region. Polarization analysis of the SH signals shows that these local enhancements are contained almost entirely in the p-out component.

The p-in, p-out configuration is most sensitive to breaking of centrosymmetry by local particle density gradients perpendicular to the boundary. We therefore attribute the SHG boundary enhancements to these gradients.

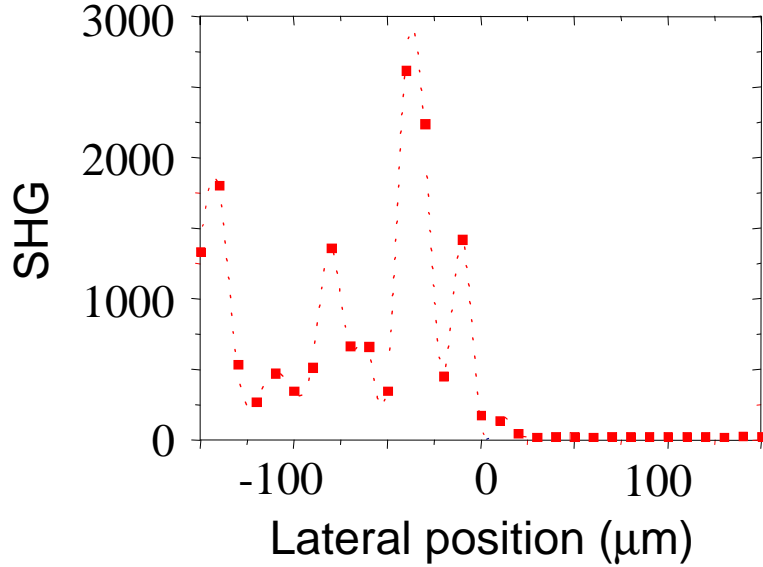


Figure 3.4: Small step lateral scan on the boundary between pure glass and nanocrystal-embedded glass shows SHG sharply increasing at some points.

3.3.3 SHG Radiation pattern

We imaged the incident fundamental mode and the SHG mode from Si NCs implanted in glass into a CCD camera using a $10\times$ microscope objective lens. The setup for imaging the SHG mode is shown in Figure 3.5. The fundamental mode image (Figure 3.5, upper right) shows a Gaussian distribution, while the SHG mode image shows a node through the center of the 2ω beam profile (Figure 3.5, lower right). This mode is consistent with SH field distribution $\mathbf{E}^{2\omega} \sim (\mathbf{E}^\omega \cdot \nabla)\mathbf{E}^\omega$, where \mathbf{E}^ω denotes the fundamental Gaussian field. This unique SHG mode image proves the essential conclusion of single-particle theories [14, 20, 31], i.e., quadrupole polarization is generated from spherically-averaged surface dipole polarization: $\mathbf{P}^{(2)} \sim (\mathbf{E} \cdot \nabla)\mathbf{E}$. In the cen-

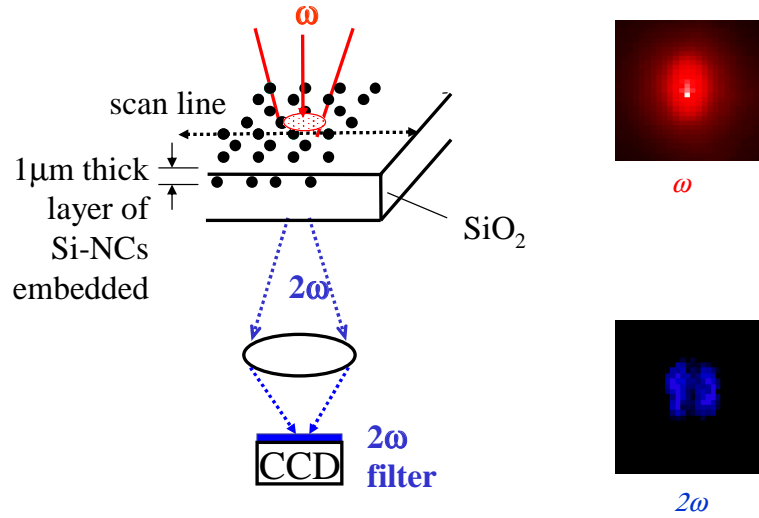


Figure 3.5: The SHG radiation pattern measured by a CCD camera has a TEM_{01} mode (double lobes, lower right) when the incident fundamental beam has TEM_{00} mode (upper right). The experimental setup for imaging the SHG mode is shown in the main panel of the figure.

ter of a Gaussian laser focus profile, $\mathbf{E} \cdot \nabla \mathbf{E} = 0$, so that no SHG is generated. SHG is distributed at the sides of beam profile where $\mathbf{E} \cdot \nabla \mathbf{E} = 0$ is nonzero (see Figure 3.6). The shape of the quadrupole polarization is consistent with the SHG mode image.

3.4 Two-beam SHG

Single beam SHG from Si nanocrystals has been demonstrated to be sensitive to surface chemistry and NC density in the last section. However, the SHG signal is very weak (a few hundred counts per second) due to its quadrupolar nature. The weak signal prevented us from doing extensive spec-

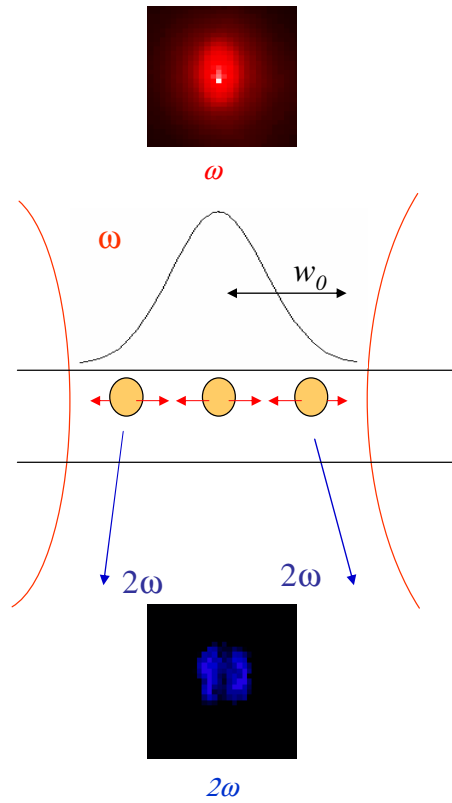


Figure 3.6: The gradient of the fundamental electric field vanishes in the center of a Gaussian beam, so does the SH field.

troscopic and fs-time-resolved studies of the nano-interface properties of Si NCs. In this section, we formulate the theory of quadrupolar SHG, then investigate the possibility to enhance quadrupolar SHG from NCs using two laser beams. The experimental realization is then presented in the following sub-sections.

3.4.1 Two-beam SHG Theory

Recent phenomenological models of SHG from individual spherical particles of centrosymmetric material [14, 20] and from nanocomposites [31] have shown that the lowest order contributions to the SH polarization density $\mathbf{P}^{(2)}$ are [31]

$$\mathbf{P}_Q^{(2)} = n_{NC}\mathbf{p}^{(2)} - \frac{1}{6}\nabla \cdot n_{NC}\tilde{Q}^{(2)}. \quad (3.1)$$

The first term represents the contribution from the SH dipole moments $\mathbf{p}^{(2)}$ of individual nanoparticles of uniform density n_{NC} . $\mathbf{p}^{(2)}$ has a nonlocal form, with its radiative part proportional to $(\mathbf{E} \cdot \nabla)\mathbf{E}$, that results from spherically averaging the locally noncentrosymmetric dipole polarization of the Si/SiO₂ interface, with additional contributions from the bulk Si. The second term describes additional contributions from the SH quadrupole moment tensor $\tilde{Q}^{(2)}$, which enhance SHG in regions of local gradients ∇n_{NC} in NC density [31].

In the two-beam geometry (see Figure 3.7), approximating incident fields \mathbf{E}_1 and \mathbf{E}_2 as plane waves, the SH polarization of Si NC composites

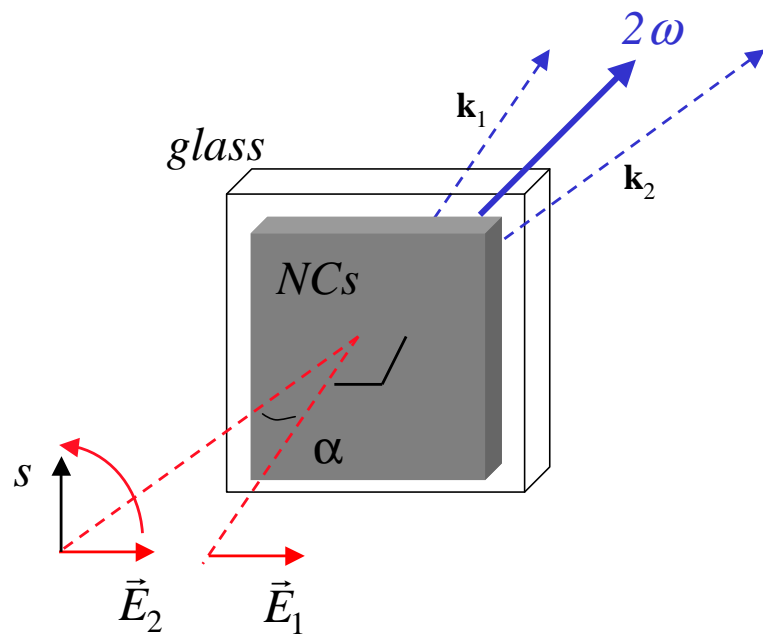


Figure 3.7: Two laser beams are used to excite quadrupolar SHG from centrosymmetric materials.

becomes

$$\begin{aligned} \mathbf{P}_Q^{(2)} = & in_{NC}(\delta - \beta - 2\gamma)\{\mathbf{E}_1^0 \cdot \mathbf{k}_1 \mathbf{E}_1^0 \exp(2i\mathbf{k}_1 \cdot \mathbf{r}) + \mathbf{E}_1^0 \cdot \mathbf{k}_2 \mathbf{E}_2^0 \exp[i(\mathbf{k}_1 + \mathbf{k}_2) \cdot \mathbf{r}] \\ & + \mathbf{E}_2^0 \cdot \mathbf{k}_1 \mathbf{E}_1^0 \exp[i(\mathbf{k}_1 + \mathbf{k}_2) \cdot \mathbf{r}] + \mathbf{E}_2^0 \cdot \mathbf{k}_2 \mathbf{E}_2^0 \exp(2i\mathbf{k}_2 \cdot \mathbf{r})\}, \quad (3.2) \end{aligned}$$

The mathematical description of the enhancement mechanism using two-beam geometry has been shown in Section 2.2. The enhancement mechanism also applies on silicon nano-composites, which are macroscopically centrosymmetric.

3.4.2 Enhanced SHG from Si NC sample

The experimental setup is the same as in Section 2.3. The amplified Ti:Sapphire laser beam was loosely focused ($w_1 = w_2 = 500 \mu\text{m}$), 50/50 split into two beams and then overlapped spatially and temporally on the Si NC embedded glass. The 2-beam SHG in the bisecting direction of the two fundamental beams was detected by the PMT when the polarization of beam 1 was rotated from horizontal to vertical (Figure 3.8 right). The 2-beam SHG increased from the minimum to the maximum as the two beams changed from co-polarization to orthogonal-polarization (see Figure 3.8 left). This result agrees very well with the theory in the last section .

Two-beam SHG of Si NCs, like its single beam counterpart, is sensitive to interface chemistry . When samples annealed in Ar and Ar + 4% H₂ were scanned, 2-beam SHG was again much stronger than from the Ar-annealed sample (see Figure 3.9). In addition, the 2-beam SHG emerged in

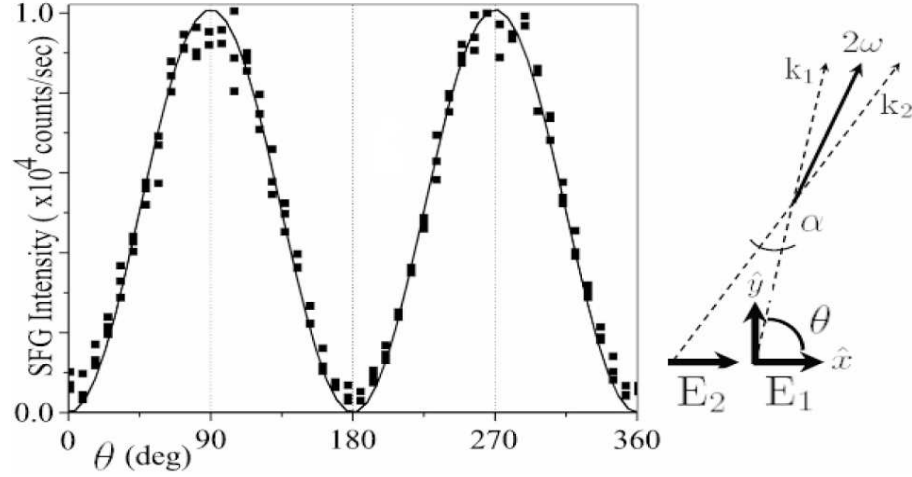


Figure 3.8: The 2-beam SHG intensity depends on the angle between the polarization of E_1 and E_2 . The intensity maximized when $E_1 \perp E_2$.

an S-polarized TEM_{00} mode (Figure 3.10), in agreement with the quadrupolar model.

We often observe strong fluctuations in two-beam SHG intensity when the laser beams scans across the border between NC implanted and unimplanted glass, as shown in the $x \approx 0$ region in Figure 3.9. These fluctuations are believed to originate from local gradients ∇n_{NC} in NC density. In non-uniform nano-composites, such gradients also contribute to the SH polarization [23, 31, 36] (see Equation 3.1). The first term in Equation 3.1 is equivalent to Equation (3.2), and describes the contribution of individual NCs of uniform density n_{NC} ; the second term is proportional to the SH quadrupole moment, and interferes with SH fields from the first term in regions of local gradients in NC density, leading to fluctuations in SHG intensity.

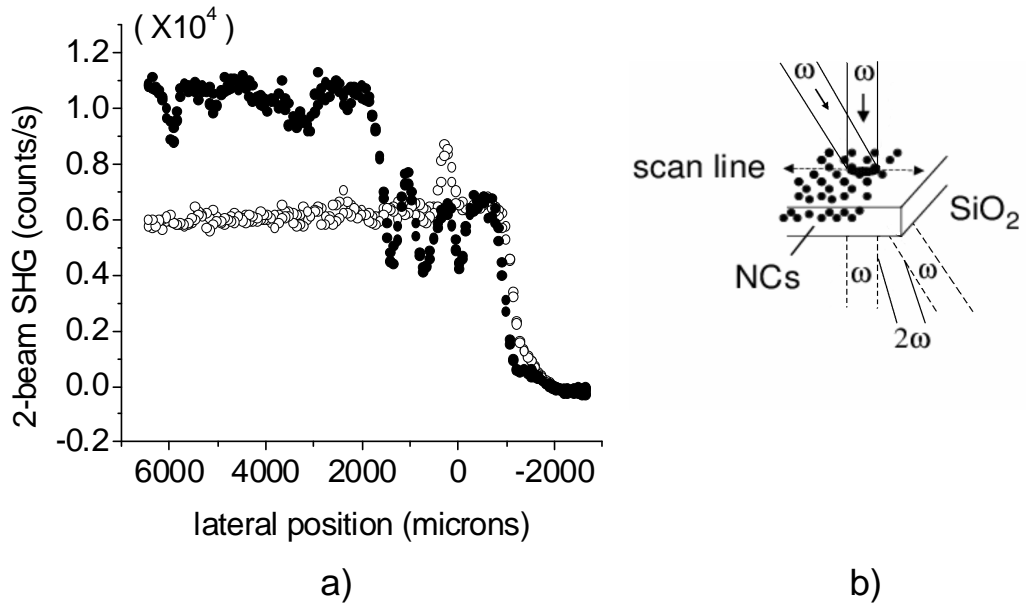


Figure 3.9: (a) Scan of two-beam SHG across the boundary between Si NC implant and unimplanted glass rim at edge of sample. $x > 0 \mu\text{m}$ – NCs implanted region; $0 > x > -1000 \mu\text{m}$ – pure fused silica margin; $x < -1000 \mu\text{m}$ – air. Solid dots (circles) correspond the sample annealed in Ar (Ar + 4% H₂). (b) Transmission two-beam SHG geometry.

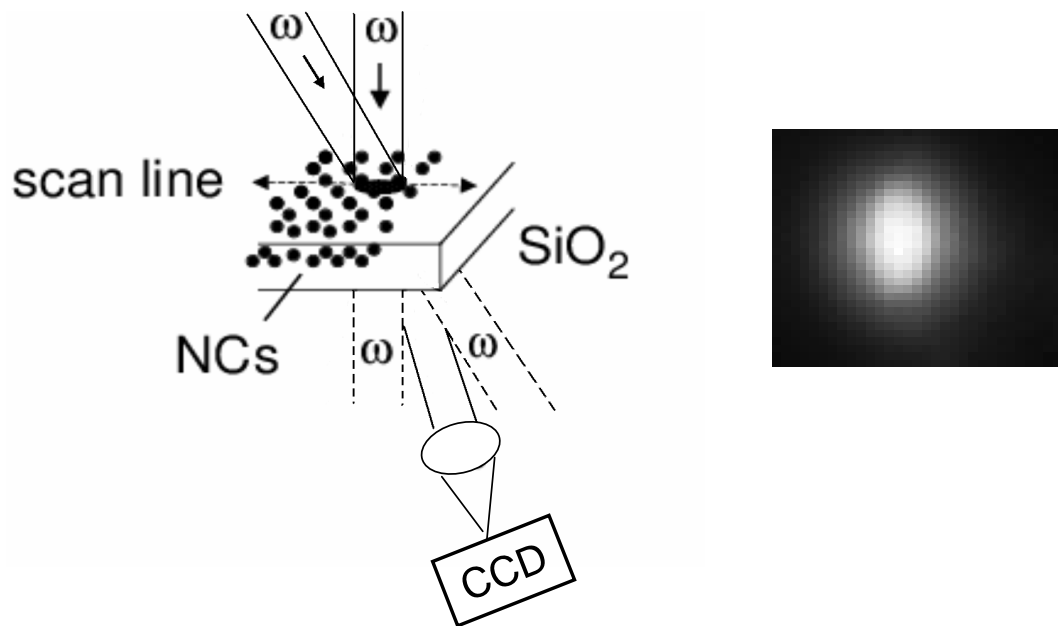


Figure 3.10: The spatial profile of the 2-beam SHG from Si NC embedded region appears in a TEM_{00} mode.

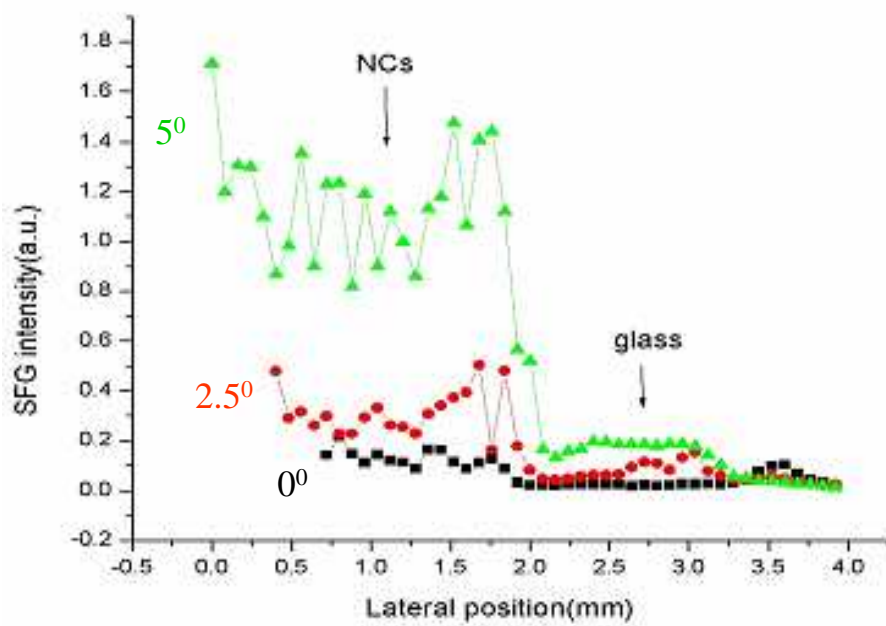


Figure 3.11: Transmitted 2-beam SHG (labeled as SFG in the figure) scan across the boundary (2.2mm) between 5 nm Si NCs and unimplanted glass on the samples annealed for 1 hour at 1100°C in pure Ar. Both of the incident beams are P polarized according to the sample.

The effect of the density gradient of nanocrystals on the SHG can be easily investigated when we set both beams polarized in the horizontal plan, in which case the first term in Equation 3.1 almost vanishes. Figure 3.11 shows SHG for p-polarized incident beams as incident angle increases from 0° (equivalent to the signals in Figure 3.3) to 5° . The increasing SHG signal from Si NC region results from the increasing incident field component along the gradient at the buried Si NC composite/glass interface, as shown in Figure 3.12.

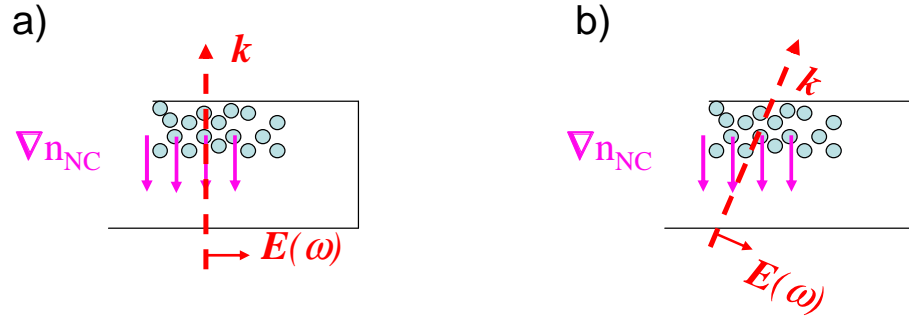


Figure 3.12: a) The incident beam electric field has no component along the gradient at the the Si NCs composite/glass interface. b) The incident beam electric field component along the gradient at the the Si NCs composite/glass interface increases when the sample is tilted.

3.4.3 SHG signal discrimination

However, the SHG from glass substrate was also enhanced, which is shown in Figure 3.9 ($0 > x > -1000 \mu\text{m}$ region), when we laterally scan the laser beams from the nanocrystal embedded region to pure glass margin on the sample. This is because glass is isotropic material and the same enhancement mechanism applied to it. So the SHG from the nanocrystal embedded region is actually a mixture of SHG from nanocrystal composite and glass substrate. The magnitude of the SHG from nanocrystals has the same order as the SHG from glass.

To verify those two contributions, we flipped the sample and did two lateral scans on the sample when the silicon nanocrystal layer was on the laser beam exit side and on the laser beam entrance side. Since the nanocrystal layer absorbs a certain amount of SHG light while is almost transparent to the

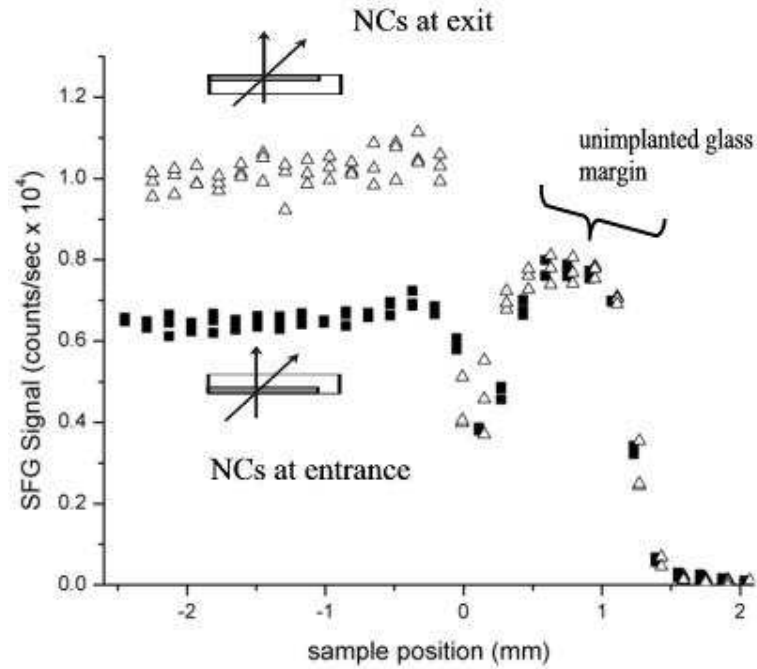


Figure 3.13: Scan of two-beam SHG across the glass-NC boundary with a NC layer ($\langle d_{NC} \rangle = 5\text{nm}$) at entrance (filled squares) or exit (triangles) side of sample, with orthogonally polarized incident fields.

fundamental light, the order of the nanocrystal layer relative to the glass substrate will make difference on the total (mixture) signal. When the nanocrystal layer is on the entrance side, it does not absorb the SHG from glass since it is generated later. However, if the nanocrystal layer is on the exit side, part of the SHG from glass will be absorbed. The SHG from nanocrystals is same in those two cases. It destructively interferences with the glass SHG. So in the case that glass SHG is absorbed (NC at exit), the total SHG is lager. The experimental result shown in figure 3.13 agrees well with the prediction.

The Si NC SHG signal can also be well discriminated in the spectral domain. The thickness of the glass substrate is about 900 μm . It is much larger than the coherence length ($\sim 10 \mu\text{m}$) of the SHG propagating in the glass. Since the fundamental laser pulse has a bandwidth of 12 nm, the phase mismatch Δk is different for different wavelength components. When each frequency component passes through the same thickness of material, the corresponding SH generated is also different. In the spectrum of SHG, we can observe “Maker” fringes. (Original Maker fringes [30] were produced when the laser beam passed through a variable thickness of crystal, and SHG intensity oscillated when the thickness increased. Here the sample thickness is fixed, but we have different wavelength components in each laser pulse.) As shown in Figure 3.14, the SHG from pure glass has four fringes when it is dispersed in a spectrometer. On the other hand, the thickness of the silicon nanocrystal layer is only 1 μm thick, much less than the coherence length. That means phase mismatch inside the nanocrystal layer is negligible so no spectral fringes are imposed as a result of SHG from nanocrystals. However, that SHG coherently superimposes on the SHG from the glass substrate, and shifts the fringes in the spectrum, as shown in figure 3.14.

The SH field from pure glass margin is [37]

$$\mathbf{E}_g^{2\omega} = \Gamma_g(\Delta k)^{-1} \mathbf{E}^2(\omega)(e^{i\Delta k_g L_g} - 1), \quad (3.3)$$

where Γ_g is the overall scaling factor, Δk_g is the phase mismatch in \hat{z} inside the sample, and L_g is the thickness of the glass. When it pass through an

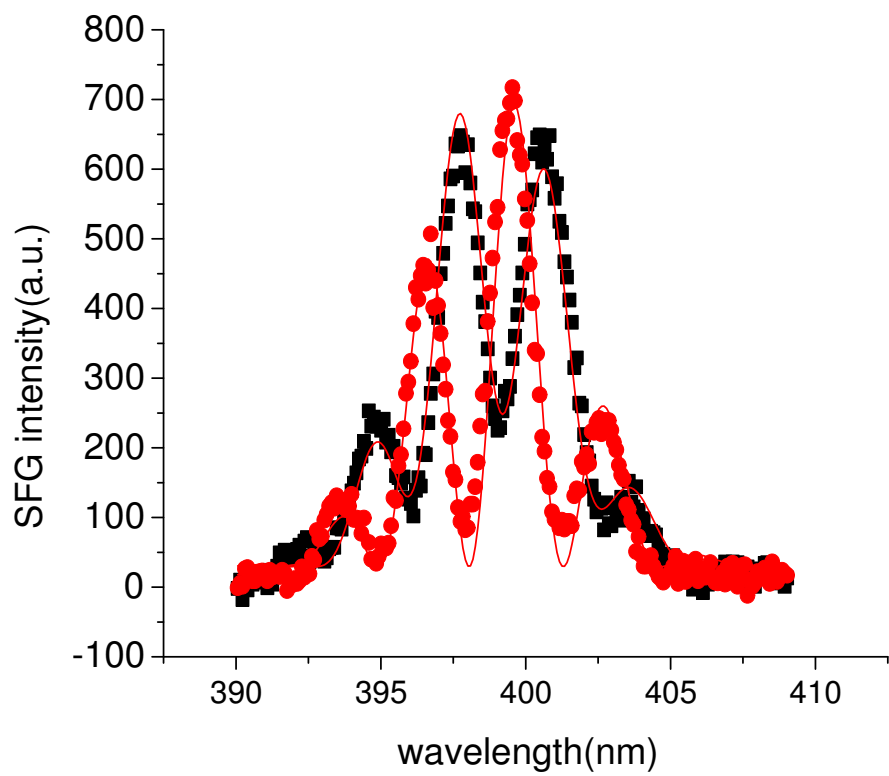


Figure 3.14: Frequency dispersed SHGs from pure glass (solid circles) and nanocrystal embedded glass (solid squares) show “Maker” fringes due to the frequency dependent phase mismatch. The solid lines are fitting curves.

embedded silicon nanocrystal layer (as in the case the nanocrystal layer in on the exit side), the absorption of the SHG has to be taken into account. Then the SH field from glass behind the nanocrystal implant is,

$$\mathbf{E}_g^{2\omega} = \Gamma_g(\Delta k)^{-1}\mathbf{E}^2(\omega)e^{(-\alpha_{NC}^{2\omega}+i\Delta k)L_{NC}}(e^{i\Delta k L_g} - 1), \quad (3.4)$$

where $\alpha_{NC}^{2\omega}$ and L_{NC} are the linear absorption coefficient and thickness of the NC layer, respectively. The SH field from silicon nanocrystals is

$$\mathbf{E}_{NC}^{2\omega} = i\Gamma_{NC}(i\Delta k + \alpha_{NC}^{2\omega})^{-1}\mathbf{E}^2(\omega)(e^{i\Delta k L_{NC}} - e^{-\alpha L_{NC}}). \quad (3.5)$$

So the total SH field from the nanocrystal embedded region is $\mathbf{E}_{NC}^{2\omega} + \mathbf{E}_g^{2\omega}$. The total SHG intensity is then $|\mathbf{E}_{NC}^{2\omega} + \mathbf{E}_g^{2\omega}|^2$. We use this model to fit the data shown in Figure 3.14, by setting the fitting value $\Gamma_{NC}/\Gamma_g = P_1 e^{iP_2}$. Fitting curves are also shown in Figure 3.14. We obtain $P_1 = 1.35 \pm 0.01$ and $P_2 = 0.39\pi \pm 0.002\pi$. The presence of a significant positive phase shift of Γ_{NC} relative to Γ_g suggest that 2ω lies just below a resonance of the Si NCs.

For contrast, the spectra of the SH generated by two co-polarized beam are shown in Figure 3.15. The SHG from glass is extremely weak. The SHG from NCs embedded region is a little stronger than from glass. Since the thickness of the NC layer is much less than the coherence length, the spectrum doesn't show "Maker" fringes, as expected.

Perhaps the best method of signal discrimination exploits the fact that the two-beam bulk-quadrupolar SHG vanishes as long as the beam overlap region is totally immersed inside the isotropic bulk substrate, which makes

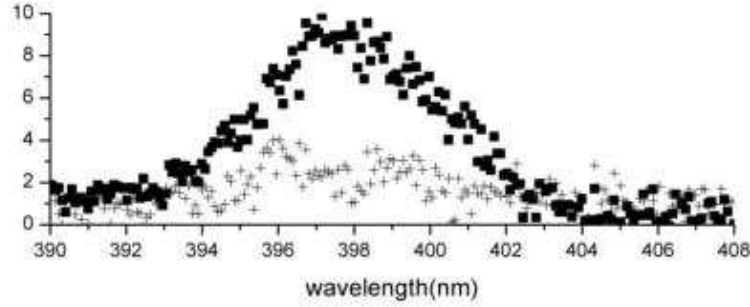


Figure 3.15: Frequency dispersed SHGs from pure glass (solid circles) and nanocrystal embedded glass (solid squares) when the two beams are co-polarized don't show "Maker" fringes.

the quadrupolar SHG surface-like [17, 18, 43] (see the details in Section 2.6). Moreover, if two isotropic materials have similar refractive indices and nonlinear susceptibilities, the two-beam SHG also vanishes on the interface between those two materials. We found that water and glass are such materials (see the details in Section 2.7). By stacking a pure glass slide on top of a NC-implanted slide (with its 1 μm -thick implant facing the gap), then filling the gap with water, we observed no SHG when the 2-beams overlapped the gap outside the NC implant (Figure 3.16, top) and pure SHG from NCs when they overlapped the implant (see Figure 3.16, bottom). In Figure 3.16 bottom, we can also see that the magnitude of the left peak (SHG from 1st surface) is only 1/3 of the right peak (SHG from 2nd surface). This is because that Si nanocrystal layer in the middle absorbs 2/3 of the SHG from glass on the left side but is transparent to the fundamental beams. This technique totally separates the SHG from the nanocrystal composites from their host glass, and still keeps

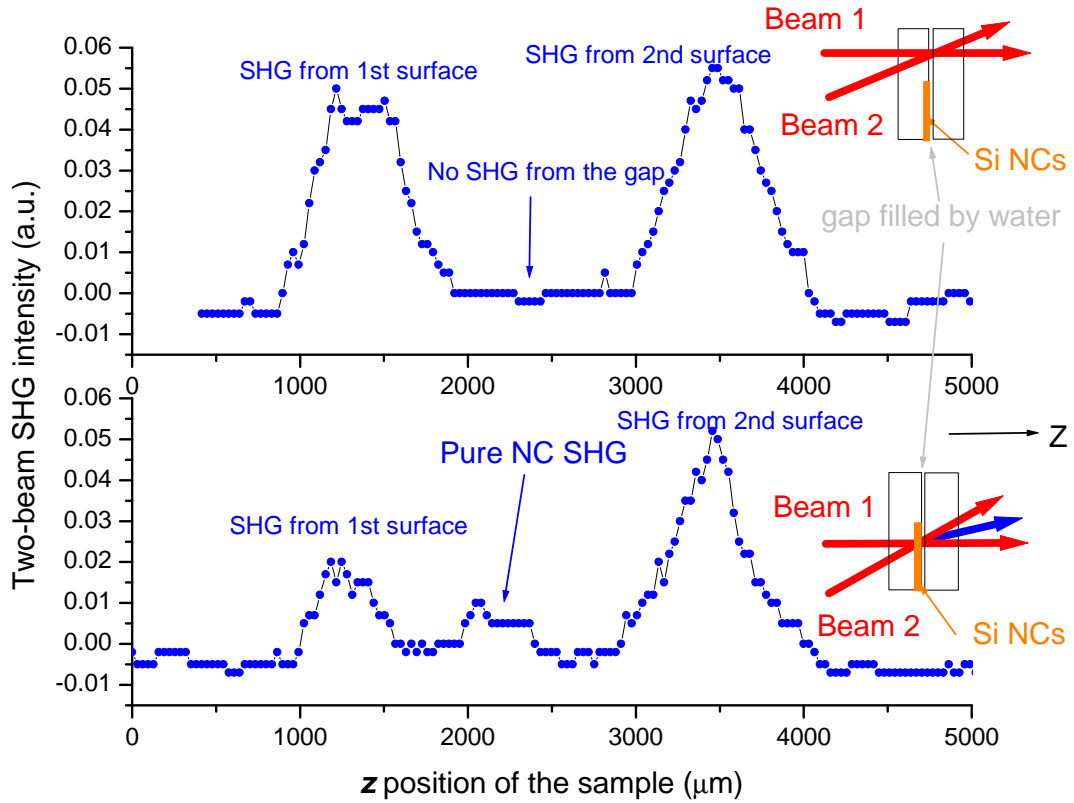


Figure 3.16: Two-beam SHG z -scan: a NC sample stacked with a same size fused silica slide with water filled in the gap. Top: z -scan in the pure fused silica margin; Bottom: z -scan in the NC implanted region.

the SHG enhanced. It can be applied to other nano-materials when we use 2-beam SHG to probe their interfaces.

3.5 Conclusion

We have experimentally verified that SHG from a uniform composite of spherical Si NCs is radiated by a nonlinear polarization of nonlocal dipolar

(quadrupolar) form proportional to $(\mathbf{E} \cdot \nabla)\mathbf{E}$. We showed that SH responses of this form are greatly enhanced in a noncollinear two-beam SHG configuration, whether they originate microscopically from spherical interfaces (as in the nanocomposite) or from a bulk quadrupolar response (as in the glass substrate). Competing signals from NCs and substrate were discriminated by several techniques. The enhanced SHG is useful for scanning, spectroscopy, real-time monitoring, and microscopy.

Chapter 4

Phase matched quadrupolar SHG from centrosymmetric materials

4.1 Introduction

Quadrupolar SH generated from the isotropic bulk is usually a weak undesired background signal that interferes with the study of interface dipolar SHG from the surface. As demonstrated in preceding chapters, this usually weak signal can be dramatically enhanced by two orthogonally polarized laser beams [23, 43]. The two-beam geometry can also be used to generate quasi-phase-matched (QPM) SHG from isotropic materials if proper periodicity can be realized.

The electric fields of phase mismatched and phase matched SHG are shown in Figure 4.1. Traditional QPM crystals (e.g. PPLN) for SHG were made by periodically reversing the sign of the second order polarization (as shown in Figure 4.1 (c)) to make the fundamental and second-harmonic (SH) wave travel in phase in the crystal [22]. In the two-beam geometry, the fundamental and the SH wave do not propagate in the same direction, causing additional phase delay between the SH wave and the fundamental wave [23, 43] (see Figure 4.2 (b)). This feature can be used to build a QPM crystal with

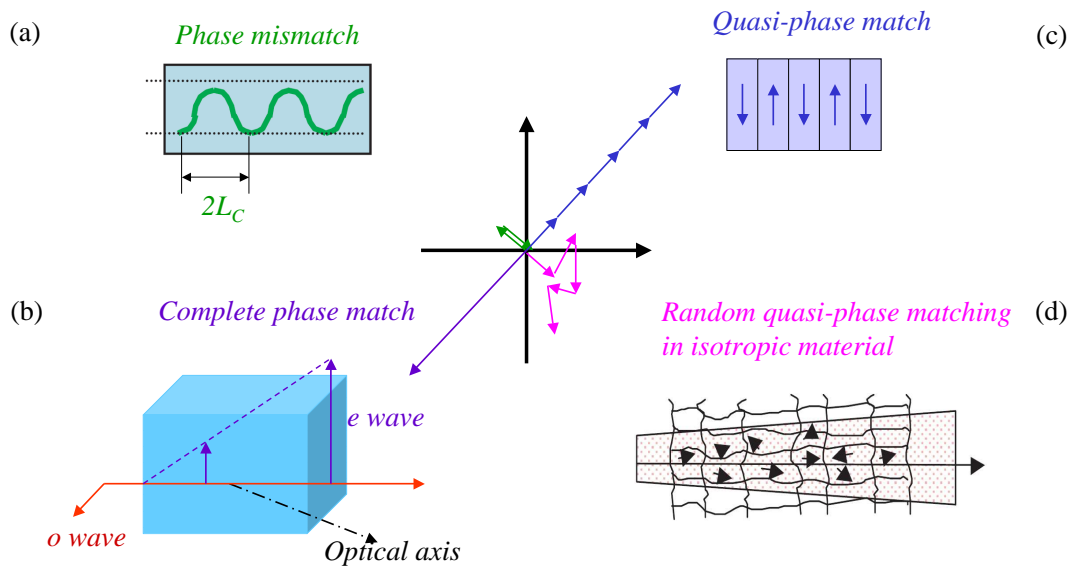


Figure 4.1: The diagram in the center shows the growth of SH electric field in a complex coordinate. (a) If there is phase mismatch between the SH polarization wave and the SH radiation wave, the SHG oscillates along the beam propagation direction inside the crystal. (b) The SH field grows linearly along the beam propagation direction when the phase match between the SH e-wave and the fundamental o-wave is realized. (c) Quasi-Phase-Match can be realized when the SH polarization can be periodically reversed in the beam propagation direction. (d) In a polycrystalline structure, superimposition of the SH generated from each domain which has different phase in the beam propagation direction can yield net increase of the total SH [4].

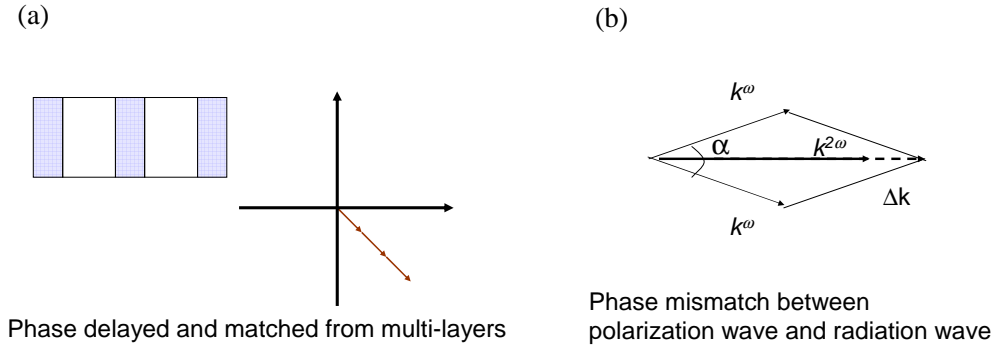


Figure 4.2: (a) A structure designed to realize Quasi-Phase-Matched 2-beam SHG using isotropic material (e.g. glass). Left: the grey region is the active material, the white region is nonactive material which delays the phase of SH polarization wave relative to SH radiation wave. Right: growth of SH electric field when the fundamental two beams propagate through the material. (b) Phase mismatch between the SH polarization wave and SH radiation wave.

isotropic materials, without periodically reversing the sign of the nonlinear polarization (see Figure 4.2 (a)). For example, we can make an array of thin glass films, each with thickness equal to the coherence length of quadrupolar SHG in glass, separated by twice this coherence length. The spacing material does not generate SH, but delays the phase between the SH and the fundamental wave. As a result, quadrupolar SHG from each film superposes constructively, and total SHG continuously grows along the film array. In Figure 4.3, we compare the SHG intensity growth with the thickness of the sample for different phase matching schemes. Two-beam quasi-phase-matched SHG grows slower than that of single beam since there are inactive materials in between the active materials, but its overall growth is parabolical.

In this chapter, we investigate the possibility of phase matching quadrupo-

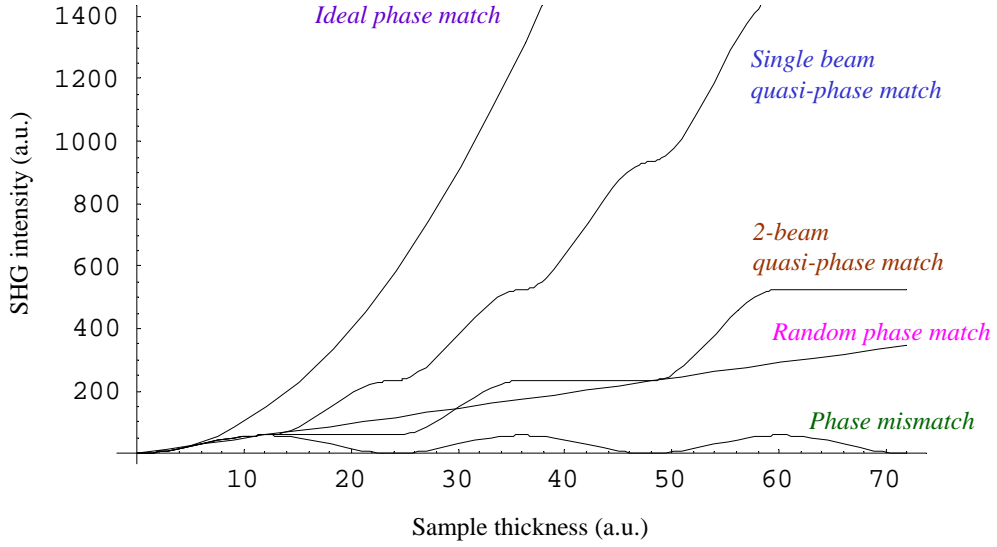


Figure 4.3: Comparison of calculated SHG growth in different schemes.

lar SHG from two kinds of centrosymmetric materials. In section 4.2 and section 4.3, we show quasi-phase-matched SHG from two glass slides and two pellicle thin films respectively.

4.2 Quasi-Phase-Matched SHG from glass slides

As a proof of principle, we prepared samples with just two QPM periods by stacking two glass cover slides (thickness around $150 \mu\text{m}$) together. The laser output (810 nm , 100 fs , $1 \mu\text{J}/\text{pulse}$) is split 50/50 into one beam that is normally incident onto the sample, and a second beam incident at 20° from the surface normal. The normally (obliquely) incident beam is focused by a lens to a spot size of $w_0 \sim 20 \mu\text{m}$ ($w_0 \sim 10 \mu\text{m}$), where w_0 is the beam waist. As a result, the two-beam overlap region has length $250 \mu\text{m}$, which sets the

maximum useful length of a QPM array. In Section 2.6, we showed that if the size of the two-beam overlap is smaller than the thickness of a bulk material, the bulk quadrupolar SHG appears surface-like [43], i.e., the signal peaked when the material surface centered in the two-beam overlap region, while the SHG from the center of the bulk vanished [43, 44](see section 2.6 for details). Here, we simulate the coherent superposition of two SH wave generated from two glass slides, shown in Figure 4.4. If there is no gap between the two glass slides (ideal case), then the two glass slides are just like one bulk, there is no SHG from the middle of the two glass slides except from the two outer surfaces (see Figure 4.4 upper left). After the two glass slides are separated by a gap of $5 \mu\text{m}$ wide, three approximately equal peaks appear (see Figure 4.4 middle left). This was also observed in our previous experiments (see Figure 2.11 in Chapter 2). At this time, the gap is not optimized for superposition of two SH waves. When the gap is about $13 \mu\text{m}$ (the coherence length of two-beam SHG in air), the two SHG wave are completely constructively superimposed, so that the total signal increases by four times (see Figure 4.4 lower left), which was also observed in the experiment shown in Figure 4.5 (a). When gap size increases more, the total SHG signal from the gap region oscillates several times (one is shown in Figure 4.4 upper right) until the gap exceeds length of two-beam overlap, which can be observed by the splitting of the middle peak, as shown in Figure 4.4 middle left (splitting) and Figure 4.4 lower left (split). In the experiment, we also observed 4 totally separated peaks (shown in Figure 4.5 (b)), just as simulated.

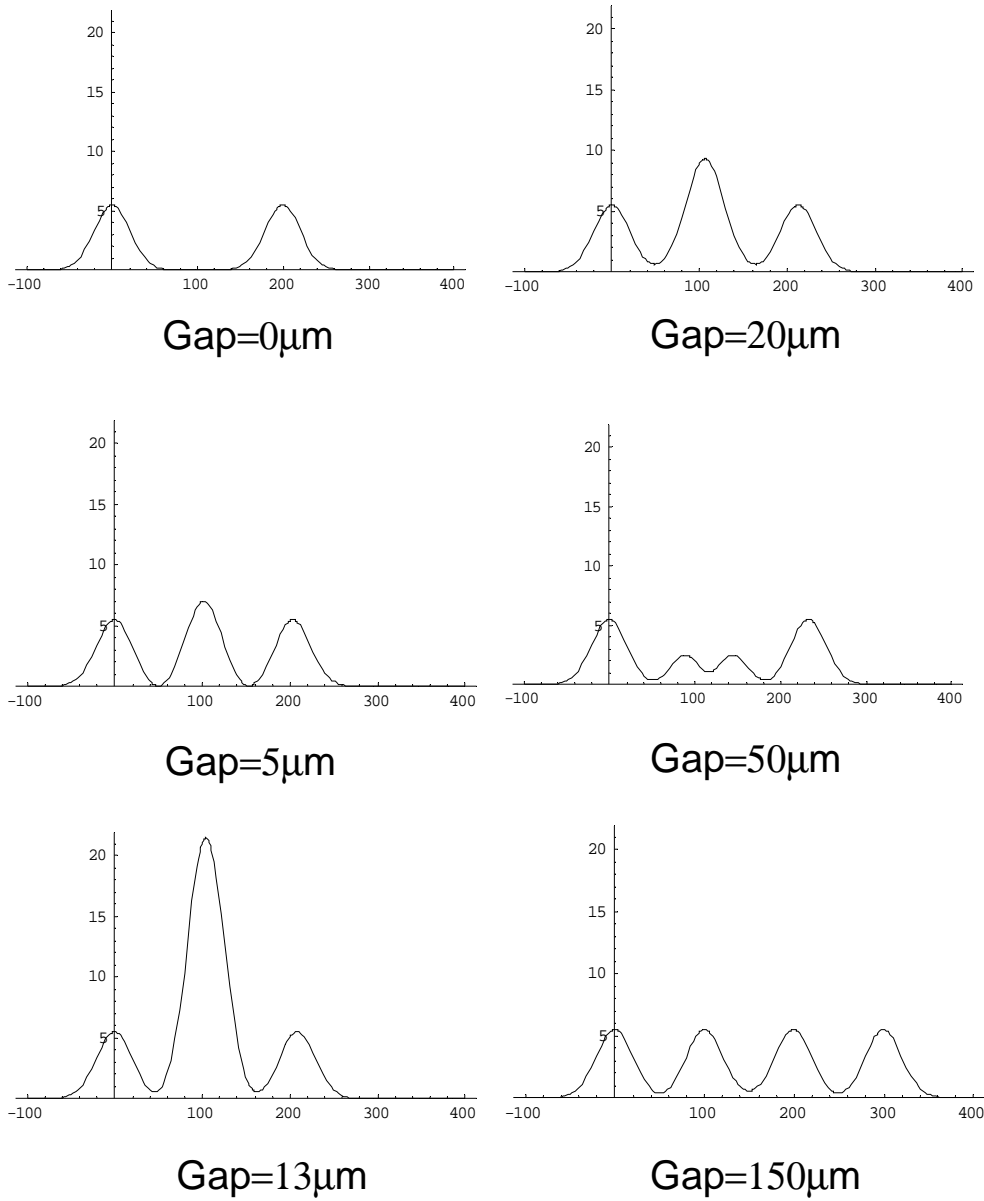


Figure 4.4: Simulation of the z-scan of the two-beam overlap across the two stacked glass slides separated by an air gap of different sizes. The horizontal axes represent the longitudinal position (\hat{z}) in μm , and the vertical axes represent the SHG intensity.

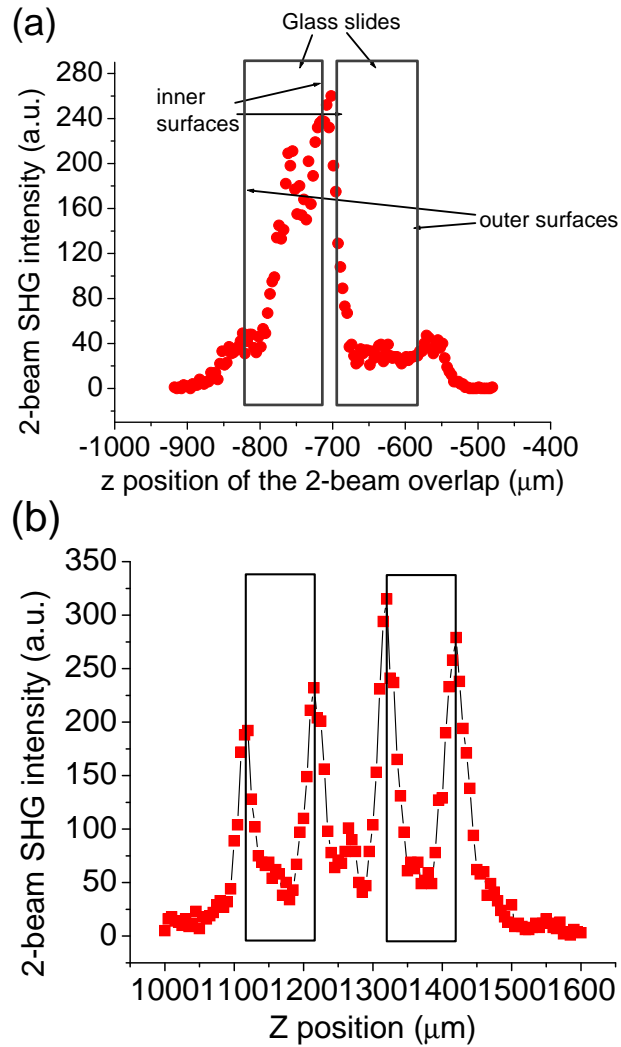


Figure 4.5: z-scan of the two-beam overlap across two stacked glass slides with a gap in between. (a) Gap size is about one coherence length ($13 \mu\text{m}$). (b) Gap size is larger than the two-beam overlap length.

To characterize the SHG superposition as a function of continuously varied phase delay between the fundamental and the SH wave, we prepared a wedge sample . Two glass slides (1 mm thick each) were stacked, one side with a spacing about $150 \mu m$, the other side made contact (see Figure 4.6). We centered the two-beam overlap inside the gap, so that only the inner side of the each glass slide generated SHG. The two inner surfaces formed a spacing wedge. When we translated the sample laterally, the spacing between the two inner surface varied so that the phase delay between the fundamental and the SH wave varied. In the Figure 4.6, we can see that the SHG oscillates when the two-beam overlap scans the wedge sample from left to right. At large (small) lateral position, the spacing is small (large). When the spacing got larger, two-beam overlap region had less overlap with the glass so the total signal decreased. Each SHG peak from a single glass slide is about 1/4 of the largest peak in Figure 4.6, which indicates the interference between the two SH waves generated from the inner sides of the wedge. The wedge angle was measured with He-Ne laser. The calculated spacing variation from lateral position from maximum SHG to its neighbor minimum is about $26 \mu m$. The coherence length of the two-beam SHG in air is about $13 \mu m$. This indicates there is an additional phase shift. It probably comes from the phase shift of the SH generated from each glass slides due to the variation of the overlap between the two-beam overlap and the glass slides.

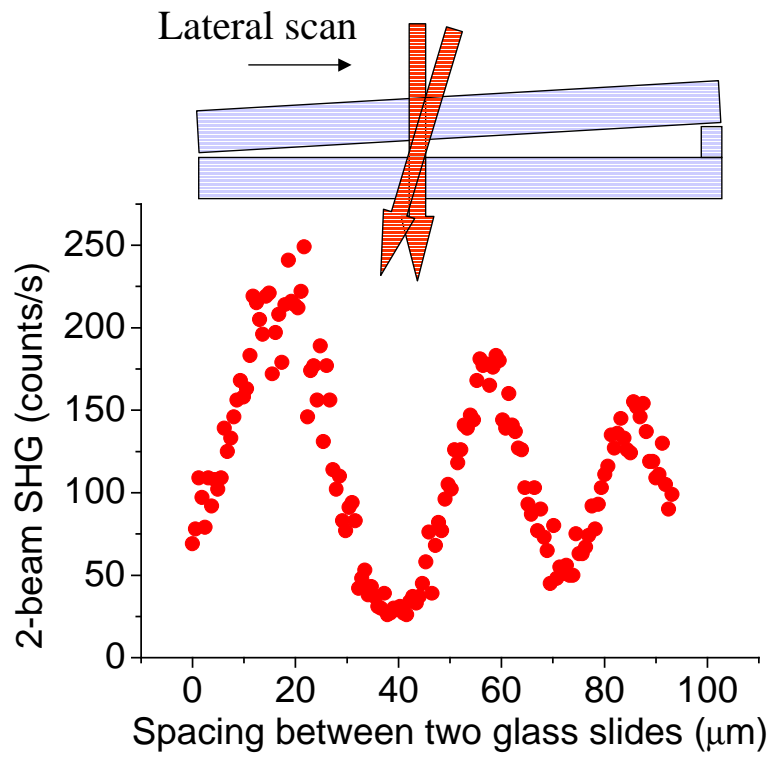


Figure 4.6: As the two-beam overlap scans laterally across the wedge sample, the SHG signal oscillates as the spacing between the two inner surfaces of the glass slides increases.

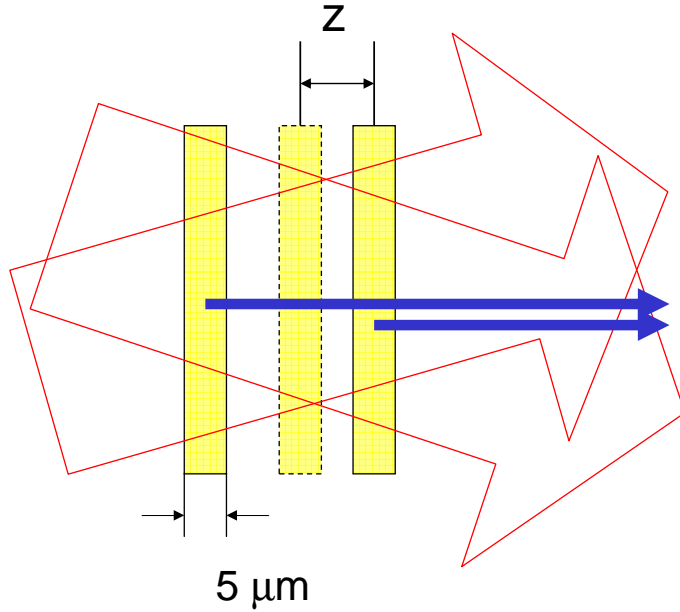


Figure 4.7: Two pellicle films (about $5 \mu\text{m}$ thick) are set parallel to each other and inside the two beams overlap region. The variation of the distance between the two films can change the phase difference between the two SH field generated from each film.

4.3 Quasi-Phase-Matched SHG from pellicle thin films

Since the thickness ($\sim 150 \mu\text{m}$) of the cover glass slides is comparable to the length ($\sim 250 \mu\text{m}$) of the two-beam overlap, the overlap between glass and the two-beam overlap also changes, which induces additional phase shift, as shown in the previous section. To overcome this difficulty, we choose pellicle thin films about $5 \mu\text{m}$ thick. This thickness is close but less than the coherence length of the 2-beam SHG in the film, but much less than the size of the two beam overlap (as shown in Figure 4.7). Then the shape of the two-beam overlap doesn't have significant effect on the SHG from the film during z-scan.

When the two pellicle films are close enough (\ll size of the two-beam overlap), the magnitude of the SH electric field is same, but their relative phase can be adjusted by changing the distance between the films. The total SHG electric field is then the superimposition of the electric field from each film. The measured SHG intensity depends on the distance as shown in Figure 4.7. The total SHG intensity is about 4 times the SHG intensity from each film when the SHG from each film is in phase; but vanishes when the SHG from each film is out of phase. From one SHG intensity peak to the next one, the distance between the two films changes about $28 \mu\text{m}$. This agrees with the model prediction ($2L_C^{air} = 2 \times 13 \mu\text{m} = 26 \mu\text{m}$) very well.

4.4 Phase-Matched SHG from calcite crystals

In the last section, we demonstrated SHG coherent superposition between just two thin films or two glass slides. Based on current technology, it is difficult to make a periodic structure with multi-layers satisfying the phase-matching condition discussed in the last sections. To bypass this difficulty, we choose a birefringent crystal – calcite – as our sample to demonstrate enhancing and phase-matching of quadrupolar SHG.

We mounted the calcite crystal sample (as shown in Figure 4.9) so that the o-axis of the crystal was always kept in $\hat{x} - \hat{z}$ plane while the sample was rotated around \hat{y} axis. By that manner, beam 1 (noted by \vec{E}_1) and beam 2 (noted by \vec{E}_2) kept their wave properties – o-wave or e-wave – during rotation, respectively. We kept beam 1 polarized in $\hat{x} - \hat{z}$ plane. When the

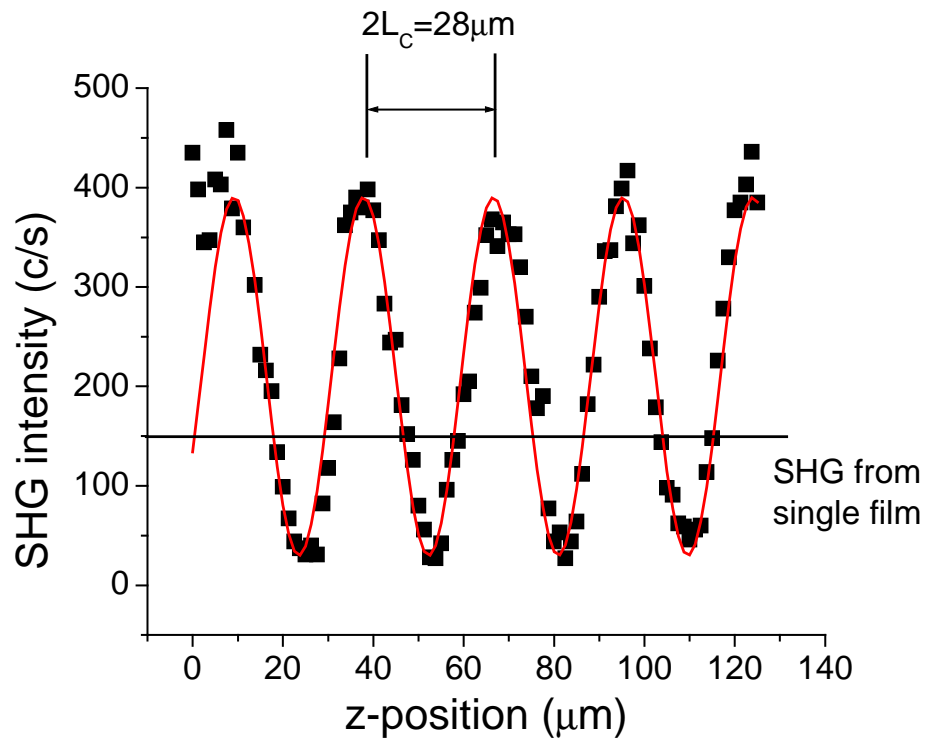


Figure 4.8: Experimental data (solid square) show the coherent superimposition of the two SH field generated from two pellicle films. The horizontal line shows the SHG intensity from a single pellicle film.

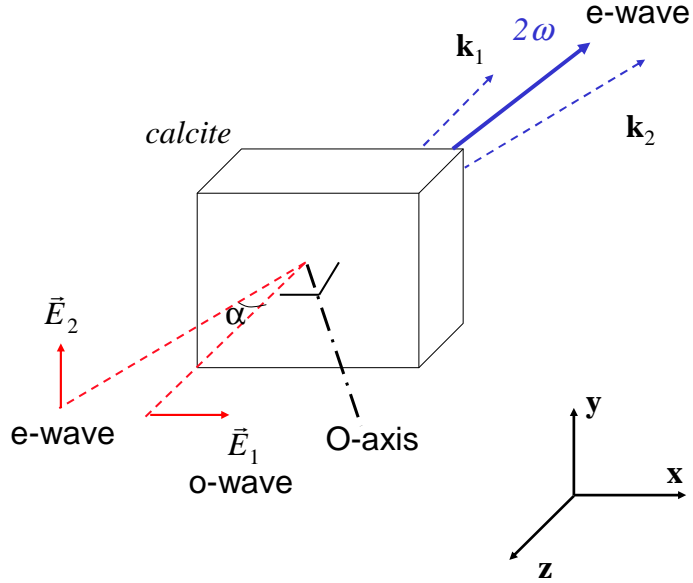


Figure 4.9: Scheme for phase-matched two-beam SHG from calcite crystal.

polarization of beam 2 was set in $\hat{x} - \hat{z}$ plane (\hat{y} direction), we rotated the sample around \hat{y} to find type I (type II) phase matching. Here, type I phase matching means two fundamental o-waves are mixed to generate SH e-wave, while type II phase matching means fundamental one o-waves and one e-wave are mixed to generate SH e-wave. We used beam 1 to do single-beam phase-matching experiments. In that case, we set beam 1 polarized 45° off the $\hat{x} - \hat{z}$ plane, which provided equal quantity of o-wave and e-wave simultaneously. We compared the two types of phase-matching with single- and two-beam using short and long laser pulses. All SHG signals were sensitive the crystal angle tuning, indicating the phase-matching of bulk SHG. The results are shown in Figure 4.1. All the type II phase-matched SHG is less than those of type I.

Here, group velocity walk-off has to be taken into account since we are using femto-second pulses and a birefringent crystal. In type II phase matching, group velocity of the fundamental e-wave ($v_g^{\omega,e} = 0.67c$ when the pulse central wavelength is 800nm, where c is the light speed in vacuum) is larger than o-wave ($v_g^{\omega,o} = 0.60c$). After the two waves propagate through 1 mm thick crystal, they separate about 520 fs, which is much larger than the pulse duration (~ 230 fs). In other word, o-wave and e-wave separate totally before they travel half of the sample. This doesn't happen in type I phase matching since both fundamental beams are o-waves. This is probably the reason why type I phase-matched SHG is larger than type II. When short pulses were used, both sing-beam and two-beam geometry gave almost the same amount of $I_{typeI}^{SHG}/I_{typeII}^{SHG}$ ratio (see Table 4.1). However, when longer pulses (~ 4000 fs) were used, the ratio when two-beam geometry (60) were used was less than single-beam geometry (28). In other word, two-beam geometry enhances the phase-matched SHG by a factor of 2 ($60/28 \sim 2$). If longer pulses are used, that factor can be improved.

4.5 Discussion

We have in principle demonstrated that quadrupolar SHG generated from isotropic materials (e.g. glass and pellicle) superposed coherently. This result shows it is promising to build build a QPM structure using inexpensive isotropic materials. But there are still several unsolved problems on the way to make such QPM “crystal”. For example, how to precisely position the layers?

		type I ($o + o \rightarrow e$)	type II ($o + e \rightarrow e$)	<u>type I</u> <u>type II</u>
short pulses (230 fs)	single beam	1	0.015	67
	two beams	0.061	9.8×10^{-4}	62
long pulses (4000 fs)	single beam	1	0.017	60
	two beams	1.3×10^{-4}	4.7×10^{-6}	28

Table 4.1: Comparison of type I and type II phase-matched SHG efficiencies in single-beam and two-beam geometries when short or long pulses are used.

How to reduce the reflection loss from each layer to improve the efficiency?
 In our experiments on pellicle thin films, the average reflection loss on each film is about 10%. After the fundamental beams pass through ten pellicle thin films, their intensity drop down to 35%, so the intensity of SHG from the eleventh film will drop down to $(35\%)^2 = 12\%$. Those reflection lose limits the SHG conversion efficiency and should be solved before practical applications. Using birefringent crystal to realize phase-matching doesn't have the reflection lose. However, there are also other limitations, for example, the group velocity walk-off problem will limit its application in ultra-short pulses.

Chapter 5

SHG *in situ* monitoring of CVD growth of nanocrystals

5.1 Introduction

As discussed in Chapter 2, optical second harmonic generation (SHG) is electric-dipole forbidden in bulk centrosymmetric media such as Si. However, the centrosymmetry of the bulk is broken when an electric field E^{DC} is applied to it, which locally enhances SHG in that region. As discussed below this electric-field-induced second-harmonic (EFISH) process is potentially useful for *in situ* monitoring of growth of nanocrystal layers for flash memory applications. In Si-NC-based flash memory devices, an NC layer embedded in the oxide traps and stores charge that has tunneled through the oxide layer separating it from the Si substrate [46]. Such a trapped charge layer creates an electric field that pervades the Si substrate, where EFISH generation can then take place. In preparation for this discussion, we first present a phenomenological description of EFISH generation.

EFISH is modeled in the dipole approximation by treating the applied electric field E^{DC} as an additional electric field contributing to the polarization density \mathbf{p}^{EFISH} , along with the incident laser field $\mathbf{E}(\omega)$. The applied field cou-

ples with the driving laser field through a third-order nonlinear susceptibility tensor [2]. The polarization density is

$$P_i^{EFISH}(2\omega, \mathbf{r}) = \chi_{ijkl}^{(3)}(2\omega) : E_j(\omega, \mathbf{r})E_k(\omega, \mathbf{r})E_l^{DC}(0, \mathbf{r}), \quad (5.1)$$

where the $E_j(\omega, \mathbf{r})E_k(\omega, \mathbf{r})$ are the components of the laser field, $E_l^{DC}(0)$ is the applied DC field, and $\chi^{(3)}$ is the fourth-rank susceptibility tensor.

In real measurements, the total SHG signal also includes contributions from surface dipole and bulk quadrupolar polarizations. The total quadratic polarization density is thus the sum of these three contributions:

$$\mathbf{P}^{(2)}(2\omega, \mathbf{r}) = \mathbf{P}^S(2\omega, \mathbf{r}) + \mathbf{P}^{BQ}(2\omega, \mathbf{r}) + \mathbf{P}^{EFISH}(2\omega, \mathbf{r}), \quad (5.2)$$

as illustrated in Figure 5.1.

The (SiO₂/Si(100)) sample is mounted on a rotational stage to observe the azimuthal angle dependence of SHG. In a field-free Si sample, the bulk SHG intensity is much lower than the surface SHG intensity (see Figure 5.2). If a DC electric field applied to the bulk silicon, EFISH from the bulk grows stronger relative to surface SHG (see Figure 5.3). The growth of EFISH in Figure 5.3 is caused by laser-induced accumulation of charges on the surface of the oxide cover layer. The charges are multi-photon excited by the laser from silicon substrate, then trapped on the SiO₂ surface. If the laser beam is blocked temporarily, the charge traps and EFISH decreases (see Figure 5.3). Thus the dynamics of EFISH reveals charge trapping and de-trapping dynamics on the sample surface. To be trapped, the electrons have to gain enough energy

by multi-photon excitation to overcome the potential barrier between the Si valence band and SiO₂ conduction band. Then the electrons diffuse to the SiO₂ surface. Since the scattering length of the electrons in SiO₂ is about 3.4 nm [7], the oxide need to be thin enough that the electrons can diffuse to the SiO₂ surface and be trapped there, or the electrons will return to the positively charged Si substrate. On the other hand, if the oxide is more than 10 nm thick, too few electrons diffuse to the SiO₂ surface, and time-dependent SHG (TDSHG) is negligible [7, 27].

Surface contaminants or surface and bulk defects in SiO₂ can serve as trap sites . Si NC grown on a Si/SiO₂ substrate can also serve as electron trap sites [46]. Because of Coulomb blockade, each nanocrystal can only trap one electron, so the density of the trapped electrons is proportional to the density of the nanocrystals. Since the density of the electrons can be probed by EFISH, the density of the NCs can also be probed. In this chapter, we investigate the possibility of using SHG to probe NC density noninvasively in a deposition chamber. Section 5.2 describes the experimental setup and procedure. In Section 5.3, we demonstrate that surface contaminants affect EFISH. In Section 5.4, we show experimental results of *in situ* SHG from Si NCs and discuss the results.

5.2 Experimental Setup

Experiments were performed in an ultra high vacuum chemical vapor deposition (UHV CVD) growth chamber (base pressure of 3×10^{10} Torr). Sam-

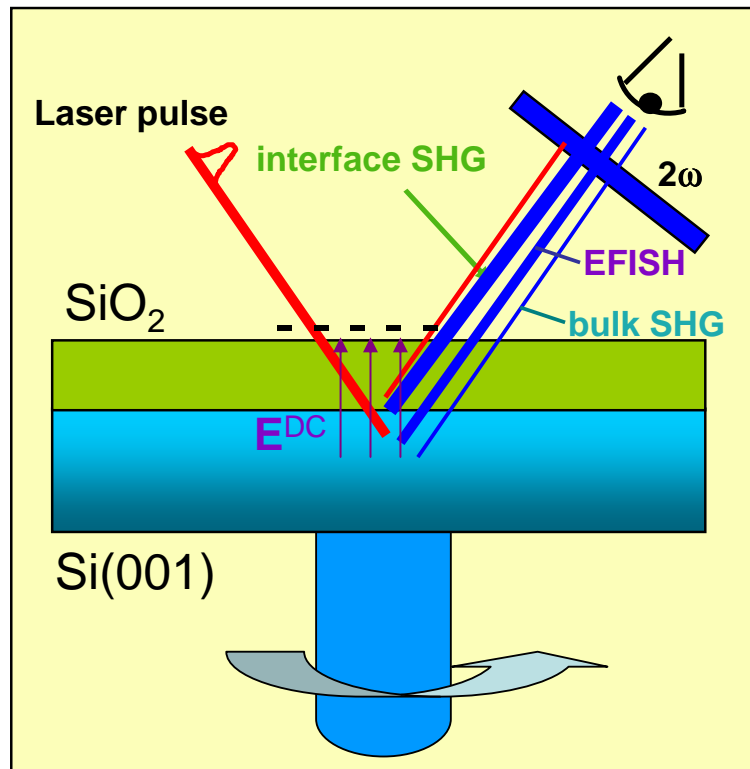


Figure 5.1: This cartoon shows all SHG sources from a Si sample: Si/SiO₂ interface SHG, Si bulk SHG and EFISH due to the DC electric field formed by charges trapped on the SiO₂ surface.

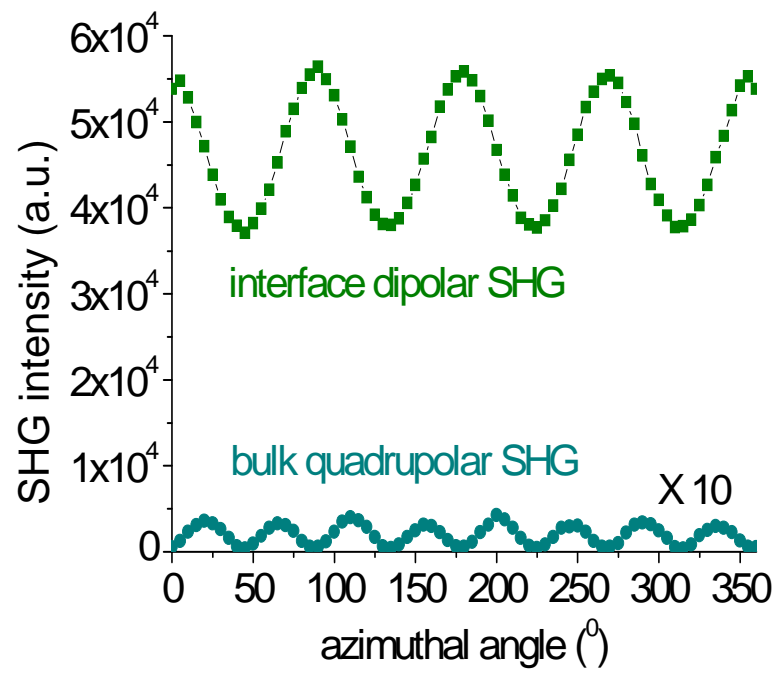


Figure 5.2: The intensity of the SHG from Si sample depends on the azimuthal angle. The bulk SHG has 8 fold symmetry. The bulk SHG intensity is 2 order lower than the surface SHG.

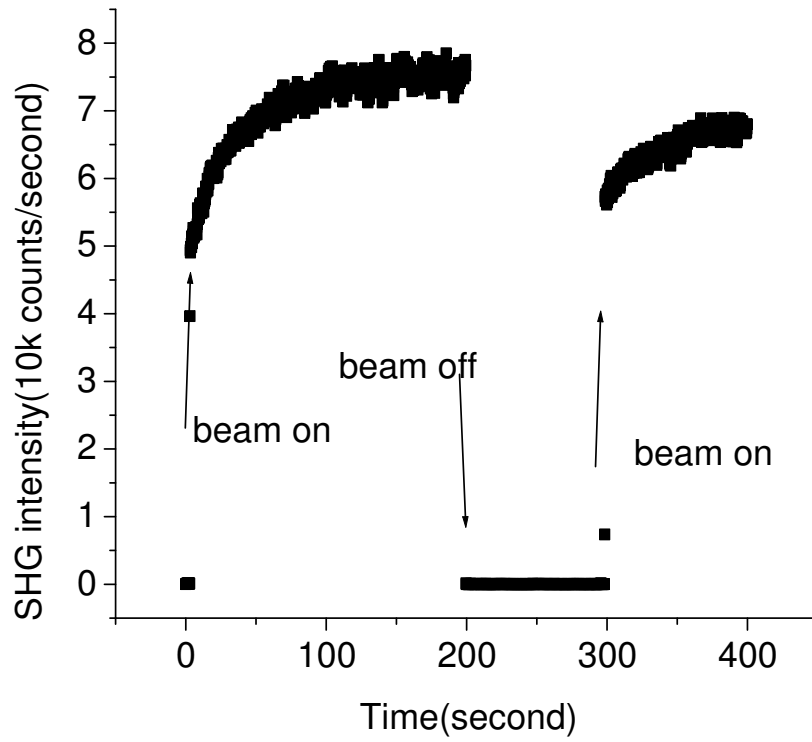


Figure 5.3: The total reflected SHG from a Si sample (lightly p-doped silicon substrate with 9 nm thick SiO₂ on top) increases by time which is due to the DC electric field building up by the trapped charges on the sample surface.

ples were introduced to the vacuum via a load lock and transferred into the CVD chamber on a sample mount that slides onto an infrared (IR) heating unit. The IR heating unit utilizes a 400W Osram Xenophot IR light bulb to heat samples from the backside, producing surface temperatures up to 830 °C. Sample temperatures were measured indirectly using a calibrated reference thermocouple. Dilute disilane gas (4% Si₂H₆ in helium) was introduced to the reactor through a leak valve to backfill the chamber to the desired pressure. The samples were cleaned in acetone, ethanol and rinsed in deionized water (DI-water). They were blown dry with helium gas prior to entry in the load lock. All samples were annealed at 700 °C prior to growth remove adsorbed water and surface contaminants. Samples were then kept at 600 °C, while disilane pressure was kept at 1×10^4 Torr for nanocrystal CVD growth.

The optical setup is shown in Figure 5.4. SH signals were generated by unamplified 120 fs Ti:sapphire laser pulses (76MHz repetition rate, tunable from 710 nm to 800 nm), focused onto the sample through an optical port at an angle of incidence 55° from normal with p-polarization. Reflected p-polarized SHG was detected by a photon counting system. A fraction of the fundamental beam was split off to generate a SH reference signal from a wedged Z cut crystalline quartz plate in order to normalize signal intensity against laser intensity fluctuation. Constant background noise was suppressed by chopping the fundamental beam and subtracting the counts with laser pulse unblocked and blocked. Reflected fundamental laser light was blocked by color glass filters.

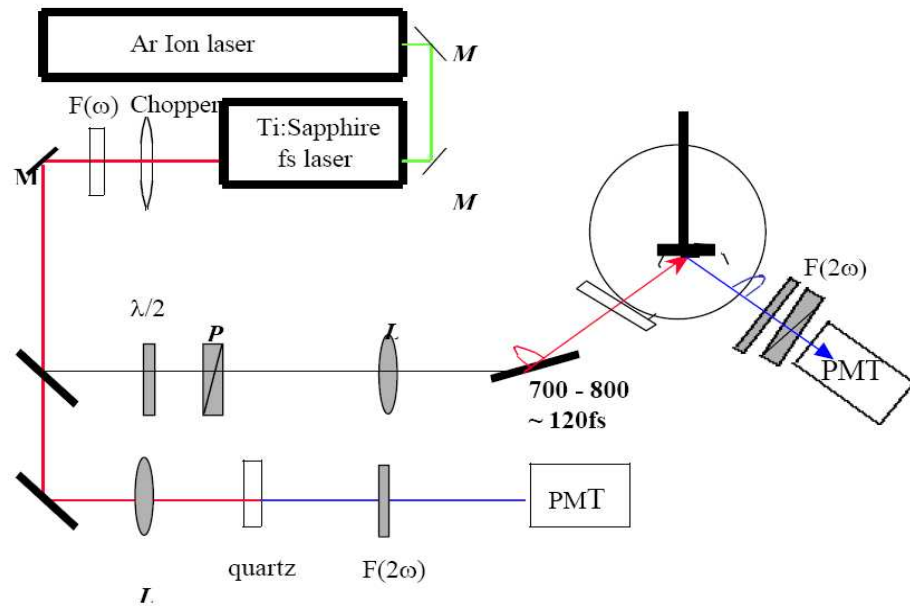


Figure 5.4: Experimental setup. M: Mirror, F: Filter, $\lambda/2$: halfwave plate, P: Polarizer, L: Lens.

5.3 Surface contaminants effect on TDSHG

We first determined experimentally the optimum oxide thickness for SHG *in situ* TD-EFISH monitoring. Figure 5.5 shows TDSHG from a silicon sample with 10 nm thermal oxide before and after removing surface contaminants by annealing to 600⁰C for ten minutes. In both cases, TDSHG is negligible, demonstrating that this oxide is too thick for our purposes. By contrast, Figure 5.6 shows that TDSHG from a silicon sample with 2 nm native oxide is very strong, and also very sensitive to annealing treatment. We therefore investigated the annealing and surface contaminant effects in more detail on samples with oxides \ll 10 nm thick. This is also the range of oxide thickness relevant for flash memory device application.

A sample after standard cleaning still captures contaminant molecules on its surface as long as it is exposed to ambient air. Even when the sample is inserted into the UHV chamber, the molecules remain and must be removed before CVD nanocrystal growth. The sample is annealed at 700⁰C for 10 minutes to remove contaminant molecules completely from the surface. If the sample is annealed at lower temperature, surface molecules are only partly removed, and can be easily detected by TDSHG. Figure 5.6 shows the effect on TDSHG of systematically increasing annealing temperature from 50⁰C to 800⁰C for a native oxidized Si(001) sample in UHV. Each increase in temperature removes more surface contaminants, causing a corresponding decrease in the time-dependent rise of SHG. After an 800⁰C annealing, the time-dependence has disappeared completely. Figure 5.7 shows a similar trend for a Si(001) sam-

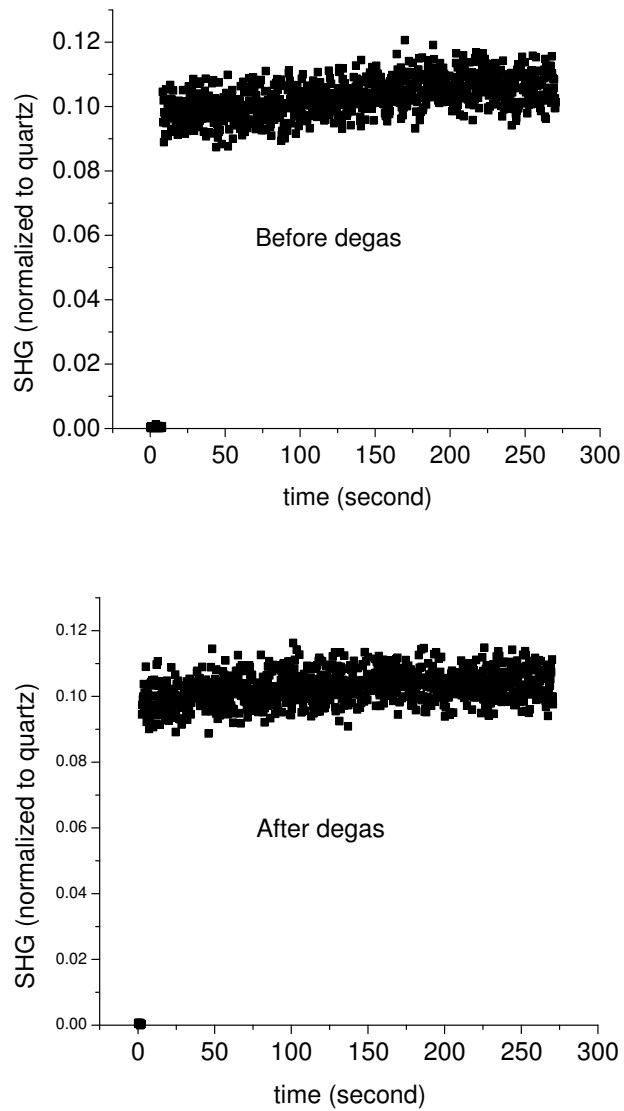


Figure 5.5: Top: TDSHG from a lightly p-doped silicon sample with 10 nm thermal oxide on top increases slightly by time. Bottom: After annealing at temperature 600°C and then cool down to room temperature, SHG from the same sample is flat over time. The data were taken in high vacuum ($\sim 10^{-9}$ Torr) at room temperature.

ple with a gate dielectric consisting of 1.1 nm SiO₂ and 3.5 nm HfO₂, prepared by atomic layer epitaxy [16]. Such “high-k” dielectrics are also of interest as substrates for Si-NC-based flash memory devices. As with the native-oxidized sample, TDSHG is very strong when the cleaned sample is first introduced into UHV conditions, then decreases systematically following subsequent anneals at increasing temperature. In this case, annealing at 600⁰C was sufficient to quench TDSHG. After the sample was annealed at 600⁰ or above, most of the molecules (contaminants) on the sample surface were gone, the TDSHG is completely flat. After the sample is exposed to air for about 1 hour, the TDSHG recovers (see Figure 5.7 Bottom). The results indicate the surface contaminants play an important role in EFISH probing [16].

5.4 Monitoring growth of Si NCs

To check the feasibility of using EFISH caused by electrons trapped in Si NCs to monitor growth of Si NCs, we introduced a fully fabricated Si NC sample, manufactured in Motorola, into the growth chamber. The sample was prepared by rapid thermal CVD of Si using silane precursor (partial pressure 37 - 110 mTorr) at the hot (450 - 800 ⁰C) surface of thermally grown oxide (3.5 nm in thickness) on undoped Si(001) wafer, where the deposited Si coalesced into a 2D NC layer. Si NC layers were then passivated by top oxides (6 nm in thickness). The average NC size and density is 8 nm and $6 \times 10^{11} \text{cm}^{-2}$, determined by SEM analysis. Based on the results in Figure 5.5, contaminants at the surface of such a thick oxide (9.5 nm total) are expected to play a

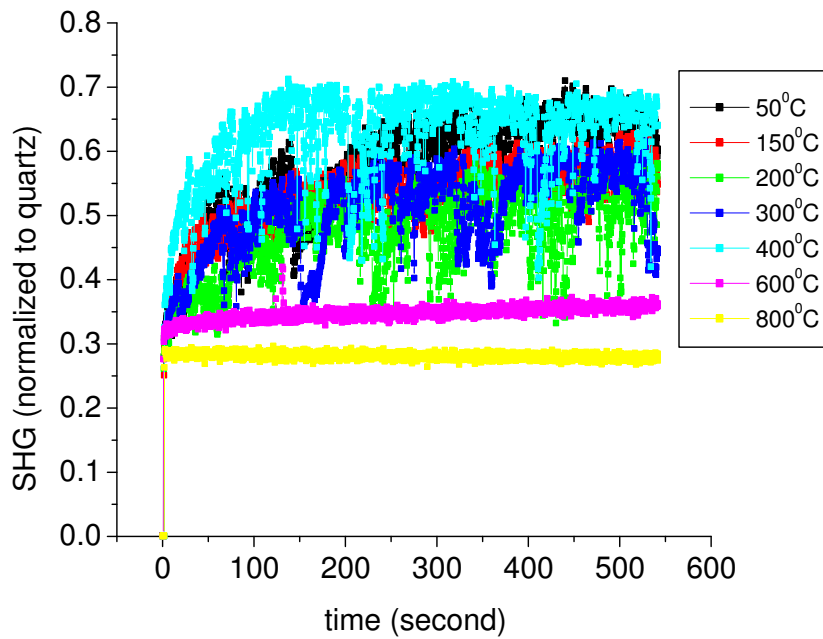


Figure 5.6: TDSHG from n^+ doped silicon sample with 2 nm native oxide on top. The sample was annealed at different temperature and then cooled down to room temperature for SHG data taking. The pressure in the vacuum is $\sim 5 \times 10^{-10}$ Torr. Each set data were taken at different point on the sample to avoid SHG hysteresis.

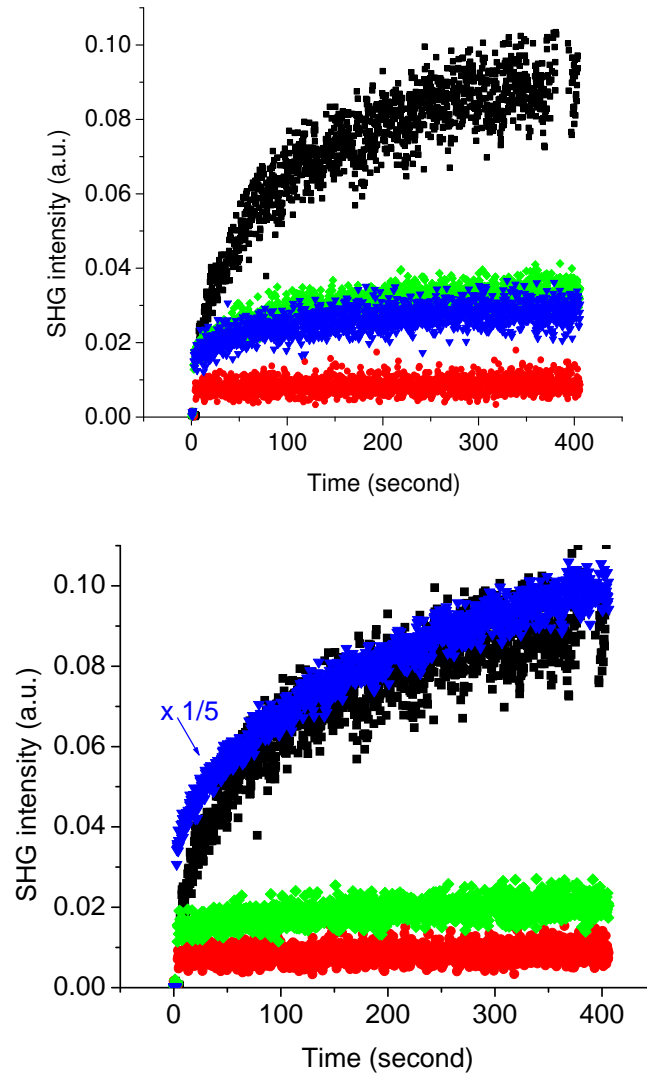


Figure 5.7: Top: TDSHG from $\text{HfO}_2(3.5 \text{ nm})/\text{SiO}_2(1.1 \text{ nm})/\text{Si}(001)$ sample depends on the annealing temperature (no annealing - solid square, 150°C - solid diamond, 300°C - solid triangle, 600°C - solid circle). Bottom: TDSHG from the same sample is large before annealing the sample (solid squares), but vanishes after annealing at 600°C for 10 minutes (solid circles). After 1 night stay in high vacuum ($\sim 10^{-9}$ Torr.), TDSHG is still negligible weak (solid diamond), but recovers after 1 hour exposure to air (solid triangle). Data were taken at room temperature in high vacuum ($\sim 10^{-9}$ Torr.)

negligible role in producing TDSHG.

Figure 5.8 (solid squares) shows that observed strong TDSHG from this sample before annealing. This appears to suggest that laser-induced charge trapping in the embedded Si NC layer is the cause of TDSHG. However, we then observed that TDSHG disappeared after the sample was annealed at 600⁰C (Figure 5.8 solid circles), and recovered after the sample was exposed again to ambient air and replaced in the chamber (Figure 5.8 solid triangles). These are the same trends observed with thinner (2-5 nm) oxides/dielectrics containing no embedded Si NCs (see Figure 5.6 and 5.7). Evidently this tells us that charges trapped by contaminants on the SiO₂ surface are playing a role, even though photo-excited electrons can hardly diffuse to the SiO₂ surface through a uniform 9.5 nm (3.5 nm tunneling + 6 nm covering) thick oxide. We hypothesize, therefore, that one or both of the following mechanism is at work in this sample: (1) the Si NC layer provides a “stepping-ston” for photo-excited electrons to reach the SiO₂ surface, but does not itself retain charge efficiently, or (2) surface contaminants catalyze the trapping of charge at the the embedded Si NCs.

Finally, we implemented SHG, including TDSHG, as an *in situ* monitoring during CVD growth of a Si NC layer onto a Si(001) substrate with 2 nm oxide (similar to the substrate studied in Figure 5.6). Strong TDSHG was observed from the Si/SiO₂ substrate before annealing and NC growth (Figure 5.9 solid squares), then disappeared after annealing at 800⁰C (Figure 5.9 solid circles), reproducing the pre-growth trends reported in Figure 5.6. CVD

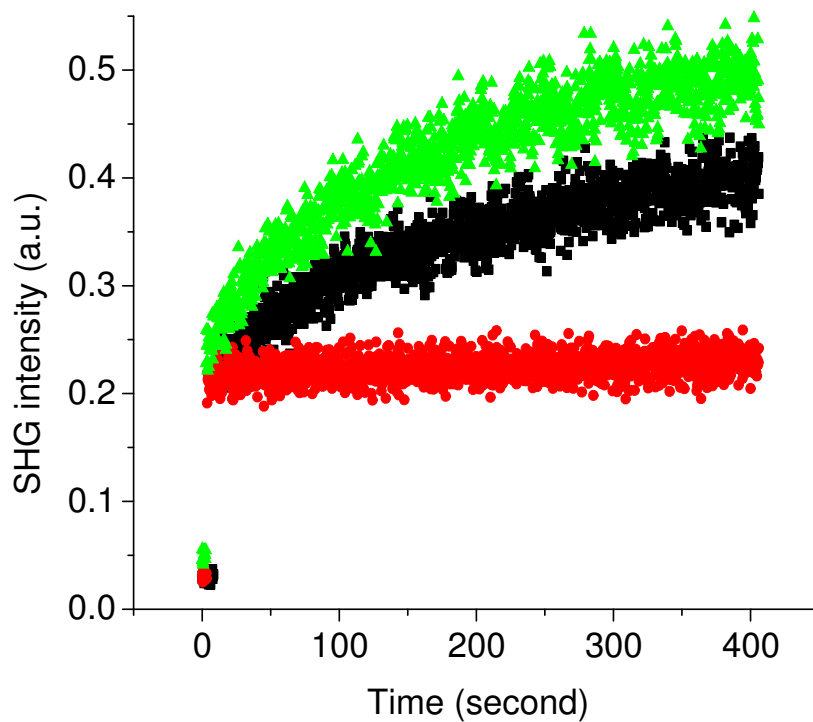


Figure 5.8: TDSHG from a Si NC sample was observed in a vacuum chamber before annealing the sample (solid squares), but disappeared when the sample was annealed at 600°C for 10 minutes and then cooled down to room temperature (solid circles). After exposure to ambient air for about 12 hours the TDSHG recovered (solid triangles).

growth was done step by step and TDSHG was taken in each interval. During CVD the laser beam remained focused on one point, but TDSHG was taken at location about 100 μm away from the original point to avoid cumulative pre-charging. We observed that reflected SHG intensity increased monotonically as the deposited NC layer increased in density from zero to 10^{10} cm^{-2} [29]. However, no time-dependence whatsoever was observed over a 140s interval at any stage of CVD growth. The TDSHG was completely flat after each step of CVD growth (see Figure 5.9). To understand this phenomenon, we estimated the DC electric field formed by electrons trapped in nanocrystals with

$$E_{DC} = z\sigma_{NC}/\epsilon, \quad (5.3)$$

where, σ_{NC} is the NC density, ϵ is the silicon permittivity and z is the number of electrons trapped on each NC. The maximum nanocrystal density achieved in a typical CVD growth is about 10^{10} cm^{-2} [29]. We assume that each NC traps one electron, so the maximum DC electric field is calculated to be $2 \times 10^3 \text{ V/cm}$. From previous work on EFISH [1, 7], applied field $E_{DC} > 10^4 \text{ V/cm}$ give rise to easily observed EFISH above the interfacial contribution without using special electro-modulation technique. The DC electric field in our experiment is an order lower than the observable threshold. Since it is hard for each NC to trap more than one electron because of Coulomb blockade, higher NC density is needed so that EFISH is observable.

Though we didn't observe significant TDSHG during growth, we observed a change in SHG intensity as a result of depositing nanocrystals on the

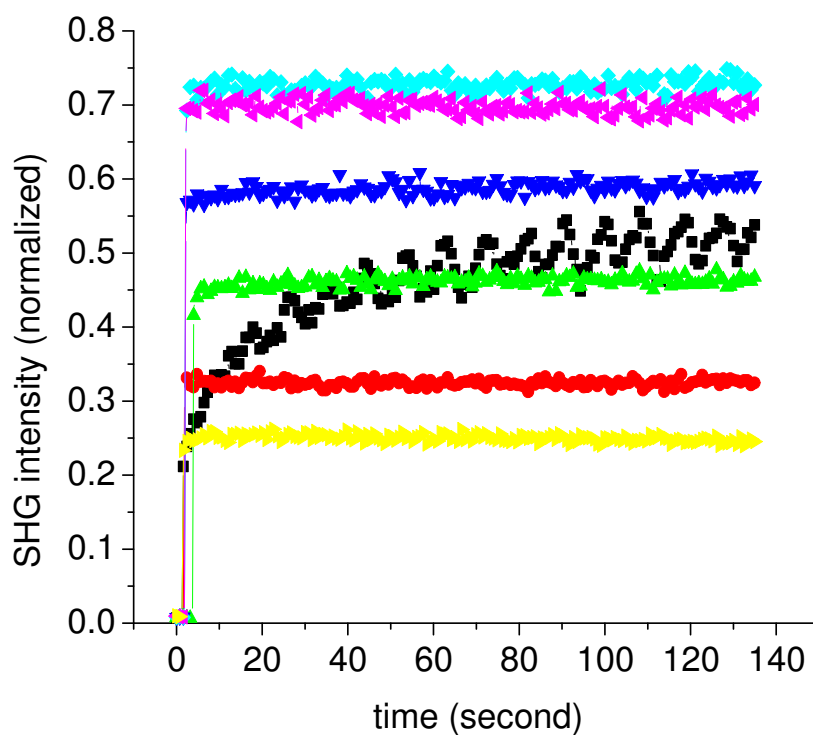


Figure 5.9: TDSHG observed from a Si sample before annealing (solid squares), after annealing (solid circles), after CVD growth for 15 minutes (solid up-triangles), 17.5 minutes (solid down-triangles), 20 minutes (solid diamonds), 25 minutes (solid left-triangles), 30 minutes (solid right-triangles). Data were taken in vacuum ($\sim 10^{-9}$ Torr.) at sample temperature 116°C .

oxide surface. This suggest that the intensity of the SHG (instead of TDSHG) can provide at least a qualitative *in situ* monitor of Si NC growth. To investigate this possibility, further *in situ* observation of time-independent SHG intensity during CVD growth were made.

In Figure 5.10 (a), SHG from an n^+ doped Si sample during CVD growth increases to the maximum after 20 minutes CVD and then decrease. The difference between the two curves shown in 5.10 (a) indicates different points on the sample give rise different SHG signals. Figure 5.10 (b) shows SHG (normalized to SHG before CVD) from samples cut from a $\text{SiO}_2(10 \text{ nm})/\text{Si}(\text{light p-doped})$ wafer shows similar CVD time dependence as $\text{SiO}_2(2 \text{ nm})/\text{Si}(n^+ \text{ doped})$ sample, except its SHG reaches the maximum after 30 minutes CVD. With the samples cut from the same wafer, we took SHG after each step of CVD growth shown in Figure 5.10 (c) and (d). Both of them have the same trend before 20 minutes CVD, but SHG in (c) decreases further while it increases in (d). SHG we obtained in above experiment actually is mixture of SHG from the nanocrystal layer grown by CVD and SHG from silicon substrate. They are different in phase as well as in magnitude. Absorption of SH by the nanocrystal layer will also affect total SHG. Since there are several factors that can affect the total SHG, it is not ideal to do quantitative *in situ* monitor with that. A possible solution to this is to use FDISHG (frequency-domain-interferometric SHG) to resolve the phase changes of the total SHG, as well as intensity [50]. The additional phase information can tell us the size and density of the nanocrystals being grown on SiO_2 surface [27].

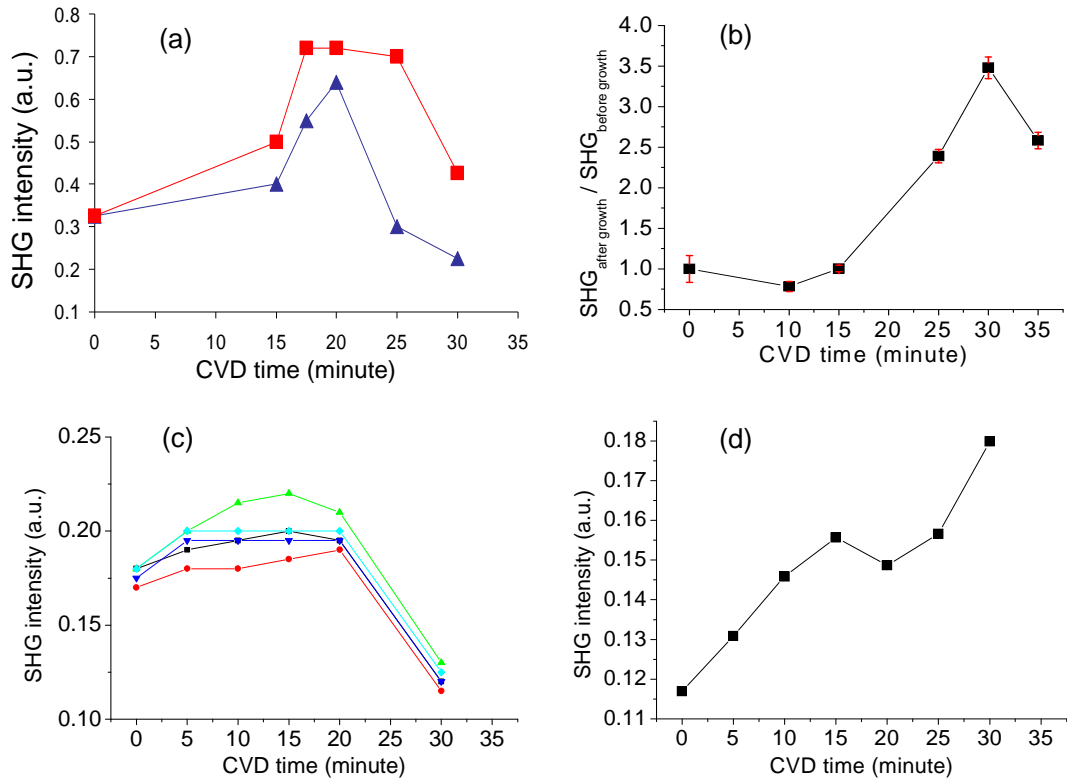


Figure 5.10: (a) Time-independent SHG from a $\text{SiO}_2(2 \text{ nm})/\text{Si}(n^+ \text{ doped})$ sample as a function of CVD time. SHG data were taken from five locations on the sample. The maximum (minimum) SHG among the five is shown by solid squares (solid triangles). (b) The ratio of SHG after and before CVD from a $\text{SiO}_2(10 \text{ nm})/\text{Si}(\text{light p-doped})$ as a function of CVD time. Each data point was taken from different samples cut from the same wafer. The error bars indicate SHG variation from point to point on one sample. (c) The sample was cut from the same wafer as in (b). SHG data were taken from four locations (indicated by four different symbols) on the sample after each step of CVD growth. (d) Repeat the experiment as in (c) with another sample cut from the same wafer. SHG from one location of the sample was taken. All SHG were taken in vacuum ($\sim 10^{-9}$ Torr.) at sample temperature $\sim 100^\circ\text{C}$.

5.5 Summary

Surface contaminants were found to dominate TD-EFISH from both Si/SiO₂ and Si/SiO₂/HfO₂ samples in UHV, including a sample with a layer of Si NCs embedded in the oxide for flash memory applications. Unfortunately, under CVD growth conditions (10⁻⁴ Torr disilane gas, clean sample surface), the expected TD-EFISH from laser-induced charge trapping in the growing Si NCs was found to be too weak to observe. Total reflected SHG intensity does change substantially as the nanocrystal layer grows, but additional phase-sensitive SHG measurements will be required to interpret the observed trends quantitatively.

Appendix

Appendix 1

SH polarization direction

The SHG polarization direction is determined by

$$\mathbf{E}_1^0 \cdot \mathbf{k}_2 \mathbf{E}_2^0 + \mathbf{E}_2^0 \cdot \mathbf{k}_1 \mathbf{E}_1^0. \quad (1.1)$$

In the coordinate system shown in Figure 2.1, if both beams are polarized in $\hat{x} - \hat{z}$ plane, then the magnetic field of either beam is in \hat{y} , so electric fields \mathbf{E}_1 and \mathbf{E}_2 can be written as

$$\mathbf{E}_1 = |\mathbf{E}_1| \hat{y} \times \mathbf{k}_1 \quad (1.2)$$

$$\mathbf{E}_2 = |\mathbf{E}_2| \hat{y} \times \mathbf{k}_2. \quad (1.3)$$

Then Formula 1.1 becomes

$$(|\mathbf{E}_1^0| \hat{y} \times \mathbf{k}_1 \cdot \mathbf{k}_2) |\mathbf{E}_2^0| \hat{y} \times \mathbf{k}_2 + (|\mathbf{E}_2^0| \hat{y} \times \mathbf{k}_2 \cdot \mathbf{k}_1) |\mathbf{E}_1^0| \hat{y} \times \mathbf{k}_1. \quad (1.4)$$

The common factor $|\mathbf{E}_1^0| |\mathbf{E}_2^0|$ does not affect the direction, so the polarization direction is determined by

$$(\hat{y} \times \mathbf{k}_1 \cdot \mathbf{k}_2) \hat{y} \times \mathbf{k}_2 + (\hat{y} \times \mathbf{k}_2 \cdot \mathbf{k}_1) \hat{y} \times \mathbf{k}_1. \quad (1.5)$$

Use equation $\mathbf{a} \cdot (\mathbf{b} \times \mathbf{c}) = \mathbf{b} \cdot (\mathbf{c} \times \mathbf{a})$, the above formula becomes

$$\begin{aligned}
& \hat{y} \cdot (\mathbf{k}_1 \times \mathbf{k}_2) \hat{y} \times \mathbf{k}_2 + \hat{y} \cdot (\mathbf{k}_2 \times \mathbf{k}_1) \hat{y} \times \mathbf{k}_1 \\
&= \hat{y} \cdot (\mathbf{k}_1 \times \mathbf{k}_2) (\hat{y} \times \mathbf{k}_2 - \hat{y} \times \mathbf{k}_1) \\
&= \hat{y} \cdot (\mathbf{k}_1 \times \mathbf{k}_2) \hat{y} \times (\mathbf{k}_2 - \mathbf{k}_1). \tag{1.6}
\end{aligned}$$

$\hat{y} \cdot (\mathbf{k}_1 \times \mathbf{k}_2)$ is a scalar, so the direction is determined by $\hat{y} \times (\mathbf{k}_2 - \mathbf{k}_1)$. Then we calculate

$$\begin{aligned}
& (\mathbf{k}_1 + \mathbf{k}_2) \times (\hat{y} \times (\mathbf{k}_2 - \mathbf{k}_1)) \\
&= \hat{y} (\mathbf{k}_1 + \mathbf{k}_2) \cdot (\mathbf{k}_2 - \mathbf{k}_1) - (\mathbf{k}_2 - \mathbf{k}_1) [(\mathbf{k}_1 + \mathbf{k}_2) \cdot \hat{y}] \\
&= 0, \tag{1.7}
\end{aligned}$$

where, $|\mathbf{k}_1| = |\mathbf{k}_2|$ (the two beams have the same wavelength) is used in the last step of calculation. The result obtained above proves the SH polarization is parallel to $\mathbf{k}_1 + \mathbf{k}_2$.

Bibliography

- [1] O. A. Aktsipetrov, A. A. Fedyanin, V. N. Golovkina, and T. V. Murzina. Optical second-harmonic generation induced by a dc electric field at the Si-SiO₂ interface. *Opt. Lett.*, 19(18):1450–1452, 1994.
- [2] O. A. Aktsipetrov, A. A. Fedyanin, A. V. Melnikov, E. D. Mishina, A. N. Rubtsov, M. H. Anderson, P. T. Wilson, M. ter Beek, X. F. Hu, J. I. Dadap, and M. C. Downer. dc-electric-field-induced and low-frequency electromodulation second-harmonic generation spectroscopy of Si(001) – SiO₂ interfaces. *Phys. Rev. B*, 60(12):8924–8938, Sep 1999.
- [3] Y. Barad, H. Eisenberg, M. Horowitz, and Y. Silberberg. Nonlinear scanning laser microscopy by third harmonic generation. *Applied Physics Letters*, 70(8):922–924, 1997.
- [4] M. Baudrier-Raybaut, R. Haidar, Ph. Kupecek, Ph. Lemasson, and E. Rosencher. Random quasi-phase-matching in bulk polycrystalline isotropic nonlinear materials. *Nature*, 432(7015):374–376, Nov 2004.
- [5] S. Bergfeld and W. Daum. Second-Harmonic Generation in GaAs: Experiment versus Theoretical Predictions of χ_{xyz}^2 . *Physical Review Letters*, 90(3):036801, 2003.

- [6] D. S. Bethune, R. W. Smith, and Y. R. Shen. Optical Quadrupole Sum-Frequency Generation in Sodium Vapor. *Phys. Rev. Lett.*, 37(7):431–434, Aug 1976.
- [7] J. Bloch, J. G. Mihaychuk, and H. M. van Driel. Electron Photoinjection from Silicon to Ultrathin SiO₂ Films via Ambient Oxygen. *Phys. Rev. Lett.*, 77(5):920–923, Jul 1996.
- [8] N. Bloembergen and R. K. Chang. McGraw-Hill, New York, 1966.
- [9] N. Bloembergen, R. K. Chang, S. S. Jha, and C. H. Lee. Optical Second-Harmonic Generation in Reflection from Media with Inversion Symmetry. *Phys. Rev.*, 174(3):813–822, Oct 1968.
- [10] N. Bloembergen and Y. R. Shen. Optical Nonlinearities of a Plasma. *Phys. Rev.*, 141(1):298–305, Jan 1966.
- [11] Robert W. Boyd. *Nonlinear Optics*. ACADEMIC PRESS, 2003.
- [12] Fielding Brown and Masahiro Matsuoka. Effect of Adsorbed Surface Layers on Second-Harmonic Light from Silver. *Phys. Rev.*, 185(3):985–987, Sep 1969.
- [13] Fielding Brown, Robert E. Parks, and Arthur M. Sleeper. Nonlinear Optical Reflection from a Metallic Boundary. *Phys. Rev. Lett.*, 14(25):1029–1031, Jun 1965.

- [14] Vera L. Brudny, Bernardo S. Mendoza, and W. Luis Mochán. Second-harmonic generation from spherical particles. *Phys. Rev. B*, 62(16):11152–11162, Oct 2000.
- [15] Paul J Campagnola and Leslie M Loew. Second-harmonic imaging microscopy for visualizing biomolecular arrays in cells, tissues and organisms. *Nat Biotech*, 21(11):1356–1360, Nov 2003.
- [16] R. Carriles, J. Kwon, Y. Q. An, L. Sun, S. K. Stanley, J. G. Ekerdt, M. C. Downer, J. Price, T. Boescke, and A. C. Diebold. Optical characterization of process-dependent charging in hafnium oxide structures. volume 24, pages 2160–2168. AVS, 2006.
- [17] Stefano Cattaneo. Two-beam surface second-harmonic generation. *Ph.D. dissertation*, 2004.
- [18] Stefano Cattaneo and Martti Kauranen. Polarization-based identification of bulk contributions in surface nonlinear optics. *Phys. Rev. B*, 72(3):033412, Jul 2005.
- [19] J. M. Chen, J. R. Bower, and C. S. Wang. Optical second-harmonic generation from submonolayer Na-covered Ge surfaces. *Optics Communications*, 9(2):132–134, 1973.
- [20] J. I. Dadap, J. Shan, K. B. Eisenthal, and T. F. Heinz. Second-Harmonic Rayleigh Scattering from a Sphere of Centrosymmetric Material. *Phys. Rev. Lett.*, 83(20):4045–4048, Nov 1999.

- [21] A. A. Fedyanin, N. V. Didenko, N. E. Sherstyuk, A. A. Nikulin, and O. A. Aktsipetrov. Interferometry of hyper-Rayleigh scattering by inhomogeneous thin films. *Opt. Lett.*, 24(18):1260–1262, Sep 1999.
- [22] M.M. Fejer, G.A. Magel, D.H. Jundt, and R.L. Byer. Quasi-phase-matched second harmonic generation: tuning and tolerances. *Quantum Electronics, IEEE Journal of*, 28(11):2631–2654, Nov 1992.
- [23] P. Figliozzi, L. Sun, Y. Jiang, N. Matlis, B. Mattern, M. C. Downer, S. P. Withrow, C. W. White, W. L. Mochan, and B. S. Mendoza. Single-Beam and Enhanced Two-Beam Second-Harmonic Generation from Silicon Nanocrystals by Use of Spatially Inhomogeneous Femtosecond Pulses. *Physical Review Letters*, 94(4):047401, 2005.
- [24] P. A. Franken, A. E. Hill, C. W. Peters, and G. Weinreich. Generation of Optical Harmonics. *Phys. Rev. Lett.*, 7(4):118–119, Aug 1961.
- [25] P. Guyot-Sionnest, W. Chen, and Y. R. Shen. General considerations on optical second-harmonic generation from surfaces and interfaces. *Phys. Rev. B*, 33(12):8254–8263, Jun 1986.
- [26] Robert Hellwarth and Paul Christensen. Nonlinear optical microscopic examination of structure in polycrystalline ZnSe. *Optics Communications*, 12(3):318–322, 1974.
- [27] Y. Jiang, L. Sun, and M. C. Downer. Second-harmonic spectroscopy of two-dimensional Si nanocrystal layers embedded in SiO₂ films. *Applied*

- Physics Letters*, 81(16):3034–3036, 2002.
- [28] Y. Jiang, P. T. Wilson, M. C. Downer, C. W. White, and S. P. Withrow. Second-harmonic generation from silicon nanocrystals embedded in SiO₂. *Applied Physics Letters*, 78(6):766–768, 2001.
- [29] W. Thomas Leach, Jianhong Zhu, and John G. Ekerdt. Cracking assisted nucleation in chemical vapor deposition of silicon nanoparticles on silicon dioxide. *Journal of Crystal Growth*, 240(3-4):425–422, 2002.
- [30] P. D. Maker, R. W. Terhune, M. Nisenoff, and C. M. Savage. Effects of Dispersion and Focusing on the Production of Optical Harmonics. *Phys. Rev. Lett.*, 8(1):21–22, Jan 1962.
- [31] W. Luis Mochan, Jesus A. Maytorena, Bernardo S. Mendoza, and Vera L. Brudny. Second-harmonic Generation in Arrays of Spherical Particles. *Physical Review B (Condensed Matter and Materials Physics)*, 68(8):085318, 2003.
- [32] L. Pavesi, L. Dal Negro, C. Mazzoleni, G. Franzo, and F. Priolo. Optical gain in silicon nanocrystals. *Nature*, 408(6811):440–444, Nov 2000.
- [33] Sylvie Roke, Wim G. Roeterdink, Judith E. G. J. Wijnhoven, Andrei V. Petukhov, Aart W. Kleyn, and Mischa Bonn. Vibrational Sum Frequency Scattering from a Submicron Suspension. *Physical Review Letters*, 91(25):258302, 2003.

- [34] Sylvie Roke, Wim G. Roeterdink, Judith E. G. J. Wijnhoven, Andrei V. Petukhov, Aart W. Kleyn, and Mischa Bonn. Vibrational Sum Frequency Scattering from a Submicron Suspension. *Physical Review Letters*, 91(25):258302, 2003.
- [35] Joseph Rudnick and E. A. Stern. Second-Harmonic Radiation from Metal Surfaces. *Phys. Rev. B*, 4(12):4274–4290, Dec 1971.
- [36] G. Russakoff. A Derivation of the Macroscopic Maxwell Equations. *American Journal of Physics*, 38(10):1188–1195, 1970.
- [37] Y. R. Shen. *The Principles of Nonlinear Optics*. Wiley & Sons, New York, 1984, section 6.6.
- [38] C. Sheppard and J. Gannaway. The scanning harmonic optical microscope. *Quantum Electronics, IEEE Journal of*, 9:912–912, 1977.
- [39] J. E. Sipe, Victor Mizrahi, and George I. Stegeman. Fundamental difficulty in the use of second-harmonic generation as a strictly surface probe. *Phys. Rev. B*, 35(17):9091–9094, Jun 1987.
- [40] J. E. Sipe, D. J. Moss, van Driel, and H. M. Phenomenological theory of optical second- and third-harmonic generation from cubic centrosymmetric crystals. *Phys. Rev. B*, 35(3):1129–1141, Jan 1987.
- [41] J.E. Sipe and G.I. Stegeman. North-Holland, Amsterdam, 1982.

- [42] Jeffrey Squier, Michiel Muller, G. Brakenhoff, and Kent R. Wilson. Third harmonic generation microscopy. *Optics Express*, 3(9):315–324, Oct 1998.
- [43] L. Sun, P. Figliozzi, Y. Q. An, M. C. Downer, W. L. Mochn, and B. S. Mendoza. Nonresonant quadrupolar second-harmonic generation in isotropic solids by use of two orthogonally polarized laser beams. *Opt. Lett.*, 30(17):2287–2289, Sep 2005.
- [44] L. Sun, P. Figliozzi, Y. Jiang, M. C. Downer, W. L. Mochn, and B. S. Mendoza. SHG spectroscopy of nano-interfaces. *physica status solidi (c)*, 2(12):4067–4071, Nov 2005.
- [45] R. W. Terhune, P. D. Maker, and C. M. Savage. Optical Harmonic Generation in Calcite. *Phys. Rev. Lett.*, 8(10):404–406, May 1962.
- [46] Sandip Tiwari, Farhan Rana, Hussein Hanafi, Allan Hartstein, Emmanuel F. Crabbe, and Kevin Chan. A silicon nanocrystals based memory. *Applied Physics Letters*, 68(10):1377–1379, 1996.
- [47] CHARLES C. WANG. Second-Harmonic Generation of Light at the Boundary of an Isotropic Medium. *Phys. Rev.*, 178(3):1457–1460, Feb 1969.
- [48] Charles C. Wang and A. N. Duminski. Second-Harmonic Generation of Light at the Boundary of Alkali Halides and Glasses. *Phys. Rev. Lett.*, 20(13):668–671, Mar 1968.

- [49] C. W. White, J. D. Budai, S. P. Withrow, J. G. Zhu, E. Sonder, R. A. Zuhr, A. Meldrum, D. M. Hembree, Jr., D. O. Henderson, and S. Praver. Encapsulated semiconductor nanocrystals formed in insulators by ion beam synthesis. *Nuclear Instruments and Methods in Physics Research Section B: Beam Interactions with Materials and Atoms*, 141(1-4):228–240, 1998.
- [50] P. T. Wilson, Y. Jiang, O. A. Aktsipetrov, E. D. Mishina, and M. C. Downer. Frequency-domain interferometric second-harmonic spectroscopy. *Opt. Lett.*, 24(7):496–498, 1999.
- [51] S. P. Withrow, C. W. White, A. Meldrum, J. D. Budai, Jr. D. M. Hembree, and J. C. Barbour. Effects of hydrogen in the annealing environment on photoluminescence from Si nanoparticles in SiO₂. *Journal of Applied Physics*, 86(1):396–401, 1999.

Index

- $\beta, \gamma, \delta, \zeta$, 5
 $\chi_D^{(2)}$, 5
 $\chi_Q^{(2)}$, 5
- Abstract, vii
Acknowledgments, v
anneal, 83
Appendices, 95
- Bibliography*, 105
birefringent crystal, 70
broken inversion symmetry, 3
- calcite crystal*, 2
centrosymmetric materials, 1
chemical vapor deposition, 77
coherence length, 54
Coulomb blockade, 77
CVD, 77
- DC electric field*, 76
Dedication, iv
density gradient of nanocrystals, 51
- EFISH*, 75
Enhanced 2-beam SHG from glass,
12
Experimental setup, 10
- FDISHG*, 92
flash memory, 35
Fourier decomposition, 1
- group velocity*, 73
Guoy phase shift, 20
- HfO₂*, 85
high-k dielectrics, 85
Historical notes, 2
hydrodynamic model, 3
hyper-Rayleigh scattering, 4
- in situ monitoring CVD growth*, 75
interface chemistry, 47
Introduction, 1
isotropic medium, 6
- Maker fringes*, 54
Monitoring growth of Si NCs, 85
- nano-structures*, 3
nanocrystal CVD growth, 81
nanocrystal density gradients, 41
native oxide, 83
noncentrosymmetric materials, 1
- pellicle thin films*, 69
Phase matched, 60
phase matching schemes, 62
Phase mismatch, 17
phase mismatch, 54
Phase-Matched SHG from calcite crystals, 70
Phenomenological model of quadrupolar SHG, 4
plane wave approximation, 10
polarization, 1
- QPM crystals*, 60
quadrupolar SH polarization, 2

Quadrupolar SHG in glass, 8
Quadrupolar SHG Theory, 9
quadrupole moment, 45
quantum confinement, 35
Quasi-Phase-Matched SHG from glass slides, 63
*Quasi-Phase-Matched SHG from pel-
 licle thin films*, 69

Sandwich experiment, 21
Scope of this work, 6
Sensitivity to surface chemistry, 39
SH polarization direction, 96
SH radiation, 1
SHG, 1
*SHG from glass using elliptically po-
 larized beams*, 16
SHG Radiation pattern, 42
SHG signal discrimination, 52
*silicon nanocrystal sample prepara-
 tion*, 36
Silicon nanocrystals, 35
Single beam SHG, 39
spectrum, 54
sphere, 4
Surface contaminants, 77
Surface contaminants effect, 83

TDSHG, 77
time-dependent SHG, 77
trap sites, 77
Two-beam SHG, 43
Two-beam SHG microscopy, 28
Two-beam SHG Theory, 45
type I phase matching, 72
type II phase matching, 72

vibrational sum frequency generation,
 4
wedge sample, 67

z-scan, 17
ZnO, 28

Vita

Liangfeng Sun was born in Taizhou, Zhejiang, China on Nov 12th, 1975, the son of Junyi Sun and Jinzhi Bao. He received the Bachelor of Engineering degree in Engineering Physics from Tsinghua University (Beijing, China) in 1997. He continued his graduate study in the Institute of High Energy Physics in Beijing, and received the Master of Science degree in Nuclear and Particle Physics in 2000. He applied to the University of Texas at Austin for enrollment in their physics program. He was accepted and started graduate studies in August, 2000. He began his doctoral work in Femtosecond Spectroscopy Laboratory, supervised by Professor Michael C. Downer.

Permanent address: 1632 W 6th St Apt D
Austin, Texas 78703

This dissertation was typeset with \LaTeX^\dagger by the author.

[†] \LaTeX is a document preparation system developed by Leslie Lamport as a special version of Donald Knuth's \TeX Program.